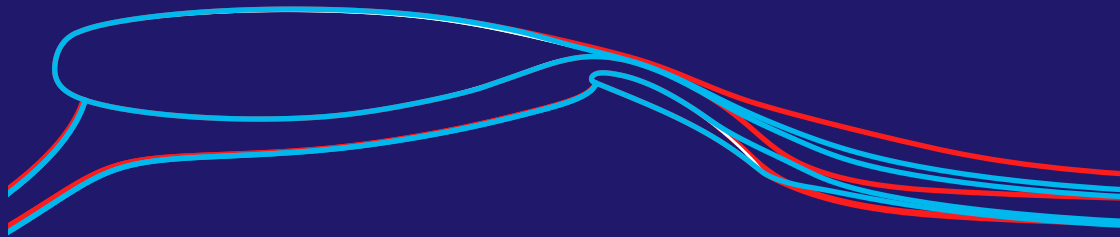


# Boundary layer suction configurations with minimal pump requirements for multi-element airfoils

Thesis

Jorik Van Craenenbroeck

Technische Universiteit Delft





# BOUNDARY LAYER SUCTION CONFIGURATIONS WITH MINIMAL PUMP REQUIREMENTS FOR MULTI-ELEMENT AIRFOILS

THESIS

by

**Jorik Van Craenenbroeck**

in partial fulfillment of the requirements for the degree of

**Master of Science**  
in Aerospace Engineering

at the Delft University of Technology.

Student number:	4047125	
Project duration:	August 3, 2015 - 30/05/2016	
Supervisor:	Prof. dr. ir. L. Veldhuis	
Thesis committee:	Prof. dr. ir. L. Veldhuis,	TU Delft
	Prof. dr. ir. B. van Oudheusden,	TU Delft
	Ir. N. Timmer	TU Delft



# SUMMARY

High lift systems are complex and heavy systems but despite that they are still indispensable to reconcile optimal cruise performance of the aircraft with an acceptable take-off and landing performance with regard to required runway length. However, a definitive trend towards lower complexity high lift systems is already ongoing for quite some time ([1]) and new methods to allow lighter and simpler high lift systems are actively sought after. One of the methods that has already proven to be able to increase high lift performance is boundary layer suction. The main disadvantage of a boundary layer suction however is that it is a form of active boundary layer control with often high power requirements. In an attempt to make up for the power requirements and minimize the weight penalty of a boundary layer suction system, systems that use an already existing low-pressure area in the engine ([2]) are interesting to pursue; nevertheless they still require extra power generation. Along the same line of reasoning a BLS system can be envisaged that is driven by a ‘naturally occurring’ low pressure zone, such as the low pressure zone near the wing-tip generated by the wing-tip vortex. The underpressure that can be expected from this however is not very low, certainly not in the order of magnitude that is necessary for a typical BLS system. Therefore the requirements for the boundary layer suction system become a very important aspect. While the research in the presented area is usually focused on maximizing the maximum lift coefficient at the cost of high system requirements (such as the required under pressure) the aim of the presented project is to look at the possible gains due to boundary layer suction on a multi-element airfoil while minimizing the requirements for the boundary layer suction system. Losing the additional lift that could be achieved with a more demanding system should be compensated by a reduction in complexity, weight and the absence of the need for additional power generation.

In order to perform this investigation a simulation platform is required. A numerical approach is used: the flowfield is simulated with the inviscid-viscid interaction flow solver MSES which is suitable for multi-element airfoils. This code however was (re-)adapted to include the simulation of BLS, which was part of the work. The report therefore includes a part describing this work as well as a part describing the validation of the applied changes. The adaption of the code to include the simulation of BLS relied heavily upon the work of Merchant and also de Oliveira Andrade and mainly involved changing the integral boundary layer formulation and closure relations in MSES [3, 4]. Validation of this work yielded the following observations:

- The simulation of larger areas of continuous suction is well predicted, the error for the suction cases is on the same order as the non-suction case. Agreement with rFoilsuc (also an inviscid-viscid flow solver adapted for BLS, although for single elements) is excellent.
- In the case of slot suction the effect of the recirculation zones at the slot entrance cannot be captured and this resulted in an underprediction of  $\theta$ . Comparison with experimental data showed that this did not affect the prediction of the ‘outer flow’ very much, but the underestimation of  $\theta$  may become a problem in cases with severe adverse pressure gradients where separation becomes an issue.
- The reliability of the flow prediction near  $C_{l_{max}}$  is unclear and varies from case to case. Therefore it is advisable to avoid using results near this area.

Shifting the focus back to the investigation for a low-requirement BLS design again, the question of what defines the required power of a BLS system is addressed. With the help of the equation for an ideal pump one can conclude that this consists at the one hand of the required increase in total pressure that must be overcome and on the other hand the suction level and area. To relax the requirements for the increase in total pressure it is interesting to apply suction at a location with a relatively high static pressure. It was concluded that the most promising suction location while taking this into consideration is towards the trailing edge of an element, largely to try to influence the wake; the focus of the study is largely concentrated on this subject.

In the presence of an adverse pressure gradient the wake tends to grow thicker and this can escalate to a situation where the wake dominates the flowfield, a loss of lift can be observed and even flow reversal occurs in the wake: ‘wake burst’. Making the boundary layer thinner with the help of suction can delay this and

increase the overall lift again. A critical factor in the detection of this so-called wake burst is the growth rate of the displacement thickness  $\frac{d\delta^*}{ds}$ : based on experimental data found in literature and the simulations with MatSESuction it was found that if it reaches a critical value of 0.23 wake burst is likely to happen.

Simulations on the NLR7301 and MFFS026 multi-element airfoil systems in a configuration where wake burst occurs show that the overall lift can be successfully increased by applying suction. A clear link between suction and the growth rate of  $\delta^*$  in the wake can be distinguished; and by keeping  $\frac{d\delta^*}{ds}$  below the critical value wake burst is avoided. In the case of the NLR7301 the lift coefficient is increased from 3.064 to 3.196 (or an increase of 4.31%) and for the MFFS026 it is increased from 3.5 to 3.6 (3%).

The simulations showed that the investigated suction configurations do not yield a significant benefit over earlier investigated BLS configurations, nor does it perform significantly worse but with the consideration that it only makes sense when wake burst is present. However, this does not take into account the effect of the suction location. Typical BLS configurations all feature suction at locations where the pressure is already very low, which will in practice require a lot of power to generate the increase in total pressure that is required to maintain the suction distribution. This again calls for a powerful pump, let alone making it possible to use a naturally occurring low pressure zone to drive the BLS. It becomes then a question of balancing the 'power' that is willing to be 'invested' in the BLS system with the suction location and strength.

# PREFACE

This report is a graduate thesis, written as a part of the Master's degree in Aerodynamics at the Faculty of Aerospace Engineering, Delft University of Technology. A basic knowledge of aerodynamics is recommended, although the necessary key ideas are explained in chapters 2 (and 5).

With this thesis I will finish my studies here in Delft and this seems like an appropriate time and place to thank some people. First and foremost my parents, who have supported me for all these years — also financially (thank you!) — and gave me the opportunity to study here in Delft. Thanks for being so patient and understanding every time I announced plans — academic and sometimes non-academic — that delayed my graduation a little bit. You made this part easy for me.

When thinking about my time here in Delft, my thoughts go immediately out to the great group of friends I have made here. Not only were you a big support for study related issues, but you were also very important for the personal development I have gone through during all these years. I couldn't have done it without you and it certainly would not have been such an amazing time!

*Tesamen met deze thesis zal ik ook mijn studies hier in Delft afronden en dit lijkt me een goed moment om even wat personen te bedanken. Eerst en vooral mijn ouders die mij al deze jaren gesteund hebben — ook financieel (dank u!) — en die me de mogelijkheid hebben gegeven om hier in Delft te komen studeren. Bedankt om zo geduldig en begrijpend te zijn iedere keer ik plannen — academische en soms non-academische — aankondigde die mijn afstuderen zouden uitstellen. Jullie maakten het me op dit vlak erg makkelijk.*

*Als ik aan de voorbije tijd hier in Delft denk gaan mijn gedachten direct uit naar de geweldige groep vrienden die ik hier heb gemaakt. Jullie waren niet alleen een grote steun tijdens het studeren, maar jullie waren ook erg belangrijk voor de persoonlijke ontwikkeling die ik heb doorgemaakt door al deze jaren. Zonder jullie zou het niet gelukt zijn en het zou zeker niet zo'n fantastische tijd geweest zijn!*

I also would like to thank my supervisors L. Veldhuis and B. van Oudheusden for their support during the project, as well as G. de Oliveira Andrade who helped me with some of the problems I encountered with the MSES code.

*Jorik Van Craenenbroeck  
Delft, May 2016*



# CONTENTS

<b>1</b>	<b>Introduction</b>	<b>1</b>
<b>2</b>	<b>Theoretical background</b>	<b>3</b>
2.1	High lift systems . . . . .	3
2.1.1	Introduction to high lift systems . . . . .	3
2.1.2	Multi-element airfoil flow fields . . . . .	4
2.1.3	Working principles of multi-element airfoils . . . . .	5
2.1.4	Flow separation . . . . .	8
2.1.5	Wake . . . . .	14
2.2	Boundary layer suction . . . . .	16
2.2.1	Historical background and flying examples . . . . .	16
2.2.2	Suction type . . . . .	17
2.2.3	Boundary layer suction on multi-element airfoils . . . . .	20
<b>3</b>	<b>Boundary layer suction for MSES</b>	<b>25</b>
3.1	MSES in short . . . . .	25
3.1.1	Newton system . . . . .	26
3.2	Code structure & summary of modifications . . . . .	28
3.3	Momentum integral relations . . . . .	30
3.3.1	von Kármán integral boundary relation . . . . .	30
3.3.2	Kinetic energy shape parameter equation . . . . .	32
3.4	Closure relations . . . . .	32
3.4.1	Laminar closure . . . . .	32
3.4.2	Turbulent closure . . . . .	33
3.5	Coupling condition . . . . .	33
3.6	The ‘mat’ in MatSESuction . . . . .	34
<b>4</b>	<b>Validation MSES adaption for suction</b>	<b>37</b>
4.1	Porous flat plate experiment by Favre et al . . . . .	37
4.1.1	Development of the BL parameters . . . . .	38
4.2	Slot suction experiment by van der Hoeven . . . . .	38
4.2.1	Different suction models . . . . .	40
4.2.2	Slot suction for different suction levels . . . . .	40
4.3	Comparison with rFoilSuc . . . . .	41
4.4	Conclusion . . . . .	44
<b>5</b>	<b>Role, importance and assessment of the wake</b>	<b>45</b>
5.1	The active part in a BLS system: the pump . . . . .	45
5.2	Wake flow in a multi-element airfoil system . . . . .	47
5.2.1	Wake in an adverse pressure gradient . . . . .	48
5.2.2	Wake burst: a question of semantics? . . . . .	50
5.3	Assessment of the wake . . . . .	52
5.3.1	Gartshore's criterion . . . . .	52
5.3.2	Wake burst detection . . . . .	54
5.4	Conclusion . . . . .	56
<b>6</b>	<b>BLS configurations with minimal pump requirements for multi-element airfoils</b>	<b>59</b>
6.1	NLR7301 . . . . .	59
6.1.1	Comparison with experiment . . . . .	59
6.1.2	NLR7301 with suction . . . . .	60

6.2	MFFS026 . . . . .	66
6.2.1	MFFS026 with suction . . . . .	66
6.3	The application of suction to avoid wake burst: the general case . . . . .	68
<b>7</b>	<b>Conclusion &amp; Recommendations</b>	<b>73</b>
	<b>Bibliography</b>	<b>77</b>
<b>A</b>	<b>Closure relations</b>	<b>81</b>
A.1	Laminar closure. . . . .	81
A.2	Turbulent closure . . . . .	82
<b>B</b>	<b>Changelog MSES to MatSESuction</b>	<b>83</b>
<b>C</b>	<b>MSES &amp; convergence</b>	<b>89</b>
C.1	Convergence of the Newton solver . . . . .	89
C.2	A flap deflection of $26^\circ$ on the NLR7301 airfoil . . . . .	90
C.3	The NLR7301 airfoil at $\alpha = 15^\circ$ . . . . .	91
C.4	The NLF22 airfoil . . . . .	92

# LIST OF SYMBOLS

## LATIN

$c$		Airfoil chord
$C_{\mathcal{D}}$	$\frac{1}{\rho_e u_e^3} \int_0^1 \tau \frac{\partial u}{\partial \eta} d\eta$	Dissipation coefficient
$C_f$	$\frac{\tau_w}{\frac{1}{2} \rho_e u_e^2}$	Skin friction coefficient
$C_l$		2D lift coefficient (limited to airfoils)
$C_{l_{max}}$		2D maximum lift coefficient (limited to airfoils)
$C_L$		3D lift coefficient (wings)
$C_{L_{max}}$		3D maximum lift coefficient (wings)
$C_{\mu}$	$\frac{\rho_w v_w}{\rho_e u_e}$	Local suction coefficient
$C_p$	$\frac{p - p_{\infty}}{\frac{1}{2} \rho_{\infty} u_{\infty}^2}$	Pressure coefficient
$C_{\tau}$	$\frac{\tau_{max}}{\rho_e u_e^2}$	Shear stress coefficient
$\bar{C}_p$	$\frac{p - p_{min p}}{\frac{1}{2} \rho u_{min p}^2} = 1 - \left( \frac{u_e}{u_{min p}} \right)^2$	Canonical pressure coefficient
$c_p$		Specific heat capacity air at constant pressure
$C_q$	$-\frac{1}{u_{\infty} \rho_{\infty} c} \int \rho_w v_w d\xi$	Suction coefficient ( $\neq C_{\mu}$ )
$e$		Internal energy per unit mass
$E$	$\rho e + \frac{1}{2} \rho u^2$	Total energy per unit volume
$h$		Specific enthalpy
$H$	$\frac{\delta^*}{\theta}$	Shape parameter
$H_k$	$\frac{\int_0^1 1 - \frac{u}{u_e} d\eta}{\int_0^1 \frac{u}{u_e} \left( 1 - \frac{u}{u_e} \right) d\eta}$	Kinetic shape parameter
$H^*$	$\frac{\theta^*}{\theta}$	Kinetic energy shape parameter
$H^{**}$	$\frac{\delta^{**}}{\theta}$	Density shape parameter
$i$		Index of a grid node along the streamlines ( $\approx x$ -direction)
$j$		Index of a grid node along equipotential lines ( $\approx y$ -direction)
$\dot{m}$		Mass flow
$M$		Mach number
$p$		Pressure
$P$		Power
$q$		Dynamic pressure
$Q$		Volumetric flow rate
$Re$		Reynolds number
$s$		Streamwise distance along BL/wake trajectory
$T$		Temperature
$u$		Velocity in $x$ - or $\xi$ -direction
$u_s$		Slip velocity for turbulent BL model
$U_{slip}$	$\frac{u_s}{u_e}$	Normalized slip velocity
$v$		Velocity in $y$ - or $\eta$ -direction

## GREEK

$\alpha$		Angle of attack
$\alpha_{C_{l\max}}$		Angle of attack at maximum lift coefficient
$\alpha_{L=0}$		Angle of attack at zero lift
$\delta$		Boundary layer thickness
$\delta^*$	$\int_0^1 \left(1 - \frac{\rho u}{\rho_e u_e}\right) d\eta$	Displacement thickness
$\delta^{**}$	$\int_0^1 \frac{u}{u_e} \left(1 - \frac{\rho}{\rho_e}\right) d\eta$	Density thickness
$\delta_{\text{suction}}^*$		Displacement of the first inviscid streamline due to missing mass flow due to suction
$\delta_f$		Flap deflection
$\Delta n$		Total displacement of the inviscid streamlines
$\gamma$		Specific heat ratio of air
$\rho$		Density
$\tau$		Wall shear stress
$\theta$	$\int_0^1 \frac{\rho u}{\rho_e u_e} \left(1 - \frac{u}{u_e}\right) d\eta$	Momentum thickness
$\theta^*$	$\int_0^1 \frac{\rho u}{\rho_e u_e} \left(1 - \frac{u^2}{u_e^2}\right) d\eta$	Kinetic energy thickness
$\xi$		Boundary layer coordinate (stream wise)
$\eta$		Boundary layer coordinate (normal to surface)

## SUBSCRIPTS

$\infty$	Freestream
$a$	Average
aw	Adiabatic wall
e	Edge of boundary layer
(eq)	Equilibrium
$t$	Stagnation (total) quantity
w	Wall (may indicate transpiration values in case of $v$ and $\rho$ )

## SUPERSCRIPTS

1,2	In conjunction with $\delta_f$ : number of flap
$\bar{x}$	Reynolds averaged value of quantity ' $x$ '
$x'$	Fluctuating Reynolds value of quantity ' $x$ '

## ABBREVIATIONS

BL	Boundary layer
BLS	Boundary layer suction

# 1

## INTRODUCTION

High lift systems are complex and heavy systems, making up to 5.5% of the weight of commercial airliners [5]. Despite that they are still indispensable to reconcile optimal cruise performance of the aircraft with an acceptable take-off and landing performance with regard to required runway length. The use of complex high lift devices became increasingly necessary with the advent of the jet age: the wing and used airfoils of the aircraft needed to be designed in such a way so they could cope with the dramatic increase in cruising speed. Unfortunately this was at the expense of the high lift capabilities of the airfoil. Relatively small changes in  $C_{L_{max}}$  can already have a large impact on the aircraft performance: Wimpres estimates that a 5% increase in  $C_{L_{max}}$  allows a 20% higher payload during take off, and during landing the same increase in  $C_{L_{max}}$  allows an even higher increase in payload of 65% [6]. Another example due to Meredith estimates that an increase in the maximum lift coefficient of 1% allows an increase in the payload of 2000 kg [7]. To reconcile the requirements for a high speed airfoil with an acceptable take-off and landing performance, retractable multi-element flap and slats were designed. Although such designs successfully increase  $C_{l_{max}}$  (and, hence,  $C_{L_{max}}$ ) they are also heavy and require a lot of maintenance. As a result a definitive trend towards lower complexity high lift systems is already ongoing since the 1970's<sup>1</sup> [1]. But also to the increasing insight into the problem and ingenuity of the high-lift multi-element airfoil designs is a limit and the designs cannot keep on getting simpler without losing their original purpose. Other approaches are therefore actively sought after. One of the methods that has already proven to be able to increase high lift performance is active boundary layer control and it is one of the directions in which research is directed to develop the lighter and simpler high lift devices [8–10].

Active boundary layer control is by now an old and mature research area, but it has the possibility of increasing camber — in the case of a flap this would amount to an increased flap deflection — while preventing separation, thus allowing smaller and simpler flap mechanisms. The main problem with active boundary layer control is the often high power requirements to achieve optimal performance. In an attempt to make up for the power requirements and minimize the weight penalty of a boundary layer suction or blowing system, systems that use an already existing low- or high-pressure area (depending on the application), e.g. in the engine, are interesting to pursue [2]. Despite the ingenuity of such solutions they are quite complex and inevitably require additional power generation from the engine. But one could also imagine using for example the low pressure zone under influence of the tip vortex at the wing tip. Strictly speaking this under pressure is also not 'free' since the induced drag of the wing tip vortices must be compensated for by generating extra propulsive power, however it must be acknowledged that these wing tip vortices are virtually unavoidable anyway: the low pressure zone is a 'given'. Using this potential of under pressure may be useful to create a boundary layer suction system that does not require additional power generation when compared to the same wing configuration without such a system, while at the same time possibly reducing the complexity (and thus weight) of the system.

It is however important to acknowledge that the available 'naturally occurring low-pressure zones' on the wing surface (or elsewhere on the aircraft) are not very strong. Therefore the requirements for the boundary layer suction system become a very important aspect in the design and application of the boundary layer

---

<sup>1</sup>Figure 2.3 illustrates this by showing the historical evolution of high lift systems

suction on the airfoil. While usually the research in the presented area is focused on maximizing the maximum lift coefficient at the cost of high system requirements (such as the required under pressure) the aim of this study is to look at the possible gains due to boundary layer suction on an airfoil while minimizing the requirements for the boundary layer suction system, more specifically the requirements for the pump system driving it. Losing the additional lift that could be achieved with a more demanding system should be compensated by a reduction in complexity, weight and the absence of the need for additional power generation.

The objective of this thesis is thus to study boundary layer suction systems with minimal pump requirements (i.e. suction with low volumetric flow and in relatively high static pressure areas) aimed at increasing the lift coefficient on a multi-element airfoil. This will be done by modifying an existing inviscid-viscid interaction flow solver to include boundary layer suction followed by an investigation into the delay of decambering of the system by boundary layer suction.

The objective of the project is reflected in the structure of this report. In chapter 2 a general discussion about multi-element airfoil flow fields and boundary layer suction is given. This is a theoretical discussion based on literature. On the application side the adaption of an inviscid-viscid flow solver (MSES) for boundary layer suction is discussed in chapter 3. This chapter presents also the required theoretical knowledge to achieve this. Following this chapter, chapter 4 treats the comparison of the results of MSES including suction with available (experimental) data, in other words: a validation of the code. With the knowledge and the tools available the investigation into avoiding the loss of lift with minimal boundary layer suction can be commenced. In order for this a rigorous discussion of the role and importance of the wake in a multi-element airfoil flowfield is required which is given in chapter 5. Chapter 6 then presents some critical cases with significant loss of lift due to wake phenomena and the effect of suction to relieve this problem. Figure 1.1 shows the structure of the report in a visual form. To end, chapter 7 presents the conclusions that can be drawn from the results in chapter 6 and recommendations concerning the adaption of MSES and future research.

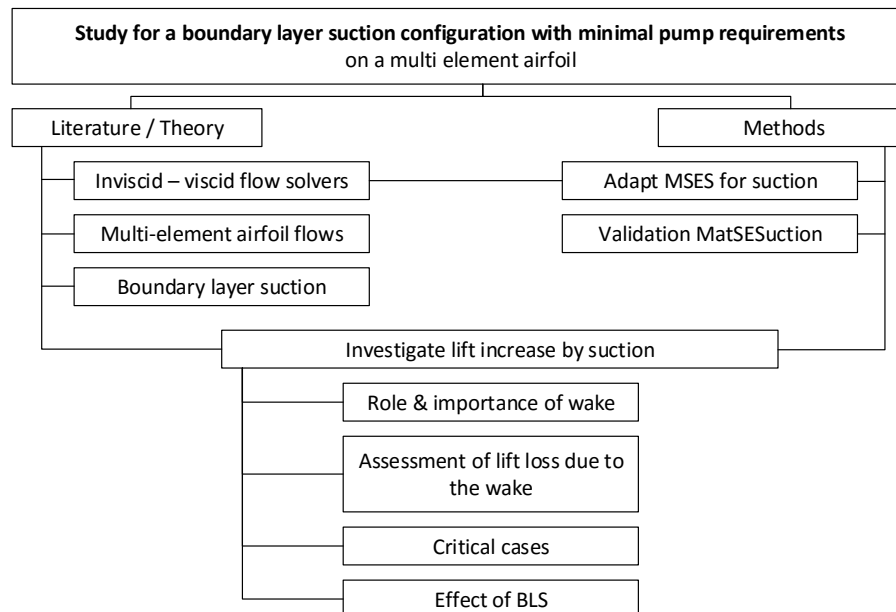


Figure 1.1: Roadmap for this thesis.

# 2

## THEORETICAL BACKGROUND

This project aims to investigate *boundary layer suction* for a *multi-element airfoil system*. This chapter gives a general theoretical background about these two subjects. The [first section](#) discusses high-lift configurations, the working principles and the challenging problems concerning solving their flowfield. The same applies to the [following section](#) for boundary layer suction. To avoid unnecessary repetition, the theory for adapting the integral boundary layer relations and closure relations for suction can be found in chapter 3. For the same reason the reader is referred to chapter 5 for a thorough discussion of the development of the wake; section 2.1.5 also discusses the wake phenomenon but limited to the parts that are not very relevant to the discussion in chapter 5.

### 2.1. HIGH LIFT SYSTEMS

High lift devices are necessary to improve the performance of aircraft during landing and take-off, and in specialized cases, also during manoeuvring. By increasing the maximum lift coefficient either a higher payload can be attained or lower stalling speeds (or smaller turn radii). The focus will be on multi-element airfoils — especially flaps — and the associated flow fields. A lot of attention is also paid to the different phenomena that cause the flow field to break down. Next to that it is also explored how much of an impact an improvement in  $C_{l_{max}}$  has on the aircraft performance and how much is desirable from high lift devices.

#### 2.1.1. INTRODUCTION TO HIGH LIFT SYSTEMS

The only way to increase the high lift performance of an aircraft when necessary is by ‘reshaping’ the wing temporarily, because for a fixed airfoil geometry the maximum lift coefficient is obviously also fixed. This is achieved by the movable devices: ‘flaps’ at the trailing edge and ‘slats’ at the leading edge. They may or may not be completely detached from the main airfoil/wing geometry, but when they are, one is dealing with a multi-element airfoil.

Flaps increase the effective camber of the airfoil, which — as long as the flow does not separate — increases the amount of air that is being deflected downward and hence increasing lift. It is important to acknowledge the basic fact that deflecting the flap does not only change the flow near the trailing edge, the whole flow field around the airfoil is changed: not only the streamlines around the flap are deflected down, the incoming streamlines are deflected upward and obviously also the stagnation point moves more towards the lower part of the airfoil. This results in the lift curve being shifted upwards by a certain  $\Delta C_l$ .  $C_{l_{max}}$  is increased by approximately the same amount, but it occurs at a slightly lower angle of attack.

The effect of slats is somewhat more complicated, but the main idea is that the slat mitigates the high pressure gradient on the main airfoil, hence preventing separation due to a too large adverse pressure gradient. A slat merely increases  $\alpha_{C_{l_{max}}}$  and thus  $C_{l_{max}}$  itself. Figures 2.1 and 2.2 show the effect of a flap and a slat respectively on the lift curve. When dealing with multi-element airfoils the interactions between the different elements are much more subtle and complicated than explained above, this is treated in section 2.1.3. [11]

Figure 2.3 shows how multi-element airfoils have become less complex over the years in an attempt to save weight and lower the maintenance costs.

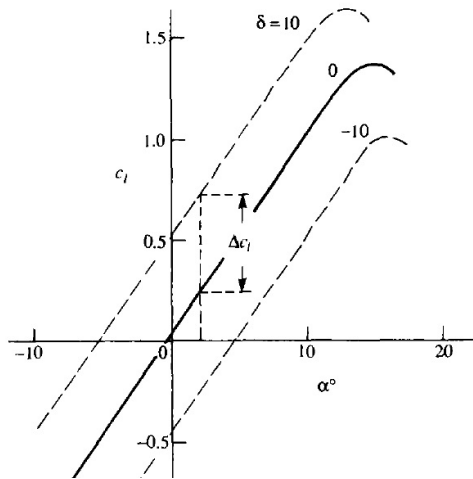


Figure 2.1: Effect of flap deflection (dashed lines) on lift curve. [11]

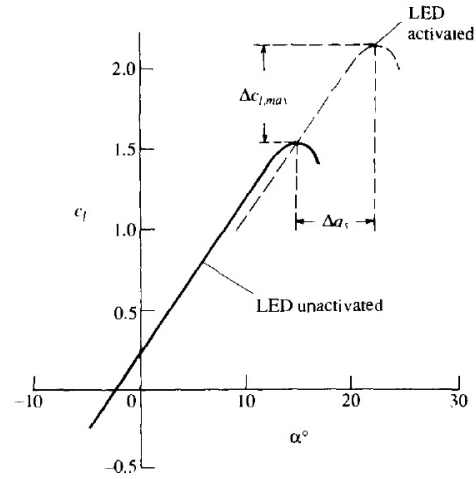


Figure 2.2: Effect of slat deflection on lift curve. [11]

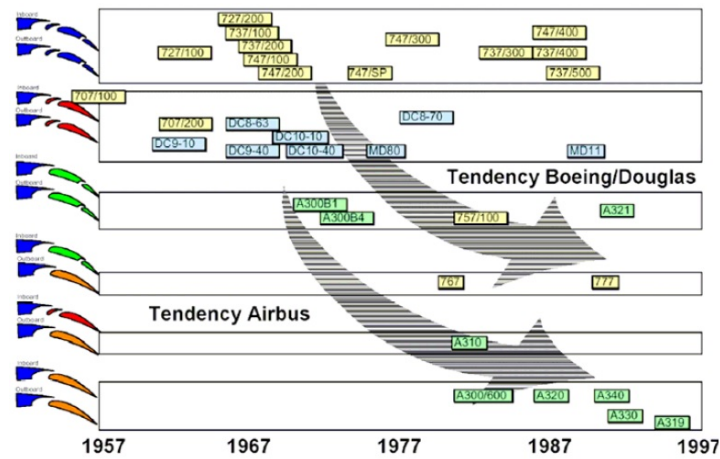


Figure 2.3: Evolution of high lift systems. [1]

### 2.1.2. MULTI-ELEMENT AIRFOIL FLOW FIELDS

Figure 2.4 summarizes the what flow phenomena influence the flow field over a multi-element airfoil [12]. The following phenomena can be distinguished:

- Strongly curved boundary layers: static pressure can significantly vary throughout the boundary layer due to the large curvature of them.
- Compressible flow: the extremely high velocities over the first element (the slat in this case, see for example the velocity distribution in figure 2.8) can cause local supersonic velocities, even at freestream Mach numbers of only 0.2 [12].
- Recirculation zones: in cavities preceded by 'sharp' edges a recirculation zone is formed.
- Relaminarization: due to the very strong favourable pressure gradient near the leading edge(s), turbulent boundary layers may relaminarize.
- Wakes: the exhausted or low-energy flow resulting from the boundary layers that leave an upstream element leave a wake that is influenced by downstream elements. Under influence of the adverse pressure gradient over downstream elements the wake may grow and merge with the boundary layer of a downstream element. These are called *confluent boundary layers*. Under influence of adverse pressure gradients the wake may also experience flow reversal without being in contact with any surface. This is

referred to as *wake bursting* or *off-the-surface separation* (in figure 2.4 it is referred to as the ‘backflow region’).

- Separation: just like for simple airfoils, separation causes the flow field around the airfoil elements to break down with a major loss in lift as a result.

In order to assess the flow field around a multi-element airfoil all these phenomena — or at least as much as possible — should be captured by the used method. Doing this computationally proves it to be extremely difficult to capture all these phenomena, and as a result predicting high-lift flows remains a challenging problem.

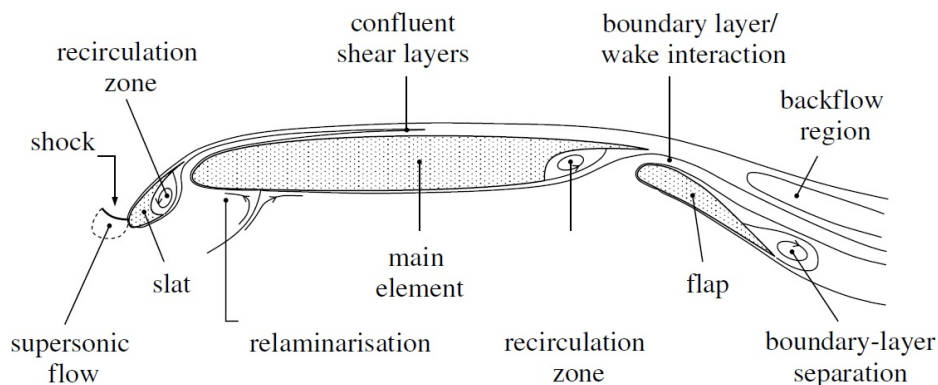


Figure 2.4: Phenomena influencing the flow over a multi-element airfoil. [12]

### 2.1.3. WORKING PRINCIPLES OF MULTI-ELEMENT AIRFOILS

Many theories exist to explain the working principles behind multi-element airfoils. A common explanation is that the slots between the multiple elements act as a jet<sup>1</sup>: the slot connects a region of high pressure on the lower surface of an element with the low pressure upper surface on the next element and as such the boundary layer is energized by a ‘blowing’ effect of the slot. This view is mistaken<sup>2</sup> as pointed out by A.M.O. Smith in his now classic and well-known paper on high lift aerodynamics [16]<sup>3</sup>. The flow field around multi-element airfoils is highly complex and as such the working principles behind it are as well. They are discussed in the next subsections, but first a rather basic recap is given about the interaction of the flow around a single airfoil and the boundary layer and how this affects separation. This will be useful in understanding the following discussion about the working principles of multi-element airfoils.

The flow around the airfoil and the boundary layer, or the ‘inviscid’ flow, is what causes lift. On the upper surface the flow is accelerated due to the shape of the airfoil, creating (much) higher velocities than the freestream velocity. However, this flow must also be decelerated again; in the case of a simple airfoil this means that the flow at the trailing edge is decelerated to values equal or lower than the freestream. Decelerating the flow creates an adverse pressure gradient, which causes the flow in the boundary layer to become unstable, turbulent and eventually to separate. A good airfoil is designed such that this deceleration process takes place in such a manner that the boundary layer can cope with the adverse pressure gradient (caused by the deceleration) without separating. When the desire is to maximize lift the peak velocities must increase or the region over which the flow has a high velocity must be increased. Both options mean that the boundary layer must cope with a larger pressure gradient to reach freestream conditions at the trailing edge. One can look at it as if the flow puts ‘stress’ on the boundary layer; and this boundary layer only allows a certain amount of stress before it separates.

<sup>1</sup>Even the celebrated aerodynamicist Prandtl and noted aerodynamicists Abott and Doenhoff suggested this to be the working principle behind multi-element airfoils. [13, 14]

<sup>2</sup>Supported by experimental data, e.g. [15].

<sup>3</sup>The paper *High Lift Aerodynamics* by A.M.O. Smith is still exceptionally relevant when it comes to multi-element lift and a lot of the insights presented in this section are based on this paper.

Having multiple lifting elements helps to ‘manage’ the flow in such a way that the ‘stress’ it puts upon the boundary layer is below a maximum allowable value that would cause it to separate. How this is achieved is explained in the next subsections. However, before diving into this important matter the concept of the canonical pressure coefficient is briefly outlined.

### MUTUAL INTERACTION

The influence of an upstream on a downstream element or the *slat effect* is such that it relieves the pressure peak on the downstream element. This can be most easily understood by visualizing a vortex as being the upstream element (e.g. a slat): the velocities induced by this vortex (or in practice, the upstream element) run counter to the velocities around the leading edge of the main element (downstream element) and reduce the high velocities in this region; this is illustrated qualitatively in figure 2.5. Of course, this leads to a reduction in lift over the downstream element, but with a well designed slot between the up- and downstream element the maximum lift that can be attained by the overall system increases. By reducing the pressure peak, higher angles of attack can be reached and therefore the slat effect usually increases the maximum angle of attack and as such also the maximum lift coefficient.

The influence of a downstream on an upstream element or *the circulation effect* is such that it changes the angle of the flow at the trailing edge: the angle of attack is effectively increased. Given that the flow does not separate, in order for the boundary layer to leave the trailing edge ‘smoothly’ (i.e. either the trailing edge is a stagnation point or the flow of upper and lower surface are equal in magnitude and direction at the trailing edge: the Kutta condition) the circulation over the airfoil must increase. In practice this means that over the upper surface the flow will be accelerated and create more underpressure<sup>4</sup>. This is shown in figure 2.6 with the rear element simulated as a simple vortex. A flap helps to increase the circulation (and consequently lift) without having to increase the angle of attack which causes pressure peaks at the nose of the airfoil due to the (relatively) small radius of the leading edge.

The high velocities at the leading edge of a downstream element also have the effect that the flow leaving the upstream element is ‘dumped’ into a region of lower pressure. This region is the result of the proximity of the leading edge (and it’s associated low pressure peaks) of the downstream element. This is the *dumping effect*. This relieves the adverse pressure gradient on the upstream element; thus providing a larger margin against separation. In figure 2.8 the ‘dumping velocities’ are highlighted with red arrows. Note that they are considerably larger than the freestream velocity, except for the flap where the dumping effect is absent and the velocity drops to a value lower than the freestream velocity.

The mutual interaction between multiple aerodynamic elements is nicely summarized in figure 2.7: due to the slat effect the velocity peaks on downstream elements are relieved, while due to the circulation effect the velocity over upstream elements is increased when compared to the situation of a simple airfoil. As a result, the first element has a very high velocity peak which poses the problem of slowing the flow down again while avoiding separation, but in a carefully designed multi-element airfoil this is overcome with off-the-surface pressure recovery, explained in section 2.1.3 and 2.1.5. Figure 2.8 also shows the mutual interaction very nicely for a more realistic multi-element airfoil. By looking at the canonical form of the velocity distribution (intermittent blue line), one can easily see that the slat and the flap are designed in such a way that both the flap and the slat relieve the adverse velocity (and as such pressure) gradient of the main element, while having a smaller margin against separation themselves.

### OFF-THE-SURFACE PRESSURE RECOVERY

As explained in section 2.1.3 the trouble with creating high lift is dealing with the high adverse pressure gradient resulting from the low-pressure peak. If this adverse pressure gradient is too large the boundary layer will eventually separate. Experiment has shown that if the boundary layer has left the surface (so it is not really a boundary layer any more, but rather a ‘wake’) it can sustain larger adverse pressure gradients without becoming unstable or grow than a boundary layer in contact with the surface [17]<sup>5</sup>. This allows a faster recovery of the pressure without the detrimental effects of separation of the boundary layer. By looking at the the scale on the right of figure 2.8 it can be seen that the velocity at the trailing edge of the flap has dropped to 0.05 times the maximum velocity over the slat. This deceleration implies a very large adverse pressure gradient and if — hypothetically — the boundary layer of the slat had still been in contact with the surface at this point it

<sup>4</sup>This is comparable to just adding a plain flap: a plain flap adds more camber (which in turn requires more circulation to meet the Kutta condition at the trailing edge) by changing the airfoil. The slotted flap does the same, but does so not by changing the airfoil itself but by influencing the flow at the trailing edge!

<sup>5</sup>The paper of Gartshore was unfortunately not available, but ref. [16] repeats the most interesting results for this discussion ([16], p. 515-516)

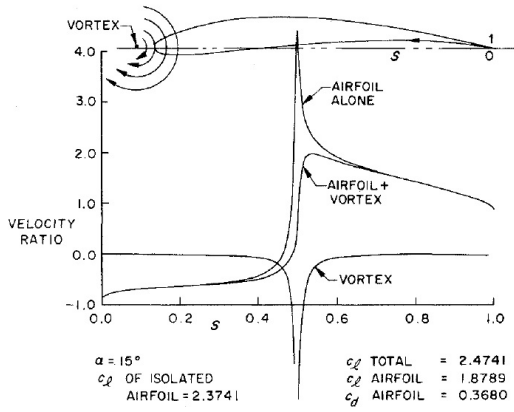


Figure 2.5: Slat effect. The slat is represented by a single vortex. [16]

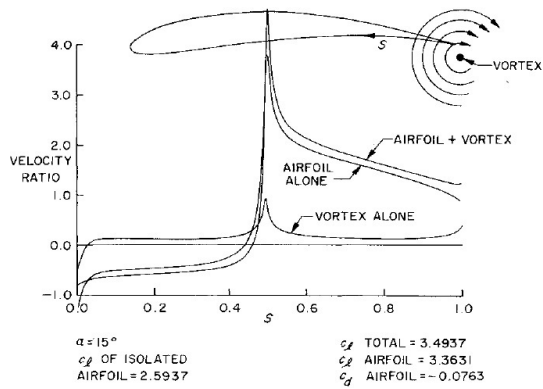


Figure 2.6: Circulation effect. The flap is represented by a single vortex. [16]

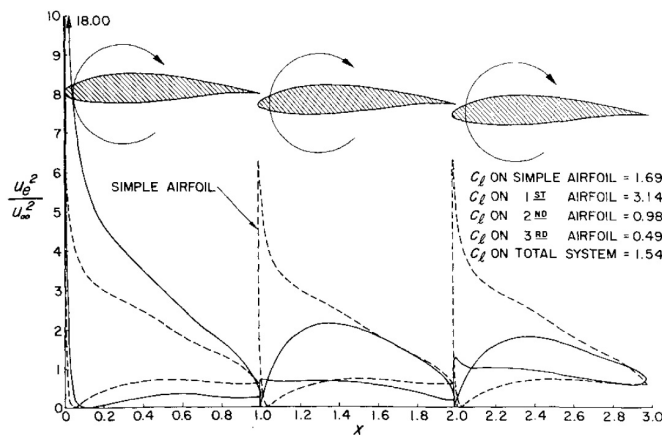


Figure 2.7: Mutual interference of multiple airfoil elements. [16]

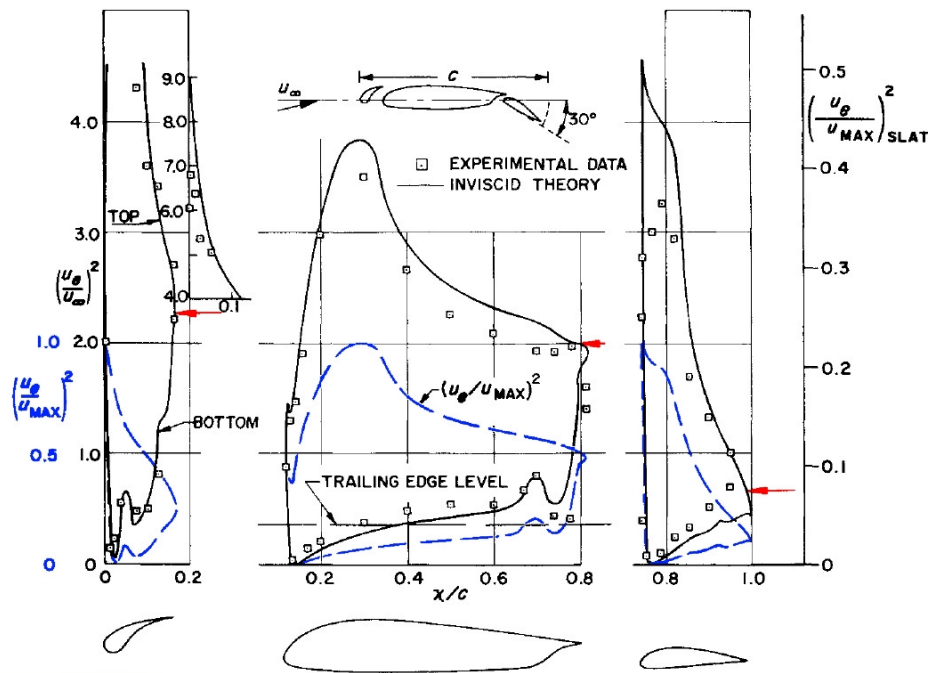


Figure 2.8: A multi-element airfoil with slat and flap. The velocity distribution is shown wrt. the freestream speed  $\frac{u_e}{u_\infty}$  (solid black line) and the maximum velocity over the respective element  $\frac{u_e}{u_{MAX}}$  (intermittent blue line, also known as the 'canonical' form which is more useful in determining the margin before separation). On the right a scale is shown that shows the velocity wrt. the maximum speed over the slat. The red arrows denote the 'dumping velocity' at the trailing edge of the elements (from slat to flap the dumping velocity ratio  $\frac{u_e}{u_\infty}$  is 2.28, 2 and 0.67 respectively). [16]

would have been for sure separated. In order for the off-the-surface pressure recovery to work, it is obviously important that the wake leaving upstream elements does not grow under influence of the rising pressure over downstream elements and — at worst — merges with the boundary layer over the downstream elements. But, as already explained, the wake can handle a larger pressure gradient before it grows than a boundary layer that is still in contact with a surface can before it separates. This phenomenon is further explained in section 2.1.5.

#### FRESH BOUNDARY LAYER

A new boundary layer is formed on each element in the multi-element airfoil and since a boundary layer keeps growing when in contact with a surface ‘breaking up’ the airfoil into several elements allows the boundary layer to remain relatively thin over each element. Thinner boundary layers can withstand larger adverse pressure gradients, thus aiding to increase lift.

#### 2.1.4. FLOW SEPARATION

The influence of the outer flow on the boundary layer and vice versa is often classified into two categories: *weak* and *strong interaction*. In the first case the boundary layer is well defined, and there is a clear ‘hierarchy’ between the outer flow and the boundary layer — in other words, they are clearly distinguishable from each other. In this case, the boundary layer has a displacement effect on the outer flow which in turn changes the velocity distribution on the edge of the boundary layer which changes the behaviour of the boundary layer again and so on... This is also reflected in the design of viscid aerodynamic panel codes: the outer flow and the boundary layer are calculated alternately until their solution converges. The fact that the boundary layer flow is calculated separately from the outer flow allows the boundary layer equations by Prandtl to be used to calculate it. The (incompressible) boundary layer equations are shown in equations (2.1) for completeness:

$$\text{Continuity: } \frac{\partial u}{\partial x} + \frac{\partial v}{\partial y} = 0 \quad (2.1a)$$

$$\text{x-momentum: } \frac{\partial u}{\partial t} + u \frac{\partial u}{\partial x} + v \frac{\partial u}{\partial y} = -\frac{1}{\rho} \frac{\partial p}{\partial x} + \mu \frac{\partial^2 u}{\partial y^2} \quad \text{with} \quad -\frac{1}{\rho} \frac{\partial p}{\partial x} = -\frac{1}{\rho} \frac{dp_e}{dx} = \rho u_e \frac{1}{\rho} \frac{du_e}{dx} \quad (2.1b)$$

$$\text{y-momentum: } \frac{\partial p}{\partial y} = 0 \quad (2.1c)$$

The strong interaction on the other hand is of a very different nature: the hierarchy between the boundary layer and the outer flow vanishes. Prandtl’s boundary layer equations lose their validity because a singularity appears. The cause of this singularity was first suggested by Goldstein [18] to be the prescribed pressure at the outer edge of the boundary layer and the fact that the pressure is constant throughout the boundary layer, which was later confirmed [19]. This is illustrated in figure 2.9: the graph represents a typical dependence between the boundary layer thickness and the (prescribed) outer velocity at a certain chordwise station along the airfoil. A minimum is visible, the minimum is associated with the appearance of a singularity and the onset of separation. Below this minimum value of  $u_e$  no solution to equations 2.1 exists: the boundary layer and the outer flow must be calculated simultaneously<sup>6</sup>. It should be clear that the topic discussed in this section, i.e. flow separation, is of the second kind: a strong interaction.

As is apparent from the preceding paragraphs, the pressure distribution imposed by the outer flow on the boundary layer has a large influence on the behaviour of the boundary layer itself. The stability of the boundary layer, the point of transition (laminar to turbulent) and the separation point are heavily influenced by the presence of an adverse pressure gradient — the pressure increases in the flow direction. While being a phenomenon with great importance that is a thoroughly studied subject on itself, the stability of boundary layers do not have a great influence on the outer flow, the shape of the boundary layer does not change by it and as a result neither does the outer flow and the entire flow field. Due to the rapid thickening of the boundary layer during the transition from laminar to turbulent flow, this aspect does have some influence on the outer flow and the resulting properties such as the lift produced by an object in the flow. But by far the most radical change in the flow field is due to flow separation of the boundary layer. By definition a boundary layer is a region in the flow where viscous forces between the fluid elements are dominant or at least of the same order of

<sup>6</sup>By looking at figure 2.9 one can see that for a prescribed displacement thickness a solution for  $u_e$  always exists, leading to the development of inverse and semi-inverse methods to calculate the outer and boundary layer flow, removing again the necessity to calculate them simultaneously.

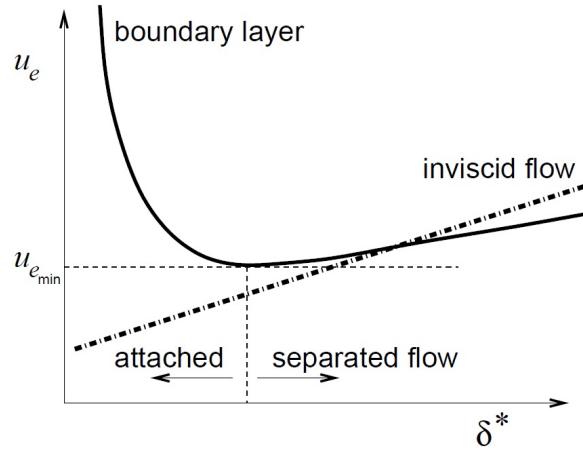


Figure 2.9: Typical dependence between edge-velocity and displacement thickness of a boundary layer. [19]

magnitude as inviscid flow properties. Under influence of the viscous forces, the fluid elements lose so much of their momentum — or kinetic energy — that not enough momentum is left over to overcome an ‘obstacle’ in the form of an adverse pressure gradient. Instead, the fluid particles in the boundary layer come to a halt and even reverse direction, creating reversed flow in the boundary layer. This process is visualized over time in figure 2.10, but the same process can also be imagined as taking place over a certain distance. That the friction forces and the adverse pressure gradient work in unison to cause flow separation is evidenced in figure 2.11: a flow against a wall perpendicular to the flow (vertical wall) causes a stagnation point on the wall and an adverse pressure gradient experienced by the ‘incoming’ flow. However, in the absence of frictional forces there is no separation as is the case in figure 2.11a. By adding a wall tangential to the flow (horizontal wall) frictional forces are introduced, i.e. a boundary layer is created. In this configuration the flow separates from the horizontal wall (figure 2.11b). Note however that it is not absolutely necessary for a wall to be present to have flow ‘separation’. The viscous forces can also be present due to the velocity difference between the retarded flow in the wake of upstream elements and the outer flow. If an adverse pressure gradient is present in these conditions, this can lead to ‘off-the-surface flow separation’ or ‘wake bursting’. This is an important phenomenon when studying multi-element airfoils and it is more thoroughly studied in section 2.1.5.

The streamlines of a separated (or nearly separated) flow depart from the wall at a certain point, the separation point. Figure 2.14 shows the streamlines and the separation point of a separated flow near the wall. Traditionally, the separation point is defined as the point where the velocity gradient perpendicular to the wall  $\left(\frac{\partial u}{\partial y}\right)_{wall}$  becomes zero (and as a result, also the wall shear stress becomes zero):

$$\text{Separation at: } \tau_w = \mu \left(\frac{\partial u}{\partial y}\right)_w = 0 \quad (2.2)$$

While this literature study focuses on external flows, separation is as much a phenomenon of internal flows as it is for external flows. Figures 2.15 and 2.16 shows how boundary layer suction prevents separation around a cylinder and on a diffuser respectively. The causes of the separation are of course identical: the boundary layer separates under influence of the adverse pressure gradient.

#### PREDICTING SEPARATION

In practice (when using inviscid-viscid interaction codes) it proves to be rather cumbersome to find the separation location based on the criterion in equation (2.2). To remedy this, a vast number of other criteria have been proposed. A few of them that can be calculated in conjunction with integral boundary relations are presented below:

- A very simple but (too) rough method to estimate the separation is coupling separation to an assumed *minimum pressure coefficient* that can be attained without separation taking place. Minimal values of  $C_p = -10$  to  $-13$  are used [21] and can only possibly be used to predict leading edge separation.

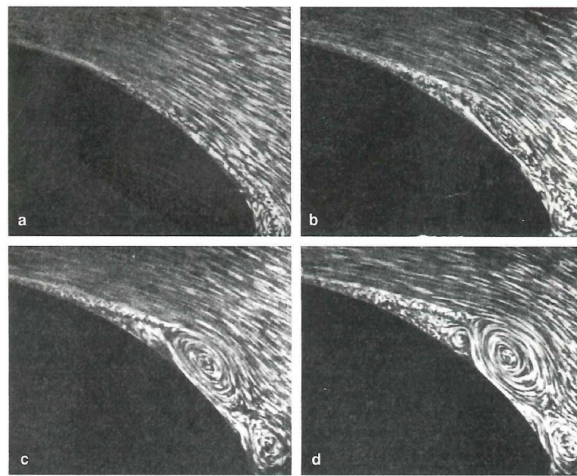
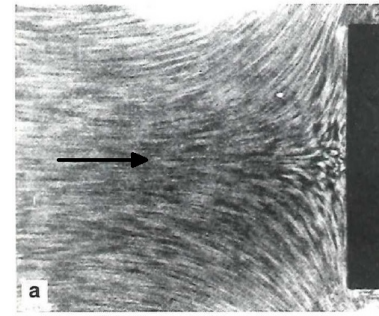
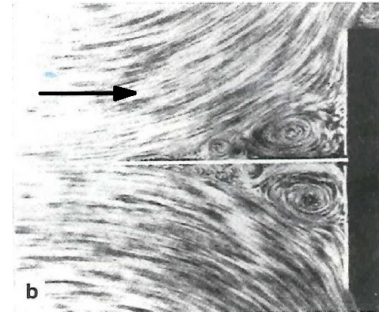


Figure 2.10: Development of separation over time. [20]



(a) Without wall: no separated flow.



(b) With wall: separated flow.

Figure 2.11: Flow experiencing an adverse pressure gradient without a wall (a) and with a wall (b). [20]

- *Loftin's criterion* uses the canonical pressure coefficient: it states that the maximum value of  $\bar{C}_p$  is 0.88 after the start of recovery [21].
- *Stratford's limiting pressure gradient*: Stratford's method is based on the development of the canonical pressure coefficient  $\bar{C}_p$  and can be used for both laminar and turbulent flows [22]. For laminar flows the equation simply reads:

$$\text{Separation at: } \sqrt{\bar{C}_p} \left( x \frac{d\bar{C}_p}{dx} \right) = 0.102 \quad (2.3)$$

For turbulent boundary layers one has to take into account that the boundary layer may not be turbulent right from its onset at the stagnation point; however the criterion itself is very similar:

$$\begin{aligned} \text{Separation at: } & \bar{C}_p \sqrt{x' \frac{d\bar{C}_p}{dx}} (10^{-6} Re_{x'})^{-0.1} = k \\ \text{with } & Re_{x'} = \frac{U_e(x')x'}{\nu} \quad (\text{Local Reynolds number}) \\ k = & \begin{cases} 0.35 & \frac{d^2 p}{dx^2} \leq 0 \quad (\text{Concave recovery}) \\ 0.39 & \frac{d^2 p}{dx^2} > 0 \quad (\text{Convex recovery}) \end{cases} \end{aligned} \quad (2.4)$$

Stratford's criterion is known to be rather conservative, although this is not the case for laminar separation bubbles. On the contrary, investigations at the TU Delft showed that the constant in equation (2.3) should be decreased to predict laminar separation bubbles [21].

- By using the *shape factor* as criterion, one ensures that the actual boundary layer properties are included in the assessment. The value of the shape factor can be coupled to the shape of the velocity

profile of the boundary layer, see figure 2.12: at high values for the shape factor the velocity clearly shows that the flow is much closer to separation ( $(\frac{\partial u}{\partial y})_{wall}$  becomes zero).

$$\text{Separation at: } \frac{\delta^*}{\theta} = H \approx [1.8, 2.4] \tag{2.5}$$

Different sources recommend other values for  $H_{sep}$ , e.g. also [2.2, 2.4] is often put forward. Although this may at first seem to make a large difference, in practice it does not since close to separation  $H$  increases very rapidly. The shape factor method is generally accepted as being the most reliable. Arguably the most well known method which uses this criterion is due to Head, in which he uses a.o. his 'entrainment relation' to close the integral BL equations [23].

By using one of the simple methods which just prescribe a fixed  $C_p$  the 'path' (on the pressure distribution plot) is not taken into account at all in the assessment of separation and therefore very crude. Stratford's method does take into account the development of the pressure recovery to a certain extent by incorporating  $\bar{C}_p$ ,  $x$  and last but not least  $\frac{d\bar{C}_p}{dx}$ . However, take a look at figure 2.13: at a certain point 's' the method will predict separation, but it cannot make the distinction between the several 'paths' towards it (e.g. a, b or c). By using the shape parameter  $H$  as the separation criterion the properties of the boundary layer are taken into account and a difference between the several paths can be made. Therefore, as mentioned before, this method is taken as the most reliable. Cebeci et al. compared several separation prediction methods with experimental data for turbulent boundary layers and concluded that [24]:

- Method's which predict separation based on fixing  $C_{p_{min}}$  do not give good results.
- Head's method (or, more generally, the shape factor method), Stratford's method and the differential CS method (designed by the authors, not discussed here) give similar and satisfactory results.
- Stratford's method is slightly conservative.

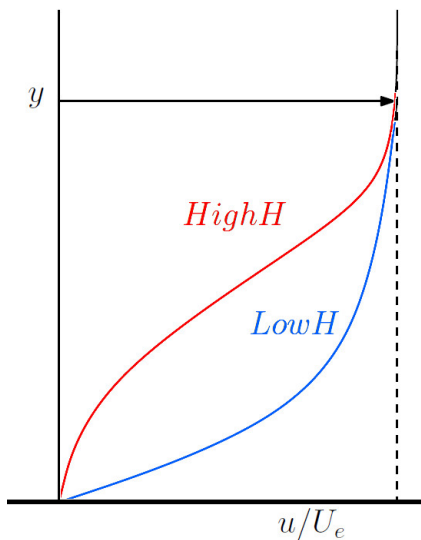


Figure 2.12: Dependence of the velocity profile on the shape factor  $H$ . [21]

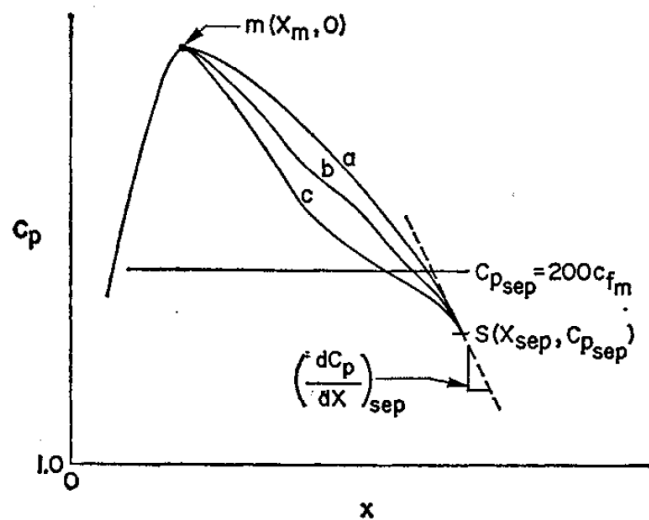


Figure 2.13: Schematic for comparison of separation criteria. [24]

SEPARATION ON AIRFOILS

The causes of flow separation have been abundantly discussed in the previous section, basically it boils down to the decelerating flow in the boundary layer not being able to overcome the adverse pressure gradient which eventually causes flow reversal. How does this affect the flow over an airfoil? Figure 2.17 shows the difference between the pressure around an airfoil for a separated (solid line) and non-separated (dashed line) flow. Near the leading edge the pressure of the separated flow is much higher, and combined with the fact that the part

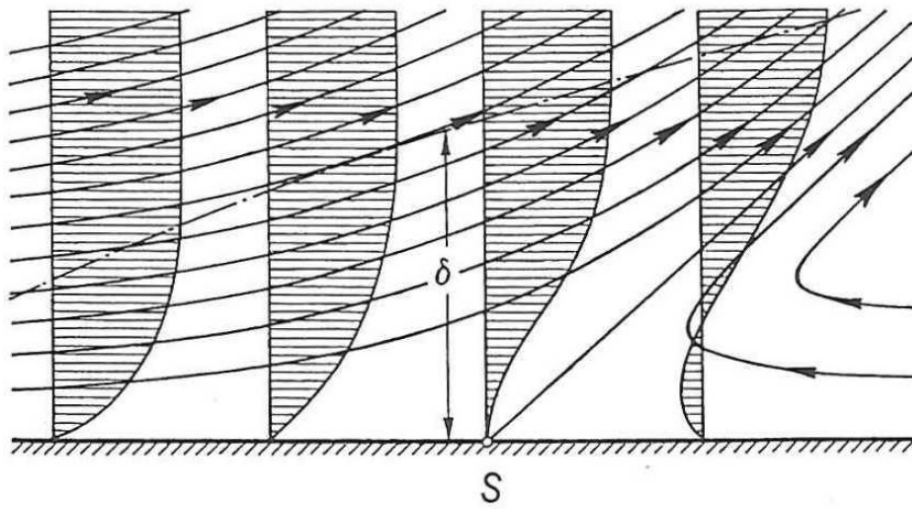


Figure 2.14: Streamlines of the flow in a boundary layer near the separation point (S). The displacement thickness of the boundary layer is also indicated ( $\delta$ ). Also some velocity profiles near the separation point are shown. Notice that the two velocity profiles most downstream contain an inflexion point, which is a necessary condition for separation. [20]

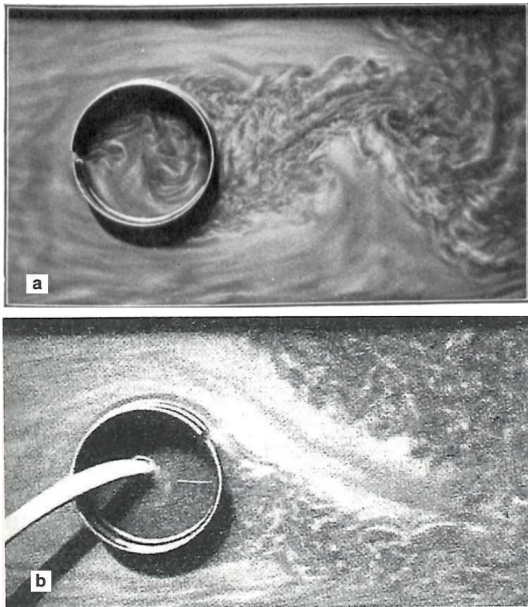


Figure 2.15: Flow around a cylinder without (a) and with suction (b). [25]

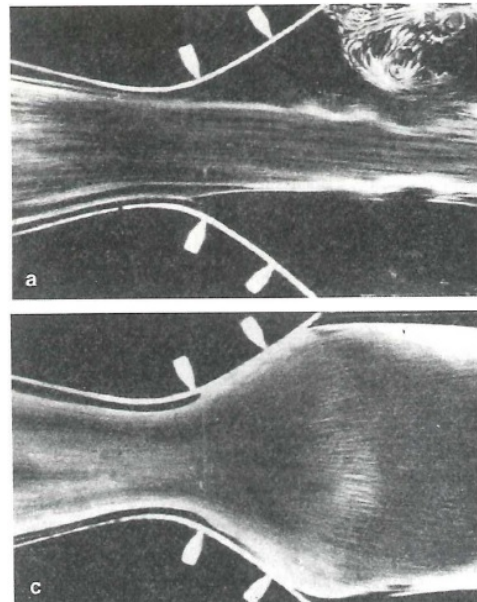


Figure 2.16: Flow in a diffuser without (a) and with suction (c). [20]

of the surface of the airfoil where much of the under pressure is lost is now aligned almost perpendicular to the lift direction, this is the main cause for a dramatic loss of lift. The sudden drop in lift due to separation means that the onset of separation on an airfoil is more or less coincident with the maximum lift coefficient it can produce ([20]). Near the trailing edge on the other hand the pressure does not recover to its free stream value when the flow is separated and hence the pressure is smaller when compared to the non-separated case. Not being able any more to compensate for the (high) pressure over the lower part of the airfoil, this is the reason for a major increase in drag. [11]

A distinction can be made between several stall ‘modes’:

- *Leading edge stall*: the origin of the separation is located at the leading edge and as a result separation immediately affects the flow over the complete airfoil resulting in an abrupt stall. This type of stall can be expected for airfoils with thickness ratios ranging from 10–15%.
- *Trailing edge stall*: not surprisingly, separation originates at the trailing edge for this type of stall. This allows the separation region to gradually grow with increasing angle of attack. This results in a more moderate stall behaviour of the airfoil, but lower values for  $C_{l_{max}}$  are usually found. This type of stall can be expected for thicker airfoils.
- *Thin airfoil stall*: this may seem not such an interesting case from a practical point of view, but it introduces the important concepts of the *separation bubble* and *reattachment*. Near the leading edge of a very thin airfoil a *separation bubble* appears where the flow separates, even at very low angles of attack, but later on the flow reattaches again to the airfoil surface. The separation bubble forms due to the laminar flow near the leading edge separating (laminar flow separates earlier than turbulent flow), it transitions to turbulent flow while detached from the surface and when the boundary layer comes into contact with the surface again it reattaches again. Figure 2.19 shows a schematic representation of this phenomenon. The separation bubble grows with increasing angle of attack until the flow over the entire airfoil is separated. For airfoils with a rather small leading edge radius this type of stall is a very real problem, and in practice more often than not it happens that the separation bubble leads to a rather abrupt form of stall, also referred to as *bubble bursting*<sup>7</sup>. Crabtree designed a criterion to assess whether bubble bursting would occur or not [26]:

$$\left( \frac{u_{e,Reattachment}}{u_{e,Separation}} \right)^2 \leq 0.65 \quad (2.6)$$

The impact of the different stall modes on the behaviour of the airfoil is summarized in figure 2.18.

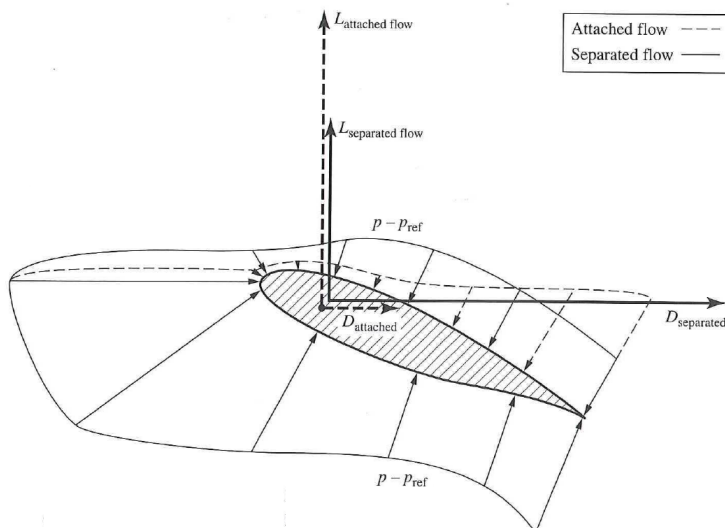


Figure 2.17: Qualitative comparison of the pressure around an airfoil for a separated (solid) and non-separated case (dashed). [11]

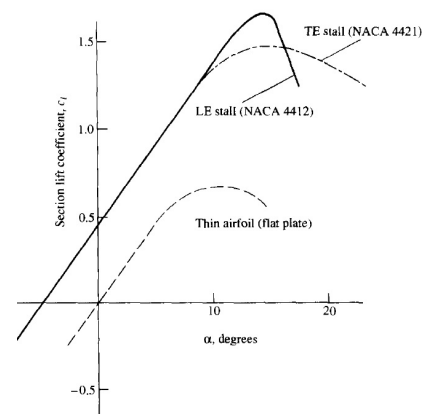


Figure 2.18: Difference between LE, TE and thin airfoil stall. [11]

<sup>7</sup>A little preview: the ‘bubble bursting’ effect may be strengthened by boundary layer suction, see section 2.2.3.

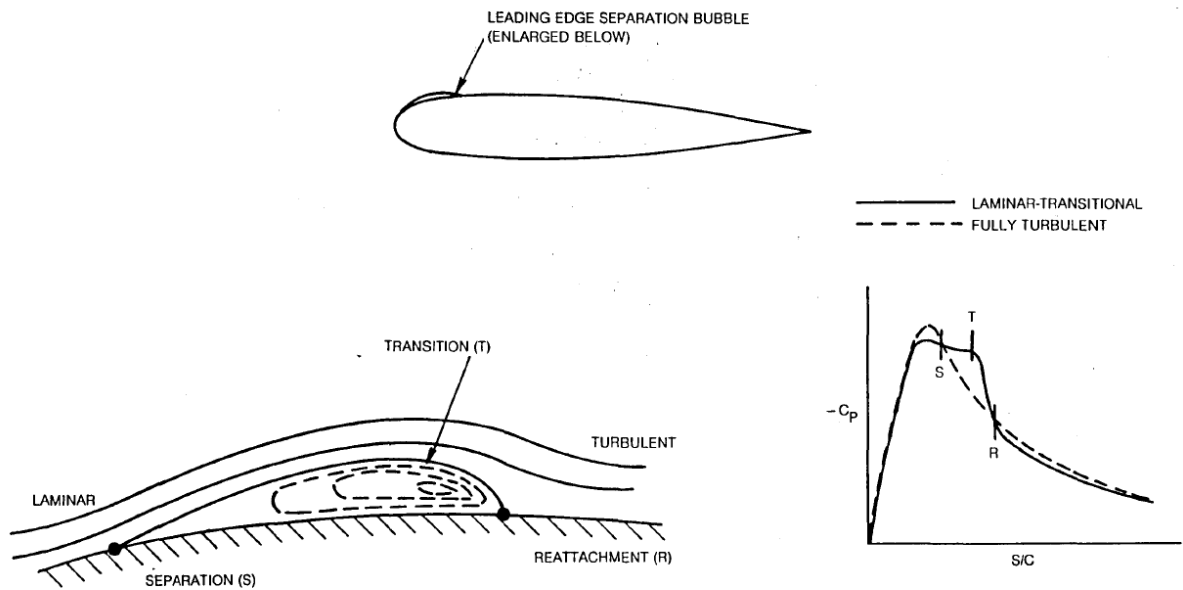


Figure 2.19: Schematic of a laminar separation bubble and the accompanying change in pressure distribution. [27]

For a well designed multi-element airfoil the stall is usually gradual, like the trailing edge stall in figure 2.18. Consider a typical configuration with a main element, a flap and a slat. The main element obviously carries the highest wing loading, and the loads on the slat and main element increase with increasing angle of attack. The load on the flap however typically decreases. At the point of stall, the flow over the main element is typically separated, while the load on the flap is still lowering and — provided gap and overhang are well designed — the flow is not separated there [28, 29].

#### MARGINAL AND MASSIVE SEPARATION

Refer again to figure 2.9. As explained in section 2.1.4 a singularity appears that is related to the onset of separation where the relation between  $u_e$  and  $\delta$  reaches a minimum (this point is often referred to as the Goldstein singularity). The Prandtl boundary layer theory becomes invalid at this point, it is thus a 'limiting point' indicating the appearance of flow separation. The term *marginal separation* is used to describe the solutions close to this limiting point. *Massive separation* on the other hand refers to a flow where all hierarchy between the outer flow and the boundary layer is lost [20].

#### 2.1.5. WAKE

Behind any body in a flow a region of retarded flow exists: the wake. This is no different for multi-element airfoil systems. When the boundary layers of upstream elements in a multi-element airfoil are 'dumped' at the trailing edge a wake develops. The wake is a region where a significant momentum deficit with respect to the surrounding flow field exists and where viscous effects are important (it is also referred to as 'low-energy' air). In contrast to the difference in velocity in the wake, the direction of the local flowfield in the wake cores does not differ from the flow outside of it [30]. As explained in section 2.1.3 it is already explained that the wake is more forgiving with respect to adverse pressure gradients and that it can be used to achieve faster pressure recovery without flow separation. However, despite this fact adverse pressure gradients always have the effect of increasing the momentum deficit in a wake. The viscous effects counter this by smoothing out the velocity defects. Based on this fact a criterion was developed by Gartshore to determine whether a wake was growing or decaying:

$$\frac{1}{1-C_p} \frac{dC_p}{dx} > \frac{0.007}{\delta^*} \quad (2.7)$$

In equation (2.7) the variable  $\delta^*$  is the local displacement thickness of the wake. If the factor  $\frac{1}{1-C_p} \frac{dC_p}{dx}$  is less than  $\frac{0.007}{\delta^*}$  the viscous effects dominate and the wake decays. However, if the right-hand side of (2.7)

is larger than  $\frac{0.007}{\delta^*}$  the adverse pressure gradient is too large and the wake grows. This can lead to the wake merging with the boundary layer element on a downstream element which must be avoided.

#### WAKE CORE

Pomeroy et al. [30] describe a method to numerically locate the position of the wake core based on the velocity gradient of the flow normal to the surface. At a constant chord wise station the velocity gradient normal to the surface  $\frac{\partial v}{\partial y}$  must be calculated and local maximum and minimum values of this velocity gradient define the edges of the wake. This method works for both confluent and non-confluent boundary layers. In the same paper it is also reported that finding the edges of the wake cannot be done by using the location of the streamlines, since they do not follow the edges of the wake.

#### CONFLUENT BOUNDARY LAYERS

In a well designed multi-element airfoil, the wake of upstream elements does not merge prematurely with other boundary layers [16]. This can be achieved by varying the gap and overhang appropriately, which explains the importance of a good combination of ‘gap’ and ‘overhang’ in a good multi-element airfoil design. However, it is not uncommon that it happens that the wake and a boundary layer merge nevertheless, leading to a phenomenon called *confluent boundary layers*.

Confluent boundary layers are a complex phenomenon with strong inviscid-viscid coupling. They can be classified based on the stage of development (figure 2.20) and their structure normal to the wall (figure 2.21), due to Agoropoulos and Squire [31] and Johnston and Horton respectively. The complexity of the confluent boundary layer is evidenced by the findings of several authors:

- Bario et al. report that the laws of the wall and wake can describe the confluent boundary layer — which is good news of course, but in their comparison of experiment with computation the point of zero shear stress did not match the point of zero velocity gradient [32].
- Agoropoulos and Squire report that in the merging stage (figure 2.20b)) areas exist where the shear stress is of opposite sign to the velocity gradient [31].
- Johnston and Horton report that a small region exists in the vicinity of the wall and the inner half wake layer where the Reynolds shear stress  $-u'v'$  has an opposite sign of the velocity gradient  $\frac{\partial u}{\partial y}$  [33].

The above means that not everywhere the Boussinesq hypothesis is valid (which models eddy viscosity by relating Reynolds shear stress to the normal velocity gradient). This is an important fact since a lot of turbulence models rest upon this hypothesis. It is hinted by some researchers that there is also a contribution of momentum transport over larger distances. This transport is due to larger turbulent structures (eddies) which can conserve their form while entering the inner half layer. In that way turbulence generated in the outer wake is transported to the inner layer and as a result locally the shear stress can be positive while the velocity gradient is negative [29, 32].

Based on the findings of Johnston and Horton, Ying et al. also stress the importance of coordinate system: usually the (turbulent) properties of a boundary layer are calculated normal to the underlying surface. However, the wake of upstream elements may locally not be aligned with the underlying surface, resulting in significant errors when calculating these properties. Therefore it is better to align the coordinate system wherein the turbulent properties are calculated with the local shear layer or streamlines.

#### WAKE BURSTING

As was already briefly mentioned in section 2.1.4, flow can also ‘separate’ without being in contact with a wall, sometimes referred to as ‘off-the-surface flow separation’. This is a little bit a misleading term to put it because in a literal sense no separation can take place of course. What is happening here is that a region of flow reversal appears away from the surface. This region of flow reversal is the result of the wake of an upstream element not being able to overcome the adverse pressure gradient of the underlying element. Although there is some discussion about this, this phenomenon can limit lift and effectively cause the airfoil system to stall, even without separated flow over any surface [29, 34].

By studying the turbulent kinetic energy, Reynolds stresses and a turbulent kinetic energy production term Pomeroy et al. found that the origin of the turbulence in the wake regions was located at the shear layers between the wake cores, while turbulence production is virtually absent in the wake cores themselves [30].

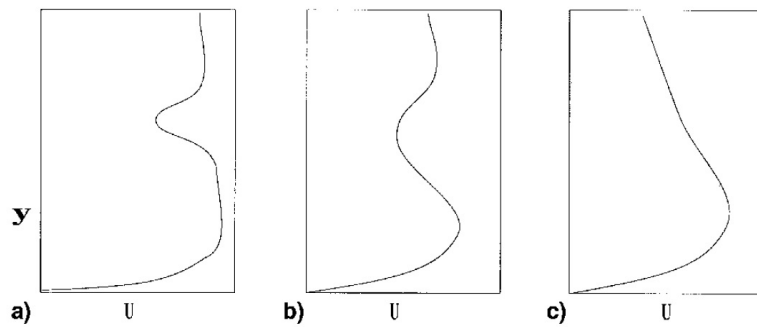


Figure 2.20: Three regions of wake and BL interaction: unmerged (a), merging (b) and merged (c). [31]

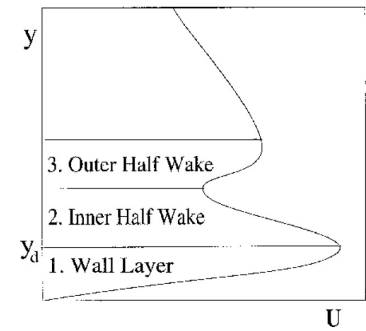


Figure 2.21: Subdivision of the confluent BL. [33]

## 2.2. BOUNDARY LAYER SUCTION

Boundary layer suction is often used for two quite different goals:

- Preventing the transition from laminar to turbulent flow with the goal of minimizing friction drag<sup>8</sup>.
- Preventing separation with the accompanying loss of lift (for an example see e.g. figure 2.23).

Boundary layer suction fits within the very diverse area of flow control, more specifically *active* flow control. The goals of active flow control are nearly endless — the two goals usually aimed for with suction mentioned above are just the tip of the iceberg. The different aspects of flow control and how they relate to each other are summarized in figure 2.22, taken from the book *Flow Control* by M. Gad-El-Hak, one of the most notable researchers in this particular field [35]. Within the context of this thesis, the focus of the boundary layer suction chapter will be on *turbulent* boundary layers. The transition of the boundary layer from laminar to turbulent flow is assumed to have already happened. Referring again to the opening sentence, the focus will thus be on the use of boundary layer suction to prevent separation — with the goal of maximizing the maximum lift coefficient.

### 2.2.1. HISTORICAL BACKGROUND AND FLYING EXAMPLES

The concept of boundary layer suction is as old as the concept of the boundary layer itself. Prandtl actually used a suction slot to remove the boundary layer from the flow around a cylinder, resulting in attached flow up to the rear of the cylinder hence proving the existence of the boundary layer [25] (see also figure 2.15 for the aforementioned experiment).

Flying examples that demonstrate the capabilities of boundary layer suction are currently limited to projects aimed at extending the laminar flow over the wing. One of the more notable examples of using boundary layers suction to promote laminar flow involves the F-16XL (an experimental version of the F-16 with a cranked delta wing, figure 2.25a). One of the wings of an F-16XL was fitted with a so called ‘glove’ over its wing made from titanium to serve as a suction sheet. The glove had laser drilled holes with a diameter of 0.0635 mm with a spacing between them ranging from 0.25–1.4 mm. The goal was to extend the laminar flow over the wing to 50–60% of the chord by sucking away the turbulent airflow, but at its optimum was only achieved up to 42% of the chord [37, 38]. Also experiments involving boundary layer suction on airliners such as the Boeing 757 and Airbus A320 have been performed [39].

More within the context of this project are examples of aircraft that use active boundary layer control to increase high lift performance (instead of delaying transition), even several examples exist of BLS used in conjunction with multi-element airfoils. A german experiment in 1940 showed that BLS can prevent separation over a flap (figure 2.24). Around the same time another experimental aircraft was built in the united states, derived from the Stinson-Vultee L1 (figure 2.25c). The BLS system performed well and a maximum lift coefficient of 3.6 was reached, thanks to the fact that with the boundary layer suction the two-section flap could be deflected to 82°. However, the BLS system itself was bulky and complicated and at the time the gain was practically cancelled by the increased weight of the special wing, engine, and ducting [40].

<sup>8</sup>It should be said however that this can also be very effective to *increase lift* as pointed out in e.g. [16].

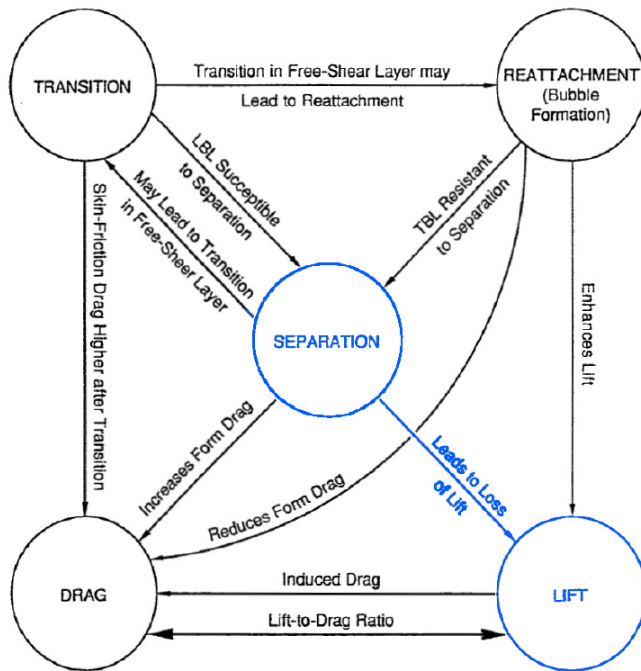


Figure 2.22: Flow control diagram. In the context of the research project the focus is on preventing separation to increase maximum lift. [35]

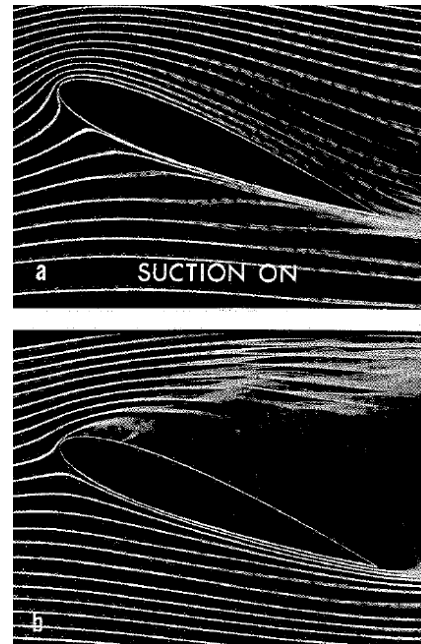


Figure 2.23: Comparison of flow over an airfoil at high angle of attack with (a) and without (b) suction. [36]

After these first attempts at preventing separation with boundary layer suction (be it on single or multi-element airfoils) a change of direction took place and blowing gained much more attention to prevent separation. Also most of the more recent research is directed in this direction, see also section 2.2.3). Examples are the Shin Meiwa PS-1/US-1A and the Blackburn Buccaneer. The Shin-Meiwa has a blowing system to improve STOL performance provided by a separate engine in the fuselage [41]. The Buccaneer 2.25b had a blowing system along the full span of the trailing edge of the main wing which bled high pressure air from the engine. By blowing elements downstream a lift increase of 50% was obtained when compared to contemporary aircraft. The use of blowing allowed the use of slats to be entirely discarded in the design [42].

### 2.2.2.2. SUCTION TYPE

Boundary layer suction can be divided up into two different kinds of suction: slot suction and continuous suction. The difference between both methods is not entirely trivial since they differ distinctly in the resulting flow field and the way separation is eventually prevented.

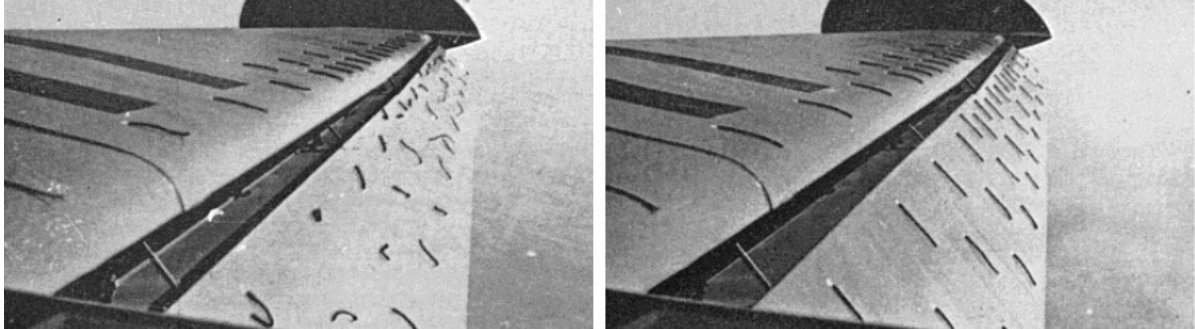
With *slot suction* a part (or all) of the boundary layer is sucked away through a small 'slot', illustrated for a cylinder in figure 2.15 and a diffuser in figure 2.16. Slit suction actually acts as a 'sink' on the outer flow (so not a direct effect on the boundary layer, other than it being sucked away), causing it to speed up in front of the slot, but also being slowed down behind it. The acceleration of the flow in front of the slot prevents separation. Behind the slot the boundary layer can start again with a drastically decreased thickness (in the case of slot suction usually the entire boundary layer is sucked away so it starts of again from zero thickness) which also prevents separation despite the fact that the outer flow is slowed down. The thinner boundary outweighs this by being able to withstand greater adverse pressure gradients. [20]

With *continuous suction* the wall is considered permeable, so the vertical velocity at the wall is not zero. Contrary to slot suction it has a direct effect on the boundary layer: the shape of the velocity profile in the boundary layer by is made more convex (especially near the wall) thus preventing separation. This can be illustrated by looking at the boundary layer equations (2.1). By taking the BL-equation for  $x$ -momentum (equation 2.1b) at the wall ( $y = 0$ ) but with boundary layer suction ( $v_0 \neq 0$ ) equation 2.8 is obtained:

$$\mu \frac{\partial^2 u}{\partial y^2} = \frac{1}{\rho} \frac{\partial p}{\partial x} + v_0 \frac{\partial u}{\partial y} \quad (2.8)$$



(a) Airplane fitted with BLS.

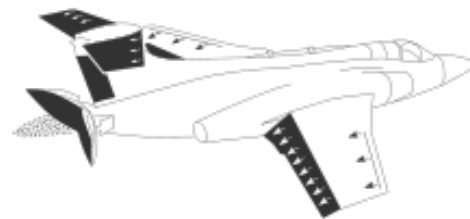


(b) Effect with (right) and without (left) suction on separation over the flap.

Figure 2.24: 1940 German test of flapped wing with BLS. [43]



(a) F-16XL fitted with glove for BLS. [44]



(b) Blackburn Buccaneer. [42]



(c) Modified Stinson-Vultee L-1 'Humpback'. The hump on the fuselage houses the engine that drives the suction. [40]

Figure 2.25: Flying examples of aircraft with active boundary layer control.

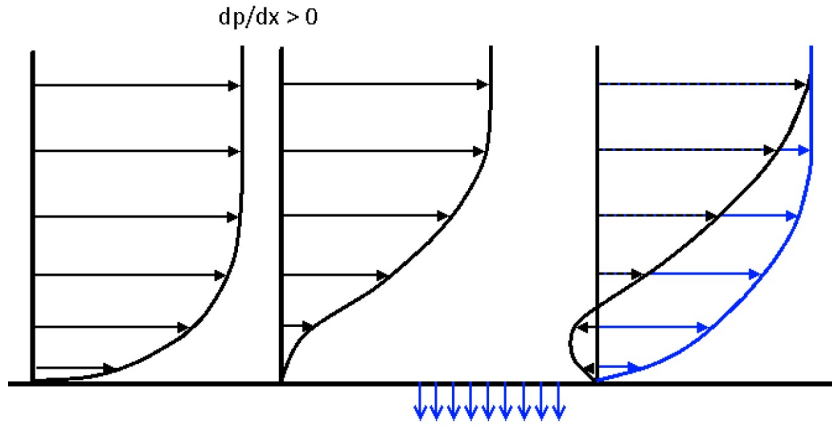


Figure 2.26: Effect of boundary layer suction on the velocity profile in the boundary layer. [45]

The right hand side of equation 2.8 should be negative to have a convex velocity profile up to the wall (recall that by definition the flow is separated if the right hand side is zero, see also section 2.1.4). In the case of an adverse pressure gradient the term  $\frac{1}{\rho} \frac{\partial p}{\partial x}$  becomes positive. If  $\nu_0$  is smaller than zero, i.e. as is the case for boundary layer suction, it relieves the destabilizing effect of the adverse pressure gradient and therefore delays separation. The effect of boundary layer suction is qualitatively outlined in figure 2.26.

The effect of boundary layer suction can also be linked to the shape factor, which is convenient when formulating separation criteria and when modelling boundary layers (see also section 2.1.4). If the effect of compressibility is neglected ( $\rho = cte \approx 1$ ) BLS has different effects on the shape parameter  $H$  for continuous and slot suction [3]:

- For *continuous suction* the displacement ( $\delta^*$ ) and momentum thickness ( $\theta$ ) decrease and the shape parameter  $H$  approaches an asymptotic value.
- For *slot suction* the displacement ( $\delta^*$ ) and momentum thickness ( $\theta$ ) evidently also decrease but the shape factor approaches the minimum value 1.

### MODELING BLS

This section contains some general considerations that are important to keep in mind when modelling BLS. A thorough discussion of the changes to integral boundary relations and closure relations is not given here but in chapter 3 (which discusses the changes to MSES to simulate BLS) to avoid unnecessary repetition.

It is more difficult to model discontinuous suction, since while approaching the minimal value of 1 for the shape factor,  $\delta^*$  and  $\theta$  tend to go to zero. If one or the other decreases too fast instabilities occur because the shape factor reaches zero ( $\delta^* \rightarrow 0$ ) or explodes ( $\theta \rightarrow 0$ ). It is vital that the shape factor  $H$  approaches 1 while  $\delta^*$  and  $\theta$  both go to 0 due to suction.

Another phenomenon that complicates the modeling of slot suction is the appearance of a stagnation point. Figure 2.27 clarifies this: as explained earlier the suction slot acts as a sink on the flow, which can be modeled by a uniform flow. The superposition of them creates a stagnation point. Because slot suction is typically relatively strong, this leads to local flow reversal and separation bubbles. This also affects the BL behaviour. A good suction slot geometry is aimed at minimizing these effects, e.g. by ‘tilting’ the suction slot in such a way that it is more aligned with the flow. This will cause the stagnation point to move further inside the slot, away from the boundary layer.

Also a more general problem arises when modelling BLS. Looking at figure 2.26 it can be (qualitatively) seen that suction ‘pulls’ the velocity profile down to the surface, i.e.  $\frac{\partial u}{\partial y}$  increases. It is not difficult to imagine that by increasing suction also this effect becomes stronger and stronger. Recall that  $C_f = f\left(\frac{\partial u}{\partial y}\right)$  and as a result suction will increase the skin friction, possibly to extreme values. In the limit the skin friction will become infinitely large for infinitely strong suction, and the shape parameter  $H_k$  will reach the limit of 1. In practice this is impossible and even non-physical; and also modelling this leads to insurmountable problems.

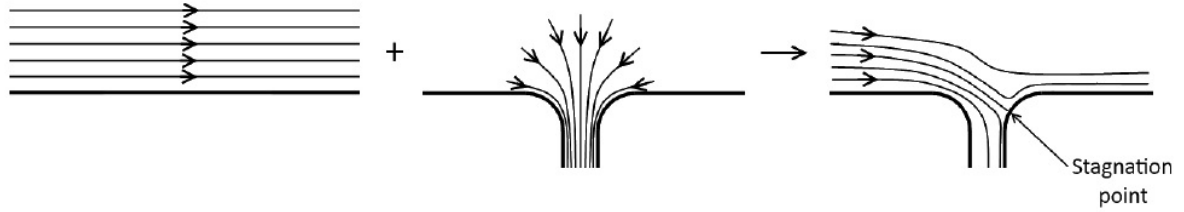


Figure 2.27: Slot suction represented as the superposition of a uniform flow and a sink. [45]

### 2.2.3. BOUNDARY LAYER SUCTION ON MULTI-ELEMENT AIRFOILS

The flow field around a multi-element airfoil is very complex, including e.g. recirculation zones, wakes and the associated confluent boundary layers [29] and wake bursting [30]. This complex flow field around multi-element airfoils leaves a lot of ‘opportunities’ for active boundary layer control to improve the airfoil performance. Although more recent research towards active boundary layer control and high lift systems has been primarily directed at periodic excitation of the boundary layer (e.g. [8, 10, 46, 47]) the focus in this literature review will be on (constant) boundary layer suction since this is the subject of the encompassing project.

Boundary layer suction on upstream elements in a multi-element airfoil reduce in the first place the thickness of the boundary layer, but the effectiveness of the suction extends beyond that: also the thickness of the wake is reduced and as such it is more able to withstand an adverse pressure gradient. It may even cause the wake to decay instead of grow, thus preventing undesirable effects as confluent boundary layers and wake bursting which lead to a rapid loss of lift. This was first recognized by Gartshore [17] and has been confirmed by later experiments.

Combining multi-element airfoils with (slot) suction to improve high-lift performance received considerable attention quite early; not entirely coincidental together with the appearance of the need for high-lift solutions for high-speed airfoils. An early investigation by Quinn in 1947 (figures 2.28–2.30 for reference) showed that slot suction over the main surface could increase, in general, maximum lift and decrease section drag. At a Reynolds number of  $3 \cdot 10^6$  the maximum lift increased with  $\Delta C_{l_{max}} = 0.28$  for a simple airfoil and increasing up to  $\Delta C_{l_{max}} = 0.56$  for a slat-airfoil-flap combination (suction location  $0.4c$ , suction level  $\frac{Q}{u_{\infty}bc} = 0.03$ ).

More recently the combination of high-lift airfoil configurations and active boundary layer control has seen renewed interest [49–52]. Shmilovich and Yadlin find that removing a part of the boundary layer at the slat (i.e. the most upstream element) creates a thinner wake that helps to improve the  $C_{l_{max}}$  of a three-element airfoil from 4.9 (baseline) to 6.25, although this also includes periodic excitation at two stations on the flap (data without this is unfortunately not available) [51]. The results of this study can be seen as lift curves in figure 2.31. It is interesting to keep in mind that this secondary effect of boundary layer removal (i.e. obtaining a thinner wake) can also be achieved by slot suction, which is a simpler suction mechanism when compared to continuous suction.

In a study involving constant boundary layer suction on a multi-element airfoil system by Khodadoust and Shmilovich [52] some interesting results can be found which showcase how boundary layer suction can be applied in other ways to increase the multi-element airfoil performance. In contrast to applying boundary layer suction at the trailing edge of the most upstream element, air is sucked away near the leading edge of the flap from a slot. Two different suction levels are compared:  $C_{\mu} = 0.0002$  and  $C_{\mu} = 0.0009$ . Here  $C_{\mu}$  is a dimensionless suction parameter, for which most researchers use the same convention, given in equation (2.9) (note that  $C_{\mu}$  as given in equation (2.9) is a version of  $C_q$  integrated over an area with constant suction. Some authors however use another definition, so  $C_{\mu}$  is given by equation (2.9) unless otherwise stated.

$$C_{\mu} = \frac{h}{c} \frac{\rho_w}{\rho_{\infty}} \left( \frac{v_w}{u_{\infty}} \right) \quad (2.9)$$

The maximum lift coefficient is increased from 3.45 to approximately 3.8 for both suction levels, but rather surprisingly a higher suction level does not give a noticeably better  $C_{l_{max}}$ . This may indicate that for slot suction increasing the suction above a certain level does not have significant effects on the flow, possibly around the point where the complete boundary layer is sucked away. Also the linear part of the lift curve is shifted upwards by  $\Delta C_l = 0.6$  and  $\Delta C_l = 0.8$  respectively so in the presented case increased suction (i.e. above the threshold level where  $C_{l_{max}}$  is not increased any further), while it has no effect on  $C_{l_{max}}$ , does have

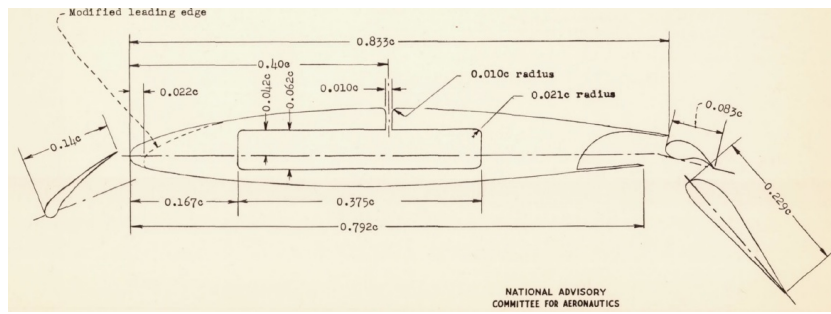


Figure 2.28: Geometry of investigation by Quinn: NACA 641A212 airfoil section with boundary-layer suction slot, leading-edge slat, and double slotted flap. [48]

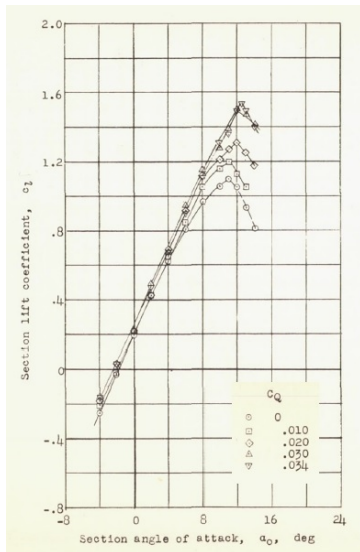


Figure 2.29: Lift characteristics for suction experiment after [48]

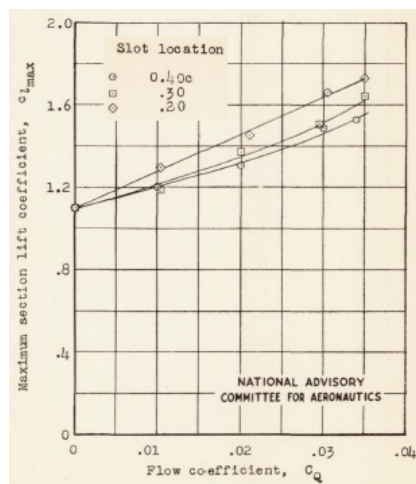


Figure 2.30: Variation of maximum section lift coefficient after [48]

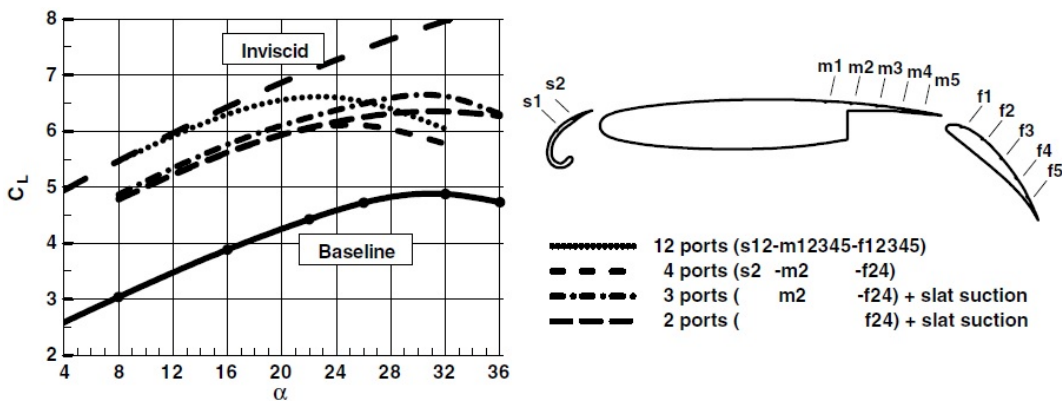


Figure 2.31: Lift curves for a multi-element airfoil with slat suction. [51]

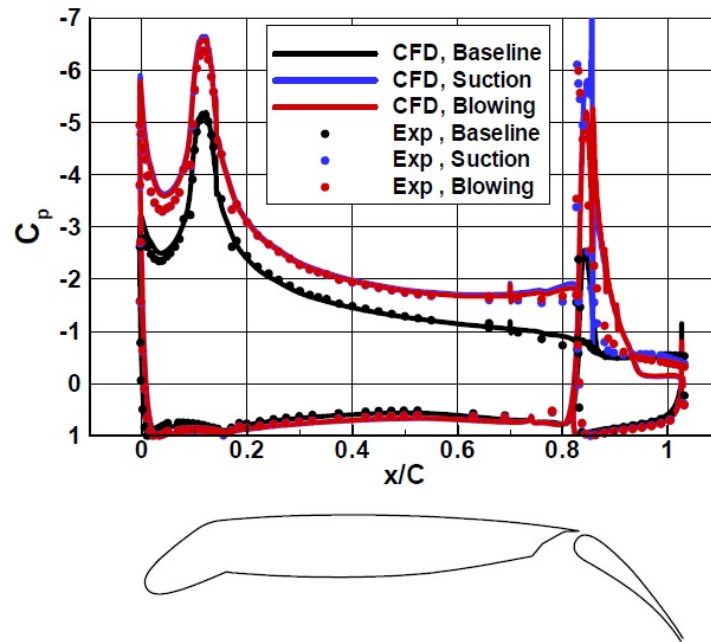


Figure 2.32: Pressure distribution over multi-element airfoil with blowing and suction. [52]  
 $\alpha = 8^\circ$ ,  $\Delta C_{l_{max}} = 0.79$  (for the active boundary layer control cases),  $Re = 9 \cdot 10^6$

an effect on the linear part of the lift curve. Also the stall becomes much more gradual when compared to the baseline case without suction. Figure 2.34 shows the lift curve for different blowing and suction levels compared to the baseline case without suction.

The higher overall lift performance of the airfoil combination due to suction and blowing can — evidently — be traced back to a changed pressure distribution, shown in figure 2.32. This figure shows how by applying suction or blowing at the trailing edge of the flap element the entire flow field is altered. By increasing circulation on the flap element also the circulation over the main element is increased by means of the ‘circulation effect’ (see section 2.1.3). By applying suction on the flap leading edge however a large pressure peak arises, which for the baseline is rather moderate due to the ‘slat effect’ (section 2.1.3). Note how the pressure distribution in figure 2.32 also strongly suggests that the dumping velocity at the trailing edge of the main element is significantly increased by both suction and blowing.

The limited increase in performance for increasing suction above a certain value is confirmed by charting the increase in  $C_{l_{max}}$  against the suction (and blowing) levels (see figure 2.33): from the case with zero suction (baseline) the  $\Delta C_{l_{max}}$  rises very sharply for minimal amounts of suction to top off at a value of  $\Delta C_{l_{max}} = 0.8$  for  $C_q = 0.001$ . On the other side of the spectrum — i.e. for blowing — the increase in  $\Delta C_{l_{max}}$  is much more gradual, which means that much higher levels of blowing are required to achieve similar performance to suction ( $\Delta C_{l_{max}} = 0.8$  for  $C_q = 0.0045$ ); but the increase in performance does not top off for a certain blowing level.

Figure 2.35 shows the (spectacular) change in the flow field between the cases with and without active flow control. For the cases with suction the authors report a complete elimination of flow reversal despite the large flap deflection as can be seen in the figure as well. Figure 2.35 also shows the flow near the orifice for suction/blowing, which shows the presence of a separation bubble for baseline and suction case inside the orifice.

The same study by Khodadoust and Shmilovich also stresses the sensitivity of the viscous layers to the Reynolds numbers: below a Reynolds number of  $3 \cdot 10^6$  the thickening of the boundary layer and wake of the main element becomes much more severe resulting in a loss of circulation ultimately leading to a (quite spectacular) drop in  $C_{l_{max}}$  from 3.4 for  $Re = 6 \cdot 10^6$  to 2.41 for  $Re = 1.6 \cdot 10^6$ . Related to the loss of circulation over the main airfoil is the loss of downwash on the flap element, causing the flow to separate earlier which is also a cause for the drop in maximum lift.

Research towards delaying separation with boundary layer suction over multi-element airfoils has also

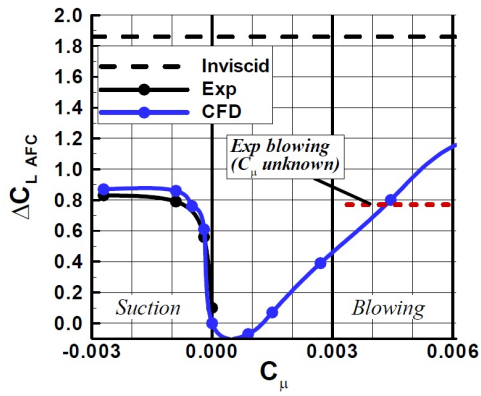


Figure 2.33: Variation of  $\Delta C_{l_{max}}$  with  $C_{\mu}$ . Negative values indicate suction. [52]  
 $\alpha = 8^{\circ}$

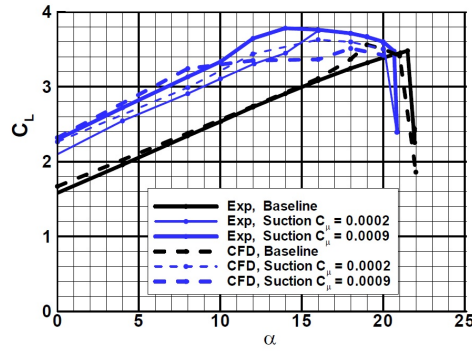


Figure 2.34: Lift curve for different suction and blowing levels. [52]

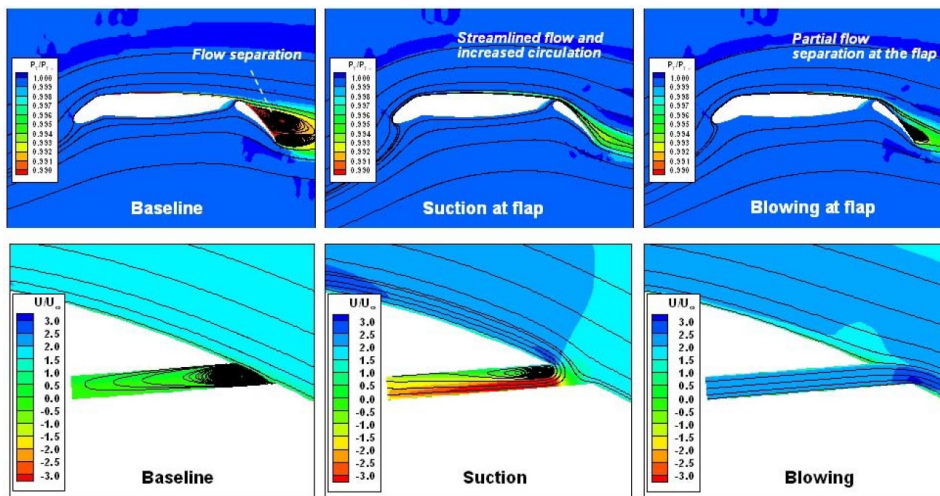


Figure 2.35: Flow field for a multi-element airfoil with and without suction and blowing. From Khodadoust et al. [52]  
 $\alpha = 8^{\circ}$ ,  $\Delta C_{l_{max}} = 0.79$

been the subject of extensive study at the faculty of Aerospace Engineering at the TU Delft. Separation delay by slot- and continuous suction was investigated by Wijnen on the NLF-MOD22(B) airfoil [53]. The influence of boundary layer suction was studied with the help of numerical simulations in Fluent. The main airfoil angle of attack and also the flap deflection were both kept fixed for the analysis at  $\alpha = 0^{\circ}$  and  $\delta_f = 50^{\circ}$  respectively. Instead, the benefits of suction were studied by observing the shift in the separation location with varying suction levels. Three different cases were considered: two slot suction locations located on the flap at  $x/c = 0.852$  and  $0.896$  and one porous suction surface between the first slot and  $x/c = 1.05$ .

Table 2.1 summarizes the results of this study. For the front slot the improvement is only marginal, with  $\Delta C_{l_{max}} = 0.1$  for  $C_{\mu} = 0.01$  and only marginally for higher  $C_{\mu}$ . The aft slot provides a better improvement:  $\Delta C_{l_{max}} = 0.4$  for  $C_{\mu} = 0.01$ , increasing marginally for higher suction levels. The continuous suction shows the best improvement of  $C_{l_{max}}$ :  $\Delta C_{l_{max}} = 0.82$  for  $C_{\mu} = 0.03$ ; for  $C_{\mu} = 0.01$  it performs similar to the aft slot suction. In all cases the relatively high suction requirements stand out (compared to the results obtained from other literature discussed in previous sections); for example, increasing the angle of attack to  $8^{\circ}$  requires a suction level of  $C_{\mu} = 0.1175$  to obtain optimal suction (the increase in performance is unclear). It should be said however that the fact that the results from Wijnen are so different from other references and taking into account the quality of the simulations at least hints at the fact that these results may not be as reliable as others.

Also Terry analysed two multi-element airfoils with boundary layer suction: the Dallara F3 and Toyota F1 front wings, both examples from the automotive racing field [39]. The research was primarily directed at studying the effect of continuous suction over the main element (in contrast to Wijnen who studied suction

Table 2.1: Optimal suction parameters obtained for different suction cases by [53].

	$C_l$	Separation location [ $x/c$ ]
Baseline (no suction)	1.67	0.926
Front slot, $C_q = 0.065$	1.85	0.944
Aft slot, $C_q = 0.055$	2.26	0.972
Continuous, $C_q = 0.0163$	2.29	1.005
Continuous, $C_q = 0.0453$	2.51	1.053
Continuous, $C_q = 0.1175$	2.54	1.021

Table 2.2: Results of suction on automotive multi-element airfoils [39].

	$C_{l_{max}}$	$\alpha_{C_{l_{max}}}$
Dallara F3, baseline	4.174	21°
Dallara F3, suction	4.534	25°
Toyota F1, baseline	5.744	24.9
Toyota F1, suction	6.087	25.2

on the flap). The results are summarized in table 2.2. For the F3 front wing he finds a  $\Delta C_{l_{max}} = 0.36$  for continuous suction located at the aft of the main airfoil ( $x/c = 0.5-0.9$  and  $v_w \approx 0.0044$ ). An interesting side note is made by Terry: “At increasing angle of attack there is a loss of positive interference between the two elements of the airfoil. Due to the negative effect of the inviscid interference between the two elements and due to the viscous displacement effect of the first element’s wake on the pressure distribution of the second element, the second element loses lift and as a consequence the positive influence on the circulation of the first element decreases.” [39]. This could be avoided by applying boundary layer suction to minimize the thickness of the wake. Even more so, at increasing angle of attack Terry reports that the wake becomes thinner with BLS. For the F1 front wing  $\Delta C_{l_{max}} = 0.304$  was found, despite the occurrence of bubble bursting at the leading edge which limits the benefits of boundary layer suction.

# 3

## BOUNDARY LAYER SUCTION FOR MSES

This chapter provides an overview and explanation of the changes made to MSES, an inviscid-viscid interaction aerodynamic solver developed by Mark Drela at the MIT Department of Aeronautics and Astronautics. The original MSES code is presented in [54] and thoroughly discussed in [55]. In the context of the project this code was modified to include modelling the effects boundary layer suction. Earlier efforts to achieve this were already undertaken by Ali Merchant and also at the faculty of Aerospace engineering at the TU Delft, but these codes were not available [3, 39, 56].

This chapter will focus on the boundary layer formulation and the inviscid-viscid interaction coupling, since these are obviously the affected parts of the physical domain and also in the code itself. The first section provides a short discussion of the overall MSES code which provides the necessary basis for a discussion of the modifications to the aforementioned boundary layer formulation and inviscid-viscid interaction coupling model, which follows in the subsequent sections. It is not the goal of this chapter to give a thorough discussion of the MSES code nor the complete theory behind it, for which the reader is referred to [55] and [57].

### 3.1. MSES IN SHORT

MSES is an inviscid-viscid interaction aerodynamic solver which is able to solve aerodynamic flows around bodies which are 'slender' enough (i.e., no blunt bodies) for subsonic and even transonic flows and for high to relatively low Reynolds numbers. It is able to simulate flows around multi-element geometries, and

- The *inviscid domain* is solved by the Euler equations in conservative form:

$$\text{Continuity: } \nabla \cdot \rho \mathbf{u} = 0 \quad (3.1a)$$

$$\text{Momentum: } \nabla \cdot (\rho \mathbf{u} \mathbf{u}^T) + \nabla p = 0 \quad (3.1b)$$

$$\text{Energy: } \nabla \cdot (\mathbf{u} (E + p)) = 0 \quad (3.1c)$$

- A solution for the *viscous domain* is obtained by solving three ordinary differential equations:

von Kármán momentum integral equation:

$$\frac{C_f}{2} = (H + 2 - M_e^2) \frac{\theta}{u_e} \frac{du_e}{d\xi} + \frac{d\theta}{d\xi} \quad (3.2a)$$

Kinetic energy shape parameter equation:

$$\theta \frac{dH^*}{d\xi} + (H^{**} + H^*(1 - H)) \frac{\theta}{u_e} \frac{du_e}{d\xi} = C_{\mathcal{D}} - H^* \frac{C_f}{2} \quad (3.2b)$$

Shear lag equation:

$$\frac{\delta}{C_\tau} \frac{dC_\tau}{d\xi} = 4.2 \left( \sqrt{C_{\tau(\text{eq})}} - \sqrt{C_\tau} \right) + \left( \frac{2\delta}{u_e} \frac{du_e}{d\xi} \right)_{(\text{eq})} - \left( \frac{2\delta}{u_e} \frac{du_e}{d\xi} \right) \quad (3.2c)$$

The first two equations form the two-equation integral boundary layer formulation; the first one is the well-known *von Kármán momentum integral equation* and the second equation is derived from a combination of the energy equation and the momentum equation; its derivation is shown in [55]. The shear lag equation must account for upstream history effects in the turbulent boundary layer. Where the boundary layer is laminar it is replaced by another rate equation for the disturbance amplification ratio to predict transition, using an  $e^9$  based method. The integral boundary layer formulation must be closed with so-called closure relations, discussed in section 3.4.

The inviscid and viscous domain are coupled by the well-known coupling condition that the displacement of the inviscid streamlines is proportional to the mass defect due to the presence of the boundary layer; an assumption which is true for flows without massive separation. This mass defect equals  $\rho_e u_e \delta^*$  and when no wall transpiration is present the displacement of the inviscid domain normal to the wall is simply equal to the displacement thickness itself:

$$\Delta n = \delta^* \quad (3.3)$$

The viscous and inviscid equations are simultaneously solved in the overall system of equations (see also section 3.1.1), hence they are ‘fully coupled’. The discretized and linearized system of equations is solved using the Newton method.

### 3.1.1. NEWTON SYSTEM

After discretization and linearisation of the coupled, non-linear Euler equations (3.1) a linear system of equations is obtained, represented by  $F(\mathbf{U}) = \mathbf{0}$ , where  $\mathbf{U}$  is the vector with the unknown variables. This system can be solved iteratively with the Newton method ( $n$  indicates a certain iteration):

$$\begin{aligned} F(\mathbf{U}^{n+1}) &= F(\mathbf{U}^n + \delta\mathbf{U}^n) = 0 \\ \Leftrightarrow F(\mathbf{U}^n) + \left(\frac{\delta F}{\delta \mathbf{U}}\right)^n \delta\mathbf{U}^n &= 0 \end{aligned} \quad (3.4a)$$

The Newton system to be solved is given by:

$$\left(\frac{\delta F}{\delta \mathbf{U}}\right) \delta\mathbf{U} = -F(\mathbf{U}) \quad (3.4b)$$

Continuing further with (3.4a),  $\delta\mathbf{U}^n$  can be calculated with the *Jacobian*  $\left(\frac{\delta F}{\delta \mathbf{U}}\right)$  evaluated at the previous iteration level:

$$\delta\mathbf{U}^n = -\left(\left(\frac{\delta F}{\delta \mathbf{U}}\right)^{n-1}\right)^{-1} F(\mathbf{U})^n \quad (3.4c)$$

Followed by an update of the solution:

$$\mathbf{U}^{n+1} = \mathbf{U}^n + \delta\mathbf{U}^n \quad (3.4d)$$

The discretized and linearised Euler and boundary layer equations for every grid node form the system of equations  $F$  — supplemented by some global equations and variables for e.g. the Kutta condition. They are solved on a ‘streamline grid’: the grid nodes are located on streamlines dependent on the solution, so the grid nodes  $(i = 1 \rightarrow i_{\max}, j)$  and  $(i = 1 \rightarrow i_{\max}, j + 1)$  form a streamtube. Since there is no mass transfer between two streamtubes — i.e. the normal velocity to a streamline is zero — a fixed mass fraction can be assigned to each streamtube. This in turn allows to relate the position of the grid nodes to the flow velocity and this is exploited by MSES. By also constraining the movement of the grid nodes along the streamlines, the system of equations for the inviscid domain (3.1) can be rewritten as a function of only the grid movement normal to the streamlines  $\delta n$  and the density  $\delta\rho$ . To solve the viscous domain, the BL equations are added (3.2) to the system of equations  $F$ , which are rewritten to only depend on the additional variables  $\delta\sqrt{C_T}$ ,  $\delta\theta$  and  $\delta\delta^*$  which are added to the vector of unknowns  $\mathbf{U}$ . Upstream of any BL stations dummy equations are used, and downstream of an element the BL equations are used to solve for the wake, with — obviously — the skin friction forced to be zero. The system to be solved eventually consists of all these equations for each grid node, resulting in a very large but very sparse system since the ‘zone of influence’ of a certain grid point is limited. This allows a so-called ‘block-structure’, shown in 3.1, which is exploited by the solver that uses a Gaussian block elimination algorithm.

$$\begin{bmatrix}
 \bar{A}_1 & \bar{C}_1 & & & & & & & & & \bar{U}_1 \\
 \bar{B}_2 & \bar{A}_2 & \bar{C}_2 & & & & & & & & \bar{U}_2 \\
 \bar{Z}_3 & \bar{B}_3 & \bar{A}_3 & \bar{C}_3 & & & & & & & \bar{U}_3 \\
 & \cdot & \cdot & \cdot & & & & & & & \cdot \\
 & & \bar{Z}_i & \bar{B}_i & \bar{A}_i & \bar{C}_i & & & & & \bar{U}_i \\
 & & & \cdot & \cdot & \cdot & & & & & \cdot \\
 & & & & \bar{Z} & \bar{B} & \bar{A} & \bar{C} & & & \bar{U} \\
 & & & & & \bar{Z} & \bar{B} & \bar{A} & \bar{C} & & \bar{U} \\
 & & & & & & \bar{Z}_I & \bar{B}_I & \bar{A}_I & \bar{C}_I & \bar{U}_I \\
 \hline
 \bar{G}_1 & \bar{G}_2 & \bar{G}_3 & \cdot & \bar{G}_i & \cdot & \cdot & \cdot & \bar{G}_I & \cdot & \bar{G}_g
 \end{bmatrix}
 \times
 \begin{bmatrix}
 \bar{\delta}_1 \\
 \bar{\delta}_2 \\
 \bar{\delta}_3 \\
 \cdot \\
 \bar{\delta}_i \\
 \cdot \\
 \bar{\delta} \\
 \bar{\delta} \\
 \bar{\delta}_I \\
 \bar{\delta}_g
 \end{bmatrix}
 =
 \begin{bmatrix}
 \bar{R}_1 \\
 \bar{R}_2 \\
 \bar{R}_3 \\
 \cdot \\
 \bar{R}_i \\
 \cdot \\
 \bar{R} \\
 \bar{R} \\
 \bar{R}_I \\
 \bar{R}_g
 \end{bmatrix}$$

Figure 3.1: Newton system with block structure. Note that this is the system presented in equation (3.4b). The structure of the A-block is shown in detail in figure 3.2, the other blocks are similar wrt. their structure but can differ due to different boundary conditions. [55]

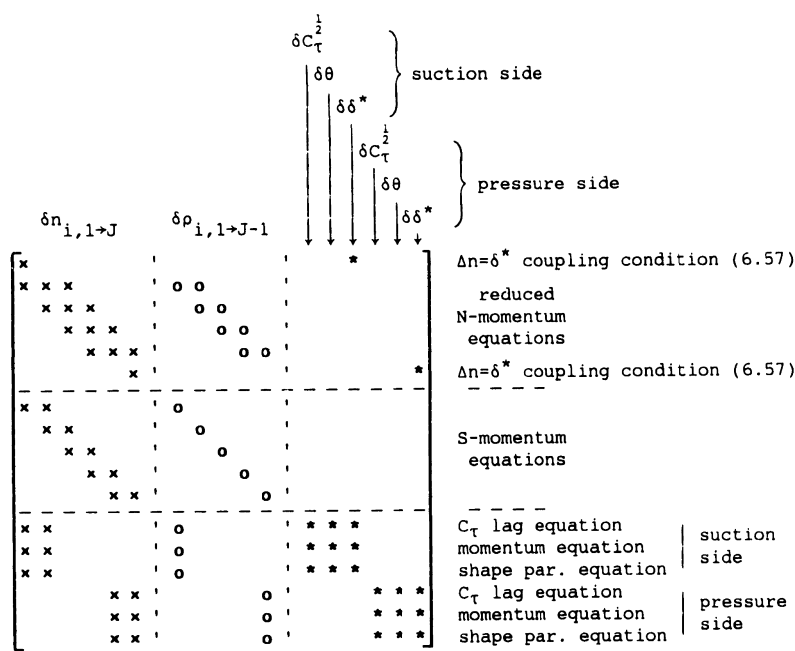


Figure 3.2: Structure of the A-block. The 'reduced N-' and 'S-momentum equations' solve the inviscid domain, the six equations below them represent the BL equations for the upper and lower side of the element respectively. 'x', 'o' and '\*' are used to denote  $\delta n$ ,  $\delta \rho$  and BL variable entries respectively. Also note the coupling condition, which is thanks to the choice of variables relatively easy implemented as a boundary condition. [55]

### 3.2. CODE STRUCTURE & SUMMARY OF MODIFICATIONS

The starting point for the modified MSES code was MSES 3.04 (2006). MSES and the related utilities are written in FORTRAN, a quite old yet still relevant programming language, particularly useful for solving mathematical and engineering problems. This section will give insight in the structure of the code, which basically consists of building the Newton system given by equation (3.4b) and solving it iteratively.

The derivatives that build up the Jacobian are found by applying the chain rule to every equation in the system all the way down to the primary ‘Newton variables’, i.e. every equation is differentiated with respect to its variables, then the variables themselves are differentiated with respect to a ‘higher’ set of variables and this all the way down to the primary variables  $n$ ,  $\rho$ ,  $\sqrt{C_\tau}$ ,  $\delta^*$  and  $\theta$ . The equations and the partial derivatives are evaluated by several different subroutines before building the Newton system with them. This process is probably most easily summarised using visual breakdown structure of the code, given in figure 3.4. Focus is given to the several steps required to set up the BL related equations and derivatives, and modified routines are highlighted. An overview of the actual function of several (sub)routines and the modifications to them is given in table 3.1.

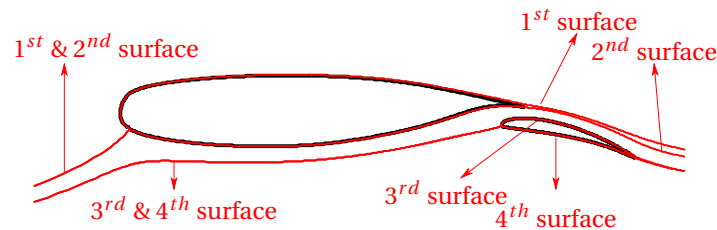


Figure 3.3: ‘BL surfaces’ in MSES.

All BL variables tied to a certain grid node are stored in an array which will be referred to as a ‘BL surface’. Geometrically, these surfaces can be viewed as the equivalent inviscid streamlines for every element (for the upper and lower surface). Figure 3.3 clarifies the concept. Also the suction distribution and — later on —  $\delta_{\text{suction}}^*$  is read and stored into such a surface, which greatly simplifies the access to the correct suction value whenever necessary.

Table 3.1: Short version of the changelog MSES to MatSESuction. Full version can be found in appendix B.

Modified routines			
Routine	P/S	Located in	Description & Changes
MSES	P	<code>mSES.f</code>	<p>Main program for initializing the solution from a previous solution state (stored in the <code>mDAT.xxx</code> file). Contains the main Newton loop for iteratively solving the Newton system (see section 3.1.1).</p> <ul style="list-style-type: none"> <li>• Additional argument is required for defining the suction mode (‘0’ for no suction (in which case the calculations follow the original MSES code) and ‘1’ for calculations taking into account suction).</li> <li>• Initialize suction distribution and read and set the suction distribution if required.</li> </ul>
SETBL	S	<code>setbl.f</code>	<p>Build the Jacobian and RHS of the Newton system for the BL grid nodes.</p> <ul style="list-style-type: none"> <li>• Before sweeping over all BL surfaces and grid nodes, VWSET is called to re-set the suction distribution to account for the movement of the stagnation point and BL grid nodes.</li> </ul>

Table 3.1: (continued)

SETBC	S	setbc.f	<p>Overwrite the Jacobian and RHS entries for grid nodes located at the boundary with appropriate value for either far field or wall conditions.</p> <ul style="list-style-type: none"> <li>• Add the displacement due to the mass defect due to suction to the RHS of the equations prescribing the coupling condition (see also 3.5).</li> </ul>
MRCHBL	S	io.f	<p>Marches every BL surface (also the wake) for every station <math>i</math> to establish the transition point based on the current solution and call for the solution of the BL variables.</p> <ul style="list-style-type: none"> <li>• Calculate the displacement due to thickness <math>\delta_{\text{suction}}^*</math> by calculating the integral in equation 3.12.</li> <li>• Added suction information to the argument list for every call to BLVAR and BLSYS.</li> </ul>
BLVAR	S	blvar.f	<p>Calculate non-kinematic BL variables for a certain BL grid node.</p> <ul style="list-style-type: none"> <li>• Added suction information to the argument list.</li> <li>• Calculate <math>C_\mu</math> and derivatives wrt. primary BL variables.</li> <li>• <math>H_k</math> lower limit is lowered further since with suction it should be able to approach 1 very closely.</li> <li>• Calculation of slip velocity <math>U_{\text{slip}}</math> reordered before calculation of <math>C_f</math> since the closure relation of <math>C_f</math> modified for suction requires <math>U_{\text{slip}}</math>.</li> <li>• Modified closure relation of <math>C_f</math> for suction cases, see also section 3.4. Also the derivatives of <math>C_f</math> are modified in accordance with the modified closure relation.</li> <li>• Modified closure relation for <math>C_\varnothing</math> as well as the derivatives with respect to the primary BL variables.</li> </ul>
BLSYS	S	blsys.f	<p>Sets up the integral momentum BL formulation equations and the shear lag equation (i.e. stores Jacobian entries and RHS in temporary local Newton system for later easy access). Also splits interval where transition occurs into a laminar and turbulent part (no additional grid nodes are created though).</p> <ul style="list-style-type: none"> <li>• Added interpolated value for <math>\nu_w</math> at the transition point (in case of a transition interval).</li> <li>• Added suction information to argument list for all BLVAR calls.</li> </ul>
BLDIF	S	bldif.f	<p>Calculates the Jacobian entries and RHS for the ODE's governing the BL for one interval (the integral momentum BL formulation and the shear lag equation).</p> <ul style="list-style-type: none"> <li>• Inclusion of <math>C_\mu</math> in the governing equations. At this level MSES already — very conveniently — included some sort of provision for future inclusion of <math>C_\mu</math>, which was used gracefully.</li> </ul>
CFTFUN	S	blfun.f	<p>Calculate turbulent <math>C_f</math> for a certain BL grid node.</p>

---

New routines

---

Table 3.1: (continued)

Routine	P/S	Located in	Description
JVWINI	S	sucsub.f	Initialize suction distribution and related variables to zero for all BL surfaces.
VWREAD	S	sucsub.f	Read suction distribution $\nu_w$ for BL surfaces from file suction.xxx.
VWSET	S	sucsub.f	Set suction distribution $\nu_w$ in arrays for every surface and BL grid node for easy access during calculating the BL variables and $\delta_{\text{suction}}^*$ . This routine has to be recalled after every solution update since due to the movement of the stagnation point also the BL grid nodes may move.

### 3.3. MOMENTUM INTEGRAL RELATIONS

The two-equation integral boundary layer formulation (consisting of the von Kármán integral boundary (3.5a) and the kinetic energy shape parameter equation (3.5b)) modified to account for boundary layer suction are given in equations (3.5), the additional terms are highlighted in red:

$$\frac{C_f}{2} = (H+2 - M_e^2) \frac{\theta}{u_e} \frac{du_e}{d\xi} + \frac{d\theta}{d\xi} - \frac{\rho_w \nu_w}{\rho_e u_e} \quad (3.5a)$$

$$\theta \frac{dH^*}{d\xi} + (H^{**} + H^*(1-H)) \frac{\theta}{u_e} \frac{du_e}{d\xi} = \left( C_{\mathcal{O}} + \frac{\rho_w \nu_w}{\rho_e u_e} \right) - H^* \left( \frac{C_f}{2} + \frac{\rho_w \nu_w}{\rho_e u_e} \right) \quad (3.5b)$$

Note that they can be formulated in such a way that the case including boundary layer suction remains a subset of the general relations (they are obtained again simply by setting  $\nu_w$  to zero). The quotient  $\frac{\rho_w \nu_w}{\rho_e u_e}$  will return very often, therefore it is useful to define it as the local suction coefficient:

$$C_\mu = \frac{\rho_w \nu_w}{\rho_e u_e} \quad (3.6)$$

Several unknowns in equations (3.5) are not accounted for, and so called ‘closure relations’ are necessary that link the unknowns of the integral relation to each other [55, 58]. For turbulent boundary layers with suction significant modification of these relations is necessary because the shear stress profile in the boundary layer changes significantly. Merchant developed [3] alternative closure relations able to cope with boundary layer suction, these are described in section 3.4 [3, 56].

#### 3.3.1. VON KÁRMÁN INTEGRAL BOUNDARY RELATION

The equation given in equation (3.5a) can be multiplied by  $\frac{\xi}{\theta}$  which gives, after bringing also  $\frac{1}{u_e}$ ,  $\frac{1}{\xi}$  and  $\frac{1}{\theta}$  behind the differential operator ‘d’:

$$\frac{\xi}{\theta} \frac{C_f}{2} = (H+2 - M_e^2) \frac{d \ln u_e}{d \ln \xi} + \frac{d \ln \theta}{d \ln \xi} - \frac{\xi}{\theta} C_\mu$$

The advantage of multiplying by  $\frac{\xi}{\theta}$  is that after discretization the differenced terms will be in logarithmic form and yield exact results for the similarity station at the stagnation point. Doing this between two BL stations 1 ( $i-1$ ) and 2 ( $i$ ), figure 3.5 serves as an illustration for this, gives:

$$\frac{\xi_a}{\theta_a} \frac{C_{f_a}}{2} + \frac{\xi_a}{\theta_a} C_{\mu_a} = (H_a+2 - M_{e_a}^2) \frac{\ln(u_{e2}) - \ln(u_{e1})}{\ln(\xi_2) - \ln(\xi_1)} + \frac{\ln(\theta_2) - \ln(\theta_1)}{\ln(\xi_2) - \ln(\xi_1)} = (H_a+2 - M_{e_a}^2) \frac{\ln\left(\frac{u_{e2}}{u_{e1}}\right)}{\ln\left(\frac{\xi_2}{\xi_1}\right)} + \frac{\ln\left(\frac{\theta_2}{\theta_1}\right)}{\ln\left(\frac{\xi_2}{\xi_1}\right)}$$

The above equation can be multiplied by  $\left(\frac{\xi_2}{\xi_1}\right)$  to eventually arrive at the discretized equation that is implemented in MSES:

$$Z = -\frac{C_{f_x}}{2} \ln\left(\frac{\xi_2}{\xi_1}\right) + (H_a+2) \ln\left(\frac{u_{e2}}{u_{e1}}\right) + \ln\left(\frac{\theta_2}{\theta_1}\right) = 0 \quad (3.7)$$

with  $C_{f_x} = \frac{\xi_1}{\theta_1} \left( \frac{C_{f1}}{2} + C_{\mu1} \right) + \frac{\xi_2}{\theta_2} \left( \frac{C_{f2}}{2} + C_{\mu2} \right)$

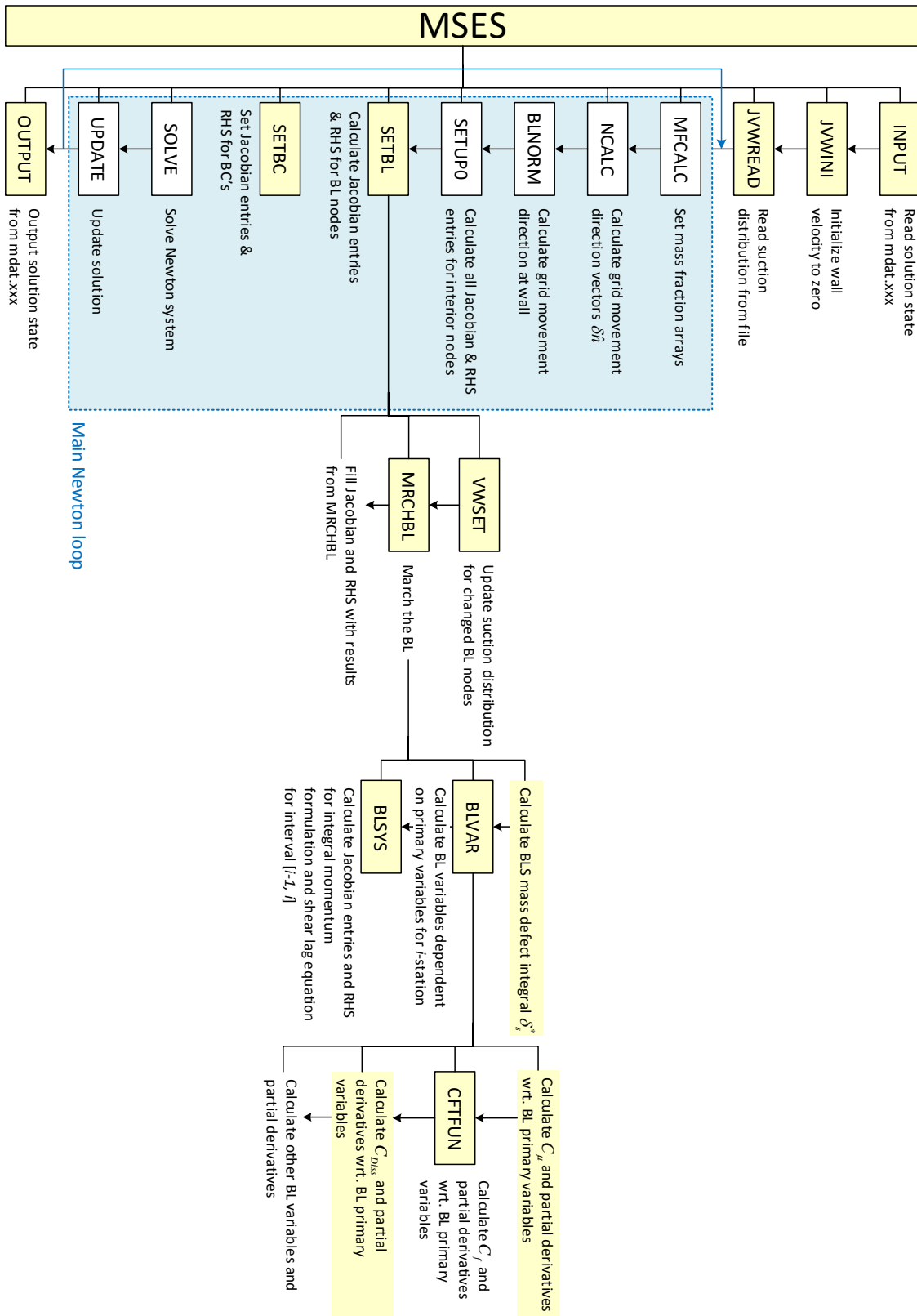


Figure 3.4: Structure of MSES code with emphasis on boundary layer calculations and modifications to account for suction. Modified routines are highlighted in yellow and a brief overview of their purpose and the modifications is given in table 3.1.

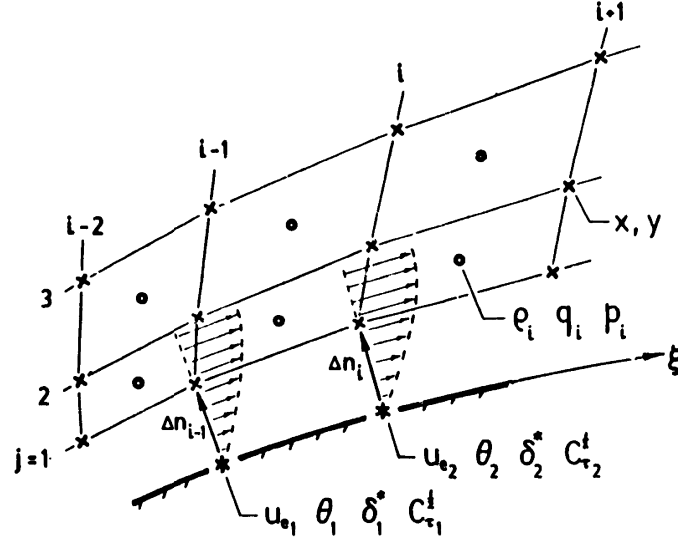


Figure 3.5: BL variable locations for discretization. [55]

### 3.3.2. KINETIC ENERGY SHAPE PARAMETER EQUATION

Equation (3.5b) is treated in a similar fashion as the von Kármán integral BL equation. After multiplying by  $\frac{\xi}{H^*\theta}$  and discretization the form implemented in MSES is obtained:

$$Z = \ln\left(\frac{H_2^*}{H_1^*}\right) + \ln\left(\frac{u_{e2}}{u_{e1}}\right) \left(2\frac{H_a^{**}}{H_a^*} + 1 - H_a\right) + \ln\left(\frac{\xi_2}{\xi_1}\right) \left(\frac{1}{2}C_{f_x} - C_{\mathcal{D}_x}\right)$$

with

$$C_{f_x} = \left(\frac{\xi}{\theta} (C_f + 2C_\mu)\right)_a \quad (3.8)$$

$$C_{\mathcal{D}_x} = \left(\frac{\xi}{\theta} \left(\frac{2C_{\mathcal{D}}}{H^*} + \frac{C_\mu}{H^*}\right)\right)_a$$

$C_{f_x}$  and  $C_{\mathcal{D}_x}$  are actually weighted averages, calculated in the same fashion as  $C_{f_x}$  in equation (3.7), but with an optional bias towards BL station 1 or 2.

## 3.4. CLOSURE RELATIONS

The closure relations are developed with a distinction being made between laminar and turbulent boundary layers. The bases for the closure relations for both types of boundary layer flow are:

- the Falkner-Skan family of velocity profiles for the laminar closure;
- Triple deck theory for the turbulent boundary layer: the boundary layer is composed of the viscous sublayer and the outer layer and these two regions are connected by an interim region known as the 'log-layer' — the viscous sublayer and log-layer together are also referred to as the inner layer. This allows the assumption that close to the wall pressure gradients do not play a role and in the outer layer that viscous effects can be neglected, since this region is dominated by transport phenomena — see e.g. [59].

For the sake of completeness, it is worth mentioning that a third type of boundary layer flow is distinguished in MSES: '*similar flow*'. This type of flow only occurs at the very first boundary layer station (i.e. at the stagnation point). As one may already expect, this type of flow also does not need any modifications to include boundary layer suction.

### 3.4.1. LAMINAR CLOSURE

Merchant reports some minor deviation of the friction coefficient  $C_f$  from the original closure relation for when suction is applied. Despite that he concludes that the original closure relations for a laminar boundary

layer (not including suction) are adequately suited to be used in conjunction with BLS, both for continuous and discontinuous cases. The original relations are presented by Drela in [55] and shown in equations (A.1), found in appendix A.

### 3.4.2. TURBULENT CLOSURE

According to Merchant the kinetic shape parameter  $H^*$  gives very similar results when compared to the laminar one and does not need modifications to account for boundary layer suction. In contrast to this, the closure relations for the friction coefficient  $C_f$  and the dissipation coefficient  $C_\mathcal{D}$  are found to be highly affected by the inclusion of boundary layer suction. Fortunately, the assumption that lies at the basis of the formulation of these closure relations, namely the existence of a layer in the BL that is dominated by wall effects — the inner layer — and an outer layer. As one can already expect, it is in the inner layer that the boundary layer suction has the most profound effect and it suffices to modify the terms related to this layer.

Merchant's modification involves a changed shear stress profile for the inner layer, based on the assumption that in the inner layer the stream wise variation in  $u$  can be neglected:

$$\tau = \underbrace{\tau_w + \rho u u_w}_{\text{Contribution inner layer}} + \underbrace{\eta \frac{dp_e}{d\xi}}_{\text{Contribution outer layer}}$$

(Since only changes to the inner layer are considered, the last term can be neglected but it is shown for completeness). This allows to relate  $\tau_w$  without suction to  $\tau_w$  with suction. Subtracting the result without suction from the case with suction gives:

$$\Delta\tau = \tau_w - \tau_{w,w/o \text{ suction}} + \rho u u_w$$

The velocity profiles of the inner layer and the outer layer match each other at some 'slip velocity'  $U_{\text{slip}}$ . At this slip velocity, where  $\eta \rightarrow \infty$ ,  $u \rightarrow u_s$  and  $\Delta\tau \rightarrow 0$  one gets:

$$\tau_w = \tau_{w,w/o \text{ suction}} - \rho u_w u_s \quad \Rightarrow \quad C_f = C_{f,w/o \text{ suction}} - 2 \frac{\rho_w u_w}{\rho_e u_e} U_{\text{slip}}$$

The closure relation for the skin friction coefficient without friction is given in equation (A.2b).

The dissipation coefficient is obtained by simply inserting this newfound value for  $\tau_w$  into equation (3.9):

$$\begin{aligned} C_\mathcal{D} &= \underbrace{\frac{\tau_w u_s}{\rho_e u_e^3}}_{\text{Contribution inner layer}} + \underbrace{\frac{1}{\rho_e u_e^3} \int_0^1 \tau \frac{du}{d\eta} d\eta}_{\text{Contribution outer layer}} \\ &= \underbrace{\frac{C_f}{2} U_{\text{slip}} - \frac{\rho_w u_w}{\rho_e u_e} U_{\text{slip}}^2}_{\text{Contribution inner layer}} + \underbrace{C_\tau (1 - U_{\text{slip}})}_{\text{Contribution outer layer}} \end{aligned} \quad (3.9)$$

A complete overview of the closure relations for the turbulent BL with suction are given in equations (A.2).

In equation (3.9),  $C_\tau$  is the maximum shear stress coefficient in the outer layer. It provides a way of including history effects in the turbulent BL model, i.e. it models upstream influence on the BL at a more downstream point; thus the common assumption of a local-equilibrium BL does not have to be made. This is important at points where adverse pressure gradients get increasingly severe and in abrupt 'relaxing' conditions, e.g. at the trailing edge. To model this correctly, an ODE is required for  $C_\tau$ . This is the *shear lag equation*, already presented in equation (3.2c) and repeated below:

$$\frac{\delta}{C_\tau} \frac{dC_\tau}{d\xi} = 4.2 \left( \sqrt{C_{\tau(\text{eq})}} - \sqrt{C_\tau} \right) + \left( \frac{2\delta}{u_e} \frac{du_e}{d\xi} \right)_{(\text{eq})} - \left( \frac{2\delta}{u_e} \frac{du_e}{d\xi} \right) \quad (3.10)$$

Contrary to the integral boundary relations in section 3.3 this equation does not need to be modified for boundary layer suction.

## 3.5. COUPLING CONDITION

The well-known coupling condition that the displacement thickness equals the displacement of the inviscid streamlines ( $\delta^* = \Delta n$ ) is compromised by applying boundary layer suction. The underlying physical explanation for the displacement thickness is that it accounts for the retarded (air) mass in the boundary layer

by ‘matching’ the retarded mass to the mass that is virtually ‘blocked’ by ‘displacing’ the body. However, by applying suction — and wall transpiration in general — part of the mass in the boundary layer is sucked away and therefore also the displacement of the inviscid body  $\Delta n$  changes. Evidently, in case of suction part of the retarded mass is sucked away, effectively reducing the displacement thickness. Without suction, the mass defect is given by (see e.g. [11]):

$$\dot{m}_{\text{defect}} = \rho_e u_e \delta^* \quad (3.11)$$

Taking into account the mass removed by suction this becomes (up to a point  $\xi_i$  along the BL):

$$\dot{m}_{\text{defect}} = \rho_e u_e \delta^* + \int_0^{\xi_i} \rho_w v_w d\xi = \rho_e u_e \Delta n$$

This can be easily rewritten to get  $\Delta n$ :

$$\Delta n = \delta^* + \delta_{\text{suction}}^* = \delta^* + \frac{1}{\rho_e u_e} \int_0^{\xi_i} \rho_w v_w d\xi \quad (3.12)$$

From equation (3.12) can be readily observed that  $\Delta n$  is dependent upon the solution for  $\rho_e$  and  $v_w$ . Return now to figure 3.2 and observe the Jacobian entries for the coupling condition: these are simply 1 and  $-1$ . However, with the new equation for  $\Delta n$  given by (3.12) this situation changes completely. The Jacobian for  $\delta n$  must be altered (to account for additional term that contains  $u_e$ , as well as  $\delta\rho$ ). This is not a trivial task and another approach is desired. An obvious choice is to treat the integral as a constant during a Newton iteration, only add it to the RHS of the overall Newton system and ‘hope for the best’, i.e. rely on the assumption that the changes after an update of  $\delta_{\text{suction}}^*$  are small enough so the iterative Newton system solver is not thrown ‘off track’. This is the approach that is opted for, and which has shown to work very well after implementation.

### 3.6. THE ‘MAT’ IN MATSESUCTION

Besides adapting MSES for suction, it is also worth briefly mentioning the effort that went into integrating MSES with Matlab<sup>®</sup>. While MSES is quite complete on itself with some pre- (AIRFOIL, MSET) and several good post-processing (MPLOT, MPOLAR, XPOLAR,...) tools, going through the trouble of linking it to Matlab has several advantages<sup>1</sup>:

- All the original programs require user-interaction for setting up an analysis or post processing the results, even just running them requires starting them from the command line. By rewriting the code and changing the input arguments this process can be controlled from Matlab<sup>®</sup>.
- With the input and output data available in Matlab<sup>®</sup> it is much easier to code a customized analysis of the data.

Especially the first point is interesting. If Matlab<sup>®</sup> can take control of setting up and running a complete analysis — determined by predefined parameters — it is eventually possible to queue a large amount of cases to be run. This allows to take full advantage of the benefits of a solver of the ‘viscid-inviscid interaction’ kind: contrary to simulations entirely based on finite difference, running one analysis with MSES typically takes not very long — on today’s computers typically on the order of minutes, i.e. the same order of magnitude of setting up an analysis manually. Actually doing this manually and sequentially would obviously lead to a huge loss of time. By specifying arrays for a desired variation of any parameter and automatically queueing them this can be avoided, thus also avoiding losing one the inherent advantages of ‘viscid-inviscid interaction’ aerodynamic simulations. This approach also makes it possible to store the results in a systematic way which in turn allows to analyse the data efficiently. As mentioned Matlab<sup>®</sup> was used as the platform for the changes presented in this chapter, but of course any other environment would do. The choice for Matlab<sup>®</sup> stems basically from the author’s familiarity with it, its availability to the author and its existing environment providing an extensive framework for data analysis and (visual) presentation of it.

To facilitate this idea of controlling MSES through Matlab<sup>®</sup>, several of the original programs in the ‘MSES package’ were altered. The main alterations were aimed at:

<sup>1</sup>But Matlab<sup>®</sup> has to be available to the user...

- removing 'read'-statements, i.e. removing all points in the code where the program waits for user input and replace it by information passed either directly as arguments or indirectly through input-files;
- adding some extra control by making parameters previously defined during compile-time an adjustable variable (limited);
- automatizing the generation of output files.

Figure 3.6 shows how the several MSES programs, the in- and output files and Matlab<sup>®</sup> communicate with each other; it provides a nice overview to discuss the changes to them. At the centre of all information is the `mdat.xxx` file, containing all the 'state' information of a certain (possibly unconverged) solution. This file was only changed to contain some information about suction parameters, but it is not used directly by the 'Matlab extension'. Instead, data analysis is performed on the basis of output files provided by special versions of MPLOT: a version that provides the complete flowfield, grid and boundary layer parameters stored in `mdat.xxx`, and a version tailored to work in conjunction with MPOLAR<sup>2</sup> that provides these output files for every angle of attack for which MPOLAR reaches a converged solution. For all these output files, a Matlab<sup>®</sup> code was designed that reads the files and stores them into meaningful data structures after which virtually any desired analysis can be performed.

So far for the output. The input is done through input files and a limited amount of arguments. Figure 3.6 shows that the input files `blade.xxx` (containing coordinates that describe the airfoil), `m ses.xxx` (specifying the run parameters for MSES such as far field type,  $M$  and  $Re$  number), `gridpar.xxx` (containing all the parameters necessary for constructing the grid) and `spec.xxx` (which contains an array of angles of attack that MPOLAR sweeps through). The 'Matlab-extension' can automatically generate all of these files with the desired settings (in case of `blade.xxx` this becomes effectively an airfoil analysis program that acts a replacement for the program AIRSET).

With all input parameters being able to be controlled through Matlab<sup>®</sup>, the goal of queueing large amounts of cases resulting from the need to analyse one or more varying parameter becomes possible. For this another piece of code is available, the so-called 'RUNNER' that takes control over first creating all the input files and arguments from the input parameters and subsequently calls either MSES or MPOLAR to do the analysis (in figure 3.6 the runner is represented by the blocks on the left). After the analysis is complete the 'RUNNER' goes on to the next set of input parameters and so on. The 'RUNNER' can take an array of values for any amount of parameters that need to be varied for which it constructs all possible combinations. Obviously the amount of data that is acquired in this way quickly 'explodes', so the 'RUNNER' also takes care of saving the data comprehensively for easy access. After the analysis the produced output is checked and a report is presented that gives information on how well the different cases converged for the requested input parameters.

What rests is the analysis of the data. Ultimately all the data needs to be translated to form a dataset (e.g. a set of cases with a varying flap deflection) for which the parameters can be compared (e.g. the lift coefficient for a certain angle of attack) and plotted. To this end, the 'Matlab-extension' contains a piece of code that retrieves the desired information from all the available cases.

---

<sup>2</sup>MPOLAR is a program that can run MPLOT for a specified array of angles of attack and as such can create a lift and drag polar.

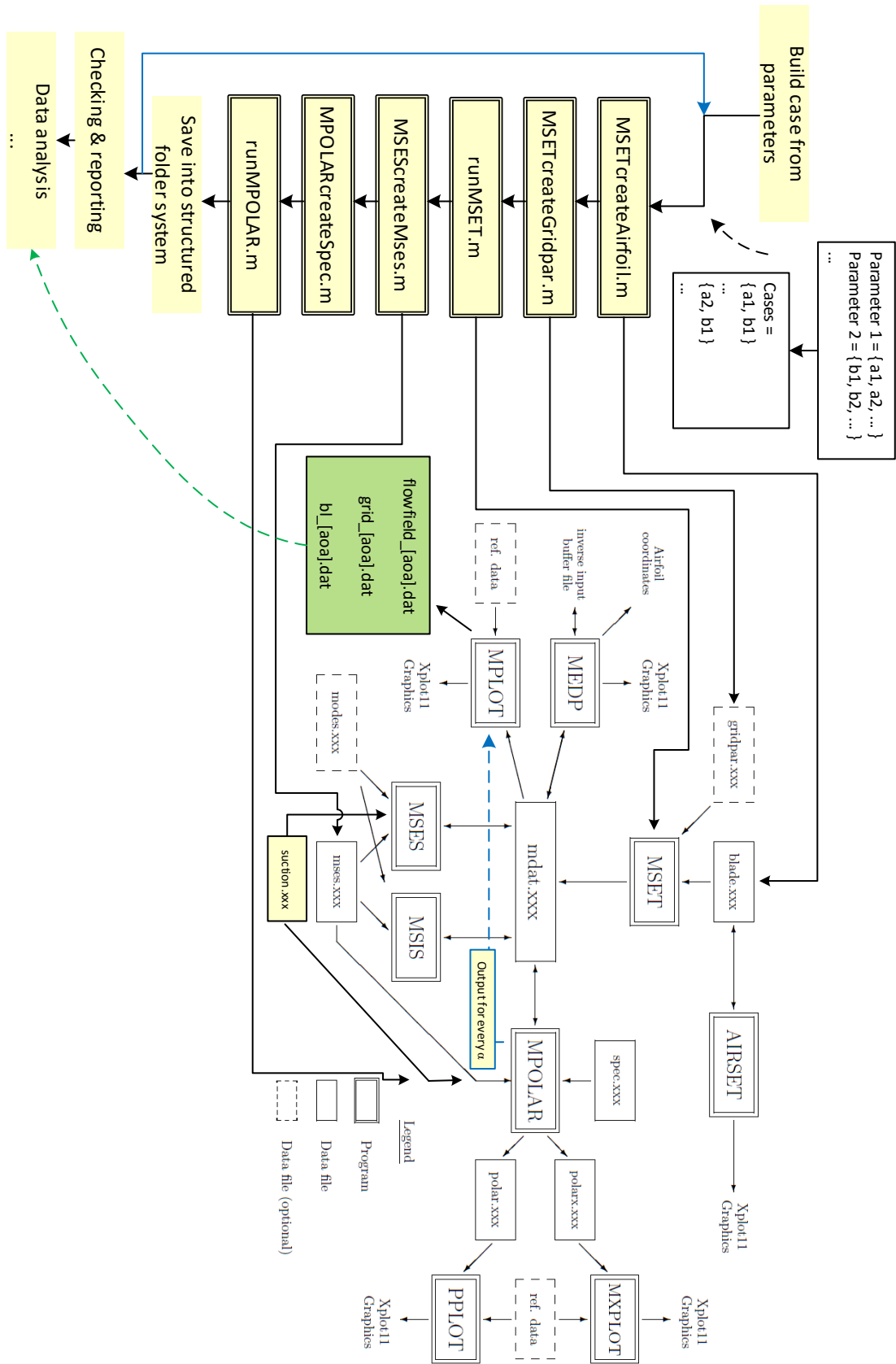


Figure 3.6: Link between MSES programs, in- and output files and 'Matlab-extension'. MSES roadmap' taken from [57].

# 4

## VALIDATION MSES ADAPTION FOR SUCTION

Experimental data for airfoils with continuous suction or slot suction are surprisingly scarce<sup>1</sup>, and even for flows over a flat plate with a ‘porous wall’ experimental data is hard to get by. Experiments performed by Favre et al in 1961 however were available and are particularly relevant for validating the modifications for suction, since it presents data for the development of several BL parameters for different suction values [60]. Section 4.1 shows how the results of MatSESuction compare to the experiment by Favre et al.

Because of the different nature of slot suction (as opposed to continuous suction) a comparison of slot suction on a flat plate with experimental data is presented in section 4.2. The experimental reference data are obtained from T. van der Hoeven who did several experiments with slot suction for his thesis at the faculty of Aerospace engineering of the TU Delft [45].

Because it is worthwhile not only to examine the flow over a flat plate but also over an airfoil the results of the adapted code are also compared to the results from rFoilsuc. This code is a modification of the rFoil code, developed in-house at the faculty of Aerospace engineering of the TU Delft, by Gael de Oliveira to simulate suction [4].

### 4.1. POROUS FLAT PLATE EXPERIMENT BY FAVRE ET AL

In an experiment performed by Favre et al several boundary layer properties are measured for the flow over a flat plate, this for several suction quantities:  $v_w/V_\infty = 0.001, 0.005$  and  $0.016$  (as well as a case without suction) [60]. The flow first travels over a flat plate without suction of 1026 mm, after which it continues over a perforated plate of 920 mm where suction can be applied. The perforated plate suffers from some deformations, extending to 0.7 mm which is considerable compared to the measured displacement and momentum thickness. It is reported that transition occurs almost immediately at the leading edge. In the context of validating MatSESuction the measurements that chart the development of  $\delta$ ,  $\theta$  (and  $H$ ) are the most relevant, since the integral BL formulation in MSES obviously cannot deliver detailed boundary layer information. These are also the properties that are most relevant for eventually determining separation.

Simulating a flat plate in MatSESuction poses the problem of the leading edge of the plate: introducing corners at the leading edge will trigger separation, which is of course undesirable. A simple rounded edge could avoid this, but will in turn introduce suction peaks influencing the flow and separation is still likely. Narashima and Prasat recommend using a cubic super-ellipse, which looks like a rectangle with chamfered corners to avoid separation, but suction peaks are still present. Despite that this is still the most favourable shape. Note that a convenient feature of the measurements by Favre et al is that the suction starts only approximately halfway the plate so the influence of the leading edge on the BL at the measurement location can remain limited.

The simulated plate is shown in figure 4.1, as well as the suction distribution. The flow is tripped at the leading edge of the plate in accordance with the experiment by Favre. The simulations were performed at a

---

<sup>1</sup>Or at least very hard to get by.

freestream Reynolds number of approximately  $7.5 \cdot 10^5$  and a Mach number of 0.1. A lower value for  $M$  would be desirable but MSES becomes unstable at low values for  $M$ , but despite that a value of  $M = 0.1$  should already be sufficient to minimize compressibility effects.

#### 4.1.1. DEVELOPMENT OF THE BL PARAMETERS

Figure 4.2 shows the development of  $\delta^*$ ,  $\theta$  and  $H$  over the perforated plate for several suction values. For the suction cases it can be seen that the displacement thickness and momentum thickness are generally slightly overpredicted by the code. Near the start of suction a peak in both  $\delta^*$  and  $\theta$  can be observed for the experimental data. However, it can be said with certainty that this is *not* related to the application of suction, but due to impurities in the suction surface at this location<sup>3</sup>; hence it is not an issue that this behaviour is not picked up by the simulation with MatSESuction. In any case, the difference between simulation and experiment for the suction cases is of the same order of magnitude as the difference for the case without suction, which represents the performance of the original MSES code. The notably worse correlation of the simulated  $\delta^*$  and  $\theta$  with the experimental ones for  $\nu_w/V_\infty = 0.005$  is remarkable, since for a much larger suction value of  $\nu_w/V_\infty = 0.016$  is again much better. No specific cause was found for this.

The kink that can be observed in the simulated  $\delta^*$  for  $\nu_w/V_\infty = 0.016$  (at  $x = 1.175$  m) is due to the abrupt change in  $\delta_{\text{suction}}^*$  at this point. Here,  $\delta_{\text{suction}}^*$  exceeds the displacement thickness itself, which is limited in the code to  $\delta^*$  to avoid instability. Also the suction value 0.005 already causes  $\delta_{\text{suction}}^*$  to exceed  $\delta^*$  but the change is not as abruptly since the rate at which  $\delta_{\text{suction}}^*$  decreases is lower.

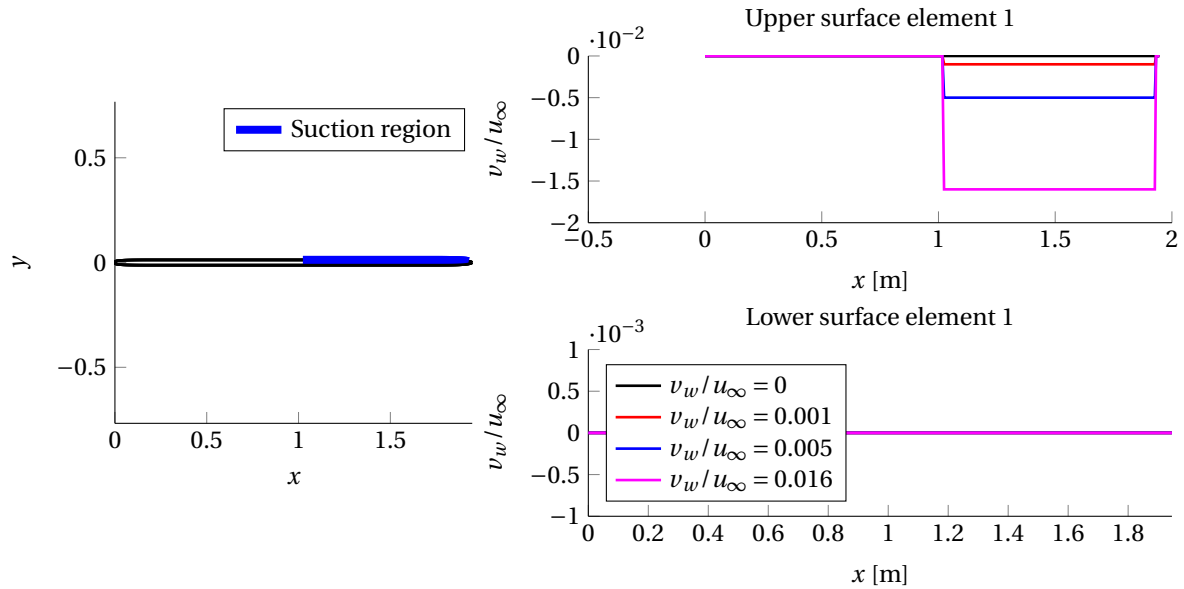


Figure 4.1: Suction location and distribution for the validation case with Favre's data.

## 4.2. SLOT SUCTION EXPERIMENT BY VAN DER HOEVEN

As already explained in section 2.2.2 the nature of slot suction is very different from continuous suction, and notoriously more difficult to simulate. In this context it is a good idea to compare the results of MatSESuction to available reference data specifically for slot suction.

<sup>2</sup>The Reynolds number  $Re$  at which the Favre experiment is performed is not entirely clear and is obtained in an indirect way. We know that the Reynolds number at start of suction ( $Z = 0$  or  $z = 1026$  mm which is the coordinate along the plate right before the start of suction, please see [60] for reference) is  $Re_{\delta, Z=0} = \left( \frac{u_e^* \delta}{\nu} \right)_{Z=0} = 16300$  where  $\delta = 22.5$  mm (mentioned in the introduction). From MSES it is difficult to obtain  $Re_{\delta}$  since  $\delta$  is not readily available, so another reference length is desirable. As an alternative,  $\theta$  is a relevant BL parameter to use as the reference length with the bonus of  $Re_{\theta}$  being readily available from the output generated by MatSESuction. From the knowledge that  $Re_{\delta, Z=0} = 16300$  the Reynolds number based on  $\theta$  can be calculated by  $Z = 0$ :  $Re_{\theta, Z=0} = Re_{\delta, Z=0} \cdot \left( \frac{\theta}{\delta} \right)_{Z=0}$ , where  $\delta$  is given as being 0.0225 m, and  $\theta$  can be obtained from the charted data of the experiment. With  $Re_{\theta, Z=0}$  available, the simulation in MatSESuction can finally be matched to the experiment. In practice, for all cases this corresponds to a freestream Reynolds number of approximately  $Re_\infty \approx 7.5 \cdot 10^5$ .

<sup>3</sup>For more information about this problem the reader is referred to the original reference [60].

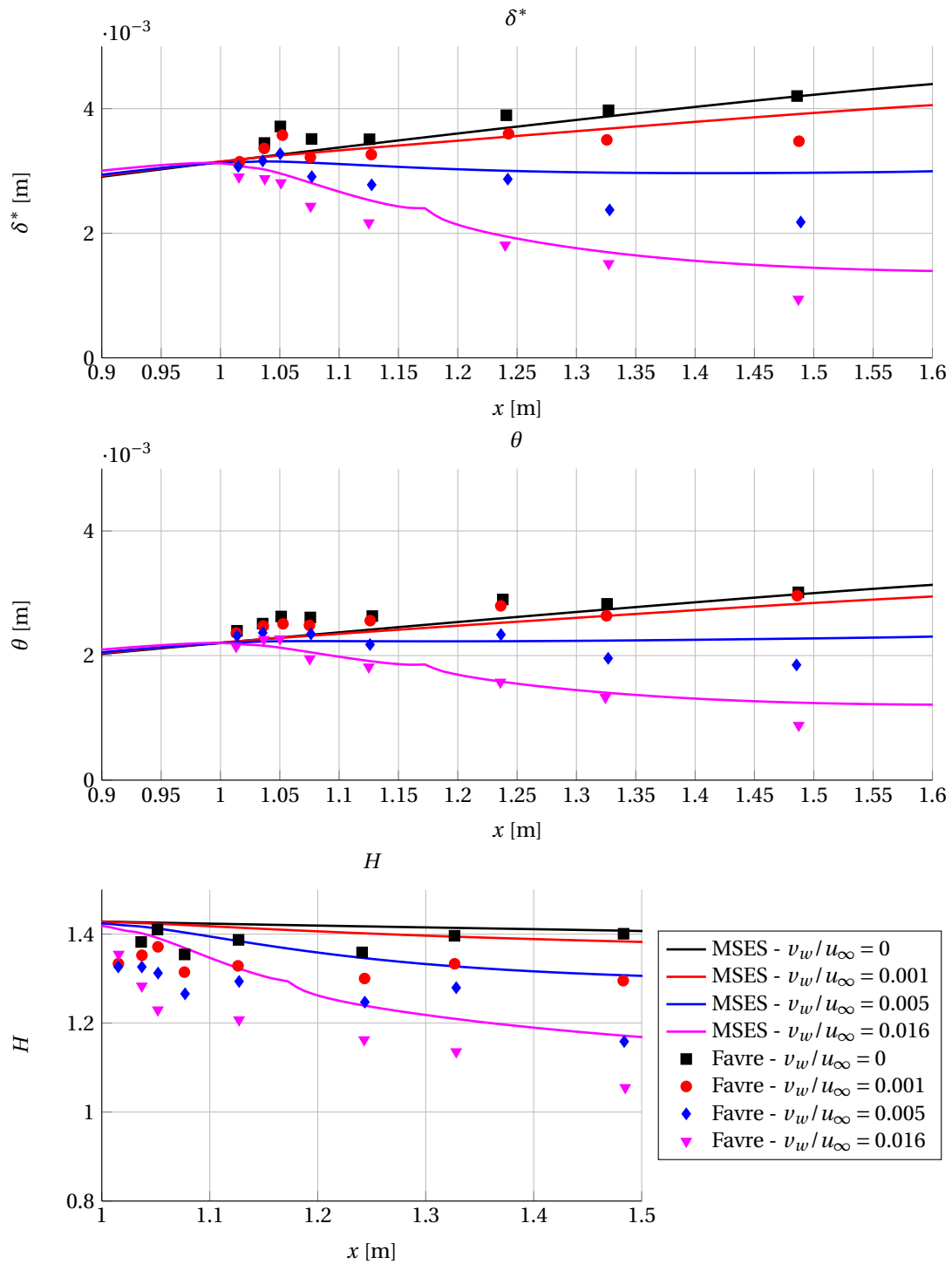


Figure 4.2: Comparison of MatSESuction with Favre's experimental data [60]:  $\delta^*$ ,  $\theta$ ,  $H$ .

T. van der Hoeven performed extensive experiments for slot suction on the flow over a flat plate with a turbulent boundary layer. These experiments were carried out in the context of his master's thesis in 2013 at the faculty of Aerospace Engineering of the TU Delft [45]. The experiment involves measurements with pressure tabs, PIV and hot-wire anemometry. The experimental set-up consists of flat plate of 2.85 m preceded by a convergent nozzle. The suction slot is at the end of the plate, after which it extends somewhat further, also with the possibility of creating a divergent nozzle to introduce an adverse pressure gradient. The width of the suction slot of the experiment considered here is 10 mm.

At the suction location a local Reynolds number of  $Re_{\theta,0} \approx 10100$  is reported, corresponding to a local momentum thickness of  $\theta_0 = 5.6 \text{ mm}$ <sup>4</sup>. The subscript '0' here refers to the location where suction is applied and to the test case without suction.

#### 4.2.1. DIFFERENT SUCTION MODELS

Figure 4.3 shows the variation of the pressure coefficient near the suction slot for a suction level of  $v_w/u_\infty = -0.2225$ . The black dots indicate the pressure coefficient as measured by the pressure tabs. Since it is difficult to perform measurements with pressure tabs on the slot location the results of another measurement method are shown as well: the pressure coefficient is extrapolated from PIV data, indicated by the solid black line. This data shows that, even more than the pressure tab measurements suggest, a strong suction peak followed by a sharp drop in the pressure coefficient. This result is expected for slot suction: it acts as a sink on the outer flow, accelerating the flow in front of followed by a deceleration behind it. The extent of the peaks should be viewed with some care however. Two simulation results are presented in the same figure: the 'Merchant'- and the 'Oliveira'-model. Concerning suction, both models are nearly exactly the same, but the 'Oliveira'-model (blue intermittent line) does not include a displacement of the inviscid streamlines due to the missing mass flow caused by suction ( $\delta_{suction}^*$ ) while the 'Merchant'-model does (red intermittent line). As can be expected the model including an additional displacement of the outer streamlines causes peaks to be stronger, since the decrease in  $\Delta n$  is more abrupt. Comparing this with the experimental PIV-data it can be concluded that including a displacement  $\delta_{suction}^*$  due to the missing mass flow from suction is the better model — in particular when it comes to slot suction.

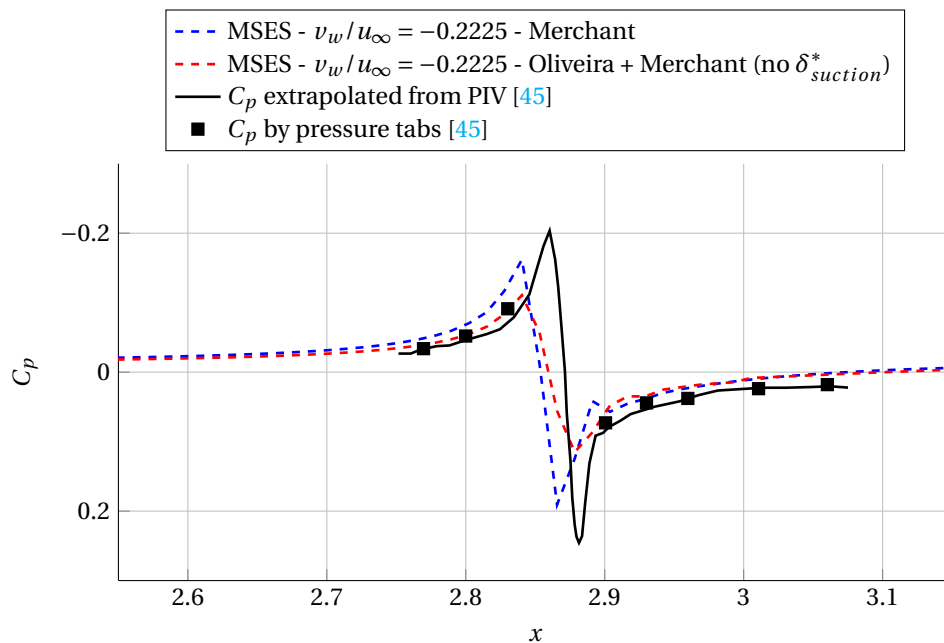


Figure 4.3:  $C_p$  for slot suction: difference between simulation with  $\delta_{suction}^*$  and without it.

#### 4.2.2. SLOT SUCTION FOR DIFFERENT SUCTION LEVELS

Figure 4.4 shows the pressure coefficient for several suction levels, compared to the experimental results from van der Hoeven [45]. The agreement for the several suction levels is very good and shows that the simulation

<sup>4</sup>Just like for the Favre experiment, the local momentum thickness  $Re_{\theta,0}$  was matched

models can cope with the special nature of slot suction with its abrupt changes in the outer flow; at least when it comes to the pressure distribution.

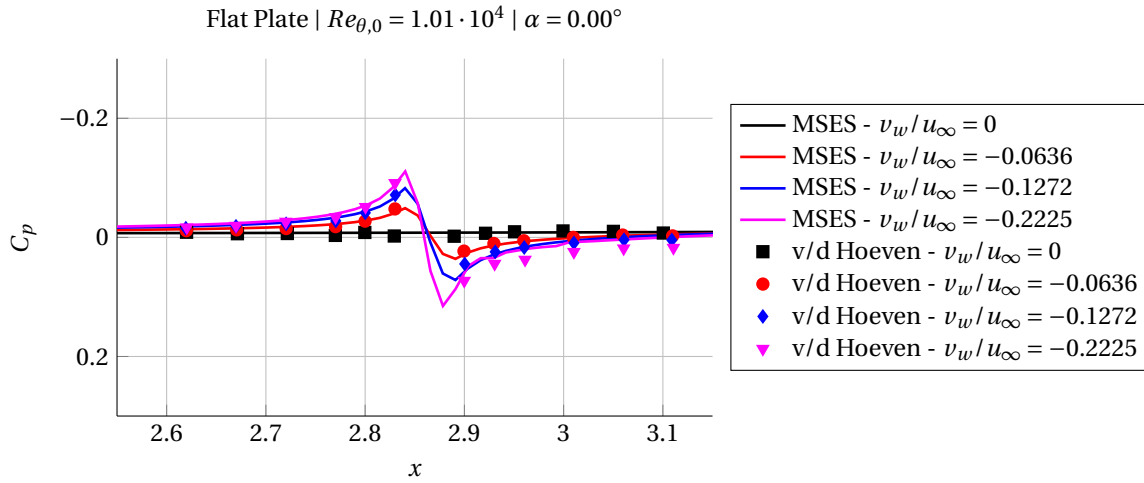


Figure 4.4: Comparison  $C_p$  for slot suction with data by van der Hoeven [45].

Figure 4.5 shows the momentum thickness near the slot. The simulation predicts an almost discrete decrease in momentum thickness. This fits the theoretical expectation that by sucking away part of the boundary layer the momentum deficit is (strongly) decreased. The experiments on the other hand reveal something else: a peak in  $\theta$  occurs at the slot, after which it follows more or less the trend it followed before the suction slot. This is most probably due to a highly turbulent region involving flow recirculation and local separation in the neighbourhood of the slot, caused by the appearance of the stagnation point at the suction slot entrance in section 2.2.2. This phenomenon however remains confined to the immediate neighbourhood of the slot and after a certain ‘settling’ length the momentum thickness ‘stabilizes’ again. Experiments with direct numerical simulation of slot suction also show this behaviour with a peak in  $\theta$ , but also predict a more pronounced decrease in  $\theta$  once it has stabilized again [61]. It remains unclear why the experimental data in figure 4.5 does not show this. It is however clear that MatSESuction cannot simulate this behaviour. It is important to keep in mind that the decrease in  $\theta$  is overpredicted, since it influences the shape parameter  $H$  directly and as such also the prediction of separation.

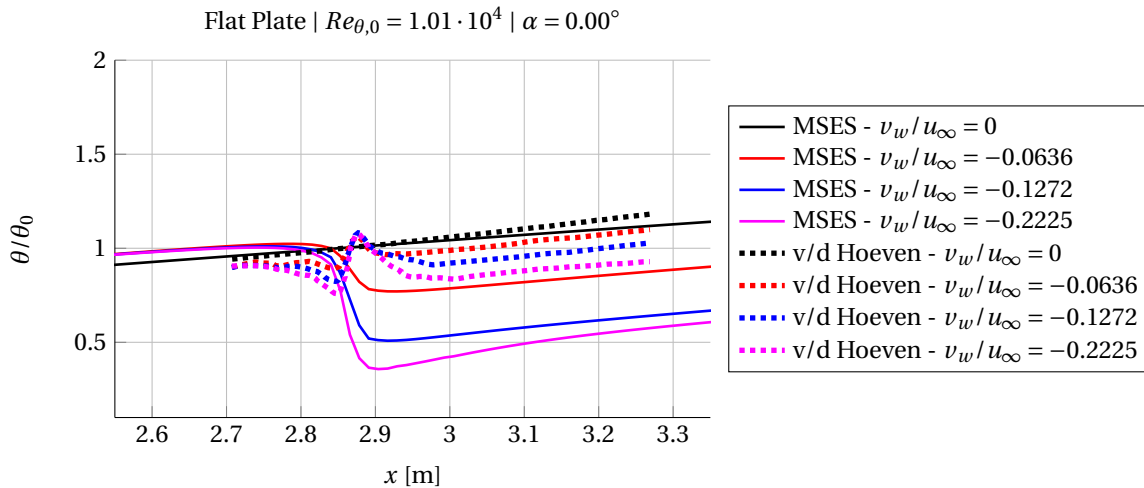


Figure 4.5: Comparison  $\theta/\theta_0$  for slot suction with data by van der Hoeven [45].

### 4.3. COMPARISON WITH rFOILSUC

rFoilsuc is an aerodynamic solver just like MSES, developed in house at the TU Delft at the faculty of aerospace

engineering based on the well-known XFOIL code (also originally developed by Mark Drela). So far, the results of MatSESuction have only been compared against flat-plate experiments, but it would be nice to also validate its performance for actual airfoil geometries. Experimental data is lacking for this unfortunately, but the results can be compared against the results of another solver that has already been validated and used frequently at the faculty of aeronautical engineering, i.e. the earlier introduced rFoilsuc code. The adaption and validation of rFoil for suction is described in [4].

The choice of what airfoil and suction distribution is discussed in this section is somewhat arbitrary, but the choice was to use the NACA0012 airfoil with suction being applied from  $x/c = 0.6$  to  $x/c = 0.9$ . The NACA0012 airfoil is frequently used as the airfoil of choice when validating CFD calculations and quite a lot of literature is available for it, hence the choice for this airfoil. In the context of this project it is expected that suction will be applied towards the trailing edge (see section 5.1), hence the choice for the suction location. Three different suction levels are compared:  $v_w/u_\infty = 0.005$  and  $0.01$ ; apart from a case without suction of course. The suction location and distributions are shown in figure 4.6.

Figures 4.7 – 4.9 show the development of the skin friction coefficient  $C_f$ , displacement thickness  $\delta^*$  and the momentum thickness  $\theta$  on the upper side of the airfoil. As can be expected, suction makes the skin friction coefficient rise sharply. This is due to the ‘pulling’ effect of BLS, causing high values of  $\frac{\partial u}{\partial y}$  and hence  $C_f$ ; explained earlier in section 2.2.2. Very good agreement can be observed between the results of MatSESuction and rFoilsuc. Small differences can be attributed to a slight modeling difference: MatSESuction models the displacement of the inviscid region accounting for the mass defect in the BL due to suction, while rFoilsuc does not. Since it was found in the previous section that the former performs better — at least when it comes to slot suction — this model is used here as well<sup>5</sup>; the differences remain small however. Also  $\delta^*$  and  $\theta$  show very good agreement. The good agreement between the two codes is not a total surprise however since the BL formulation and closure models are almost identical.

The lift polars for the same configurations as those discussed above are compared in figure 4.10, including experimental data from Abbott and Doenhoff for reference (this is for the case without suction of course) [14]. Again, the agreement is very good, except for the region near  $C_{l_{max}}$ . MatSESuction struggles to converge to the right solution here, which is evidenced by the somewhat irregular shape of the lift polar in this area. At least for the non-suction cases, it is known that rFoilsuc has superior models for this, especially developed and implemented for modeling near  $C_{l_{max}}$  but it still cannot predict the sharp drop in lift past  $\alpha_{C_{l_{max}}}$ . In any case, from these results it is advisable to use the results near  $C_{l_{max}}$  with care.

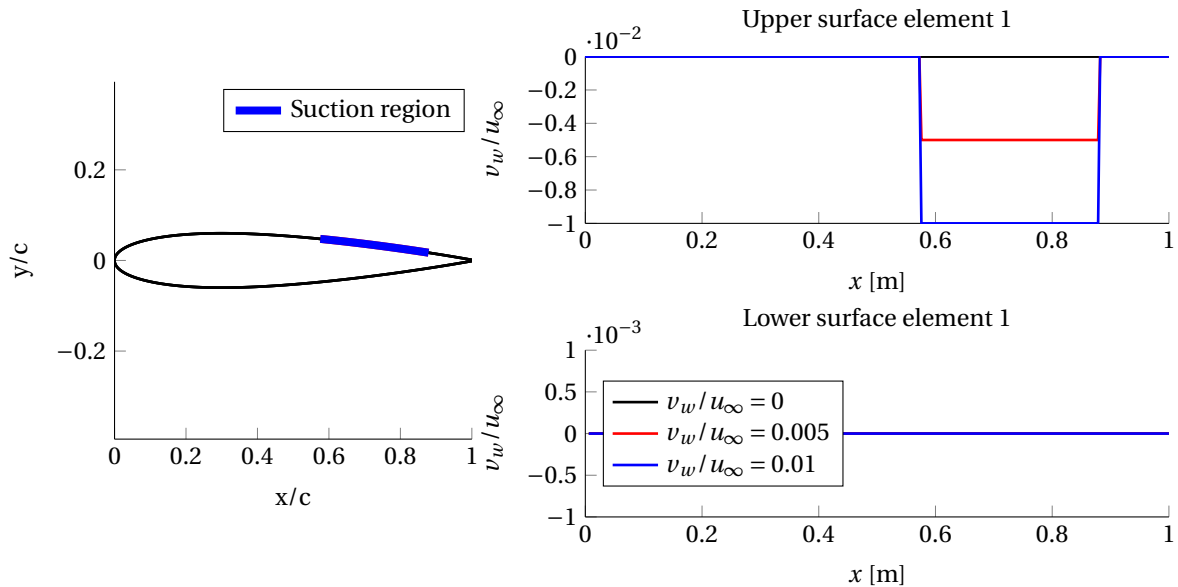


Figure 4.6: Suction location and distribution for comparison with rFoilsuc.

<sup>5</sup>MatSESuction contains several suction model options, one is to disable the displacement due to the missing mass flow.

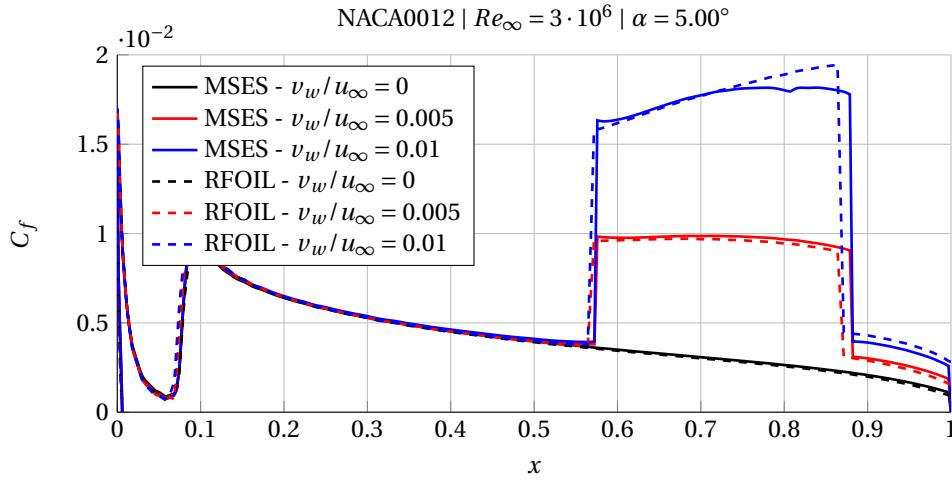


Figure 4.7: Comparison MatSESuction and rFoilsuc —  $C_f$ .

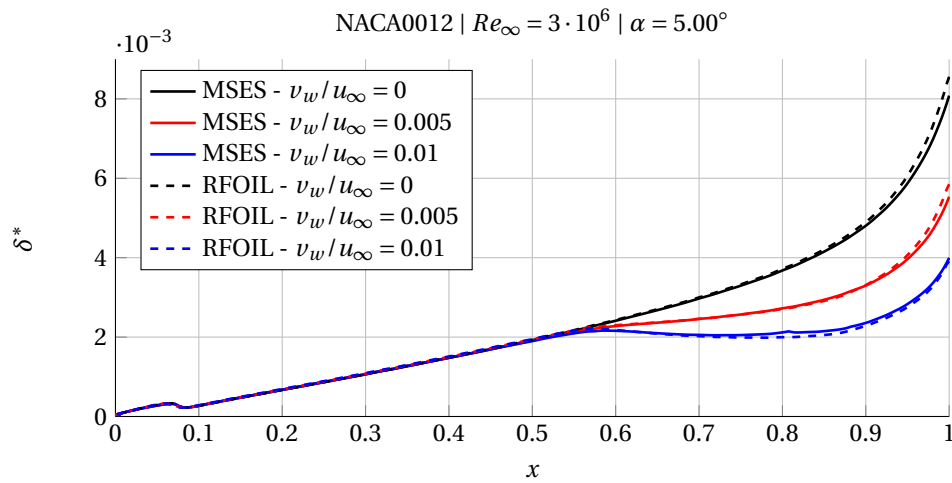


Figure 4.8: Comparison MatSESuction and rFoilsuc —  $\delta^*$ .

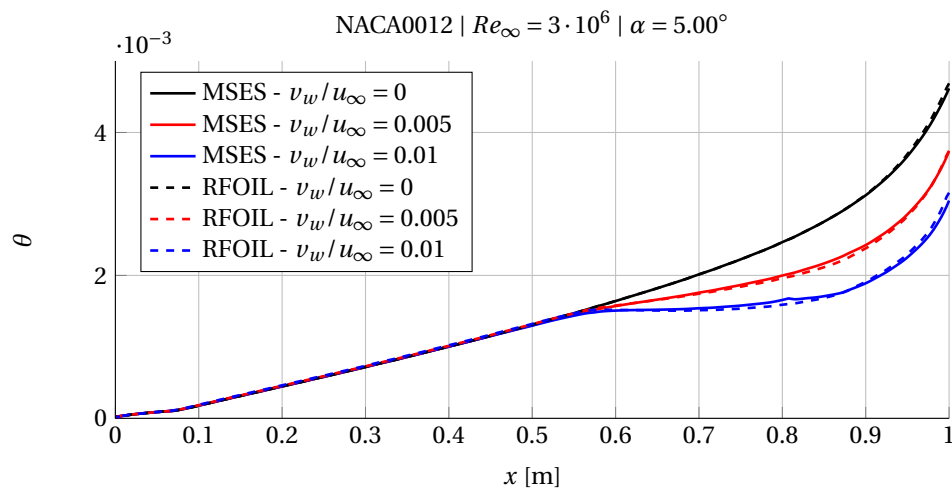


Figure 4.9: Comparison MatSESuction and rFoilsuc —  $\theta$ .

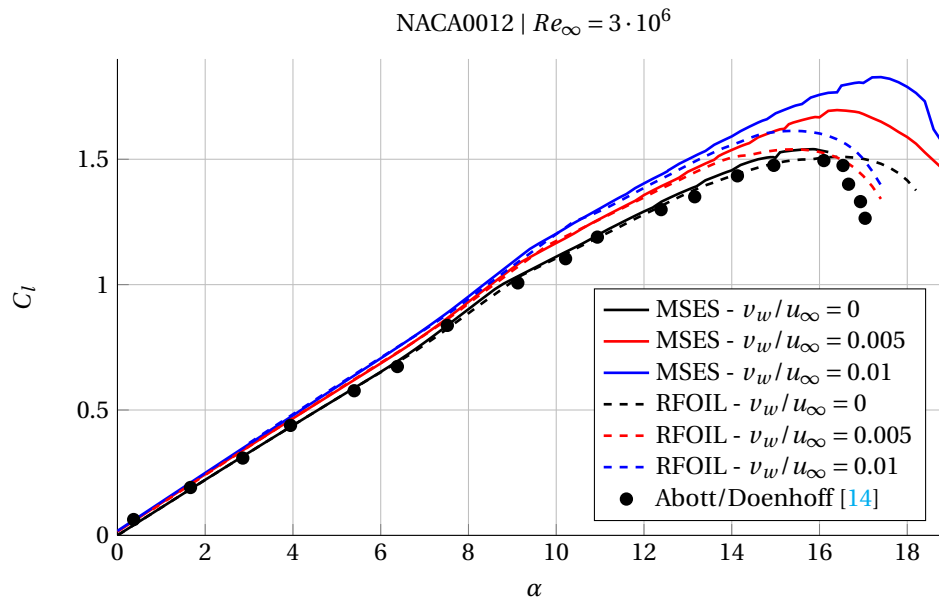


Figure 4.10: Comparison MatSESuction and rFoilsuc — Lift polar.

#### 4.4. CONCLUSION

Three validation cases have been discussed in this chapter: continuous suction over a flat plate, slot suction over a flat plate and a comparison with the rFoilsuc code. From these it can be concluded that the adaption of MSES for suction works well, except for two cases:

- Slot suction is notoriously more difficult to model, and this is also visible in the results of MatSESuction: unsurprisingly it fails to take into account the recirculation regions near the slot which results in an underprediction of  $\theta$ . The ‘outer flow’ does not seem to suffer much from this problem: the pressure distribution is in good agreement with the experiments. On the other hand, with  $\theta$  being off the danger arises that separation cannot be well predicted any more. Therefore it is recommended to not simulate very small suction areas with strong suction.
- The reliability of the flow prediction near  $C_{l_{max}}$  is unclear and varies from case to case. Therefore it is advisable to avoid using results near this area.

Since the goal of this project is to research the increase of lift the second point is somewhat regrettable. However, from a practical point can be remarked that a plane does not take off nor lands at an angle of attack that equals the maximum lift angle, but rather at a safer angle of attack that is lower. It is therefore still interesting to look at the gains in lift that can be achieved for somewhat ‘relaxed’ angles of attack.

# 5

## ROLE, IMPORTANCE AND ASSESSMENT OF THE WAKE

The starting point of this chapter is the base idea as put forward in the [introduction](#), therefore a very brief recap is appropriate at this point: the objective is to study boundary layer suction systems with minimal pump requirements aimed at increasing the lift coefficient on a multi-element airfoil.

Starting from the pump requirements, the [first section](#) discusses the reason why the wake is so interesting to investigate in the context of this project. To shed some light on how controlling the wake may benefit increasing the lift the [second section](#) gives some insight in the role of the wake in a multi-element airfoil system. The [last section](#) wraps this chapter up with a conclusion of the findings presented in the earlier sections.

### 5.1. THE ACTIVE PART IN A BLS SYSTEM: THE PUMP

What makes boundary layer suction truly an ‘active’ type of boundary layer control in the sense that it requires the external input of power is the presence of a pump in the system. This makes this pump a good starting point for looking at the possibilities to lower the requirements for the overall system, preferably up to the point where the requirements can be met by ‘naturally occurring energy potentials’. This is putting it somewhat abstractly: in practice we are looking for a pressure difference that is large enough to drive the boundary layer suction system without having to resort to external power input — thus effectively changing the system from ‘active’ back to passive. The power consumption of an ideal pump is given in equation (5.1): it is the product of volumetric flow rate of the fluid being pumped away ( $Q$ ) and the rise in total pressure ( $\Delta p_t$ ) that has to be overcome by the pumping system.

$$P_{pump} = Q \cdot \Delta p_t \quad (5.1)$$

Equation (5.1) provides a rational basis to identify the factors that influence the eventual power requirement for the BLS system, namely:

- The volumetric flow rate, or the amount of air being sucked away at the surface. A good measure for the total volumetric flow rate is given by the *overall suction coefficient*  $C_q$  (equation (5.2) shows that it is basically a non-dimensionalized version of the volumetric flow rate). The definition of the suction coefficient varies from source to source, but the convention used here is given by equation (5.2):

$$C_q = -\frac{1}{u_\infty \rho_\infty c} \int \rho_w v_w d\xi \quad (5.2)$$

The suction coefficient is usually used to compare BLS system requirements, and when it comes to the volumetric or mass flow rate this is correct. But as equation (5.1) reveals this does not tell the whole story, also the rise in total pressure that must be overcome is an equally important factor.

- The actual force required to do the work that must be delivered to move the volume of air  $Q$  in equation (5.1) is represented by the rise in total pressure  $\Delta p_t$  that must be overcome.

Let's focus on the second factor now. The rise in total pressure found in equation (5.1) can be further broken down into:

$$\Delta p_t = p_{out,t} - p_{in,t} + \Delta p_{loss} \quad (5.3)$$

The rise in total pressure is the difference between the total pressure at the outlet and the inlet, to which also the pressure drop or 'head loss' in the system must be added. Note that usually, i.e. in the case of an active pump, the total pressure at the outlet is higher than at the inlet. However, when a passive system is desired, the opposite is required so the term  $p_{out,t} - p_{in,t}$  becomes negative. If it is large enough it balances the pressure losses in the system and the net pumping power becomes zero: the work needed to drive the BLS system is now delivered by the pressure difference itself<sup>1</sup>.

Considering the no-slip condition at the suction surface the total pressure at the inlet is equal to the static pressure, and also for the total pressure at the outlet it is reasonable to make the same assumption at this point. So, in order for a 'passive suction' system, it is required that at least the static pressure at the outlet is lower than at the inlet<sup>2</sup>:

$$p_{out} < p_{in} \quad (5.4)$$

Also when the desire is only to minimize the pumping power the term  $(p_{out} - p_{in})$  must be minimized. Either way: it is desirable that the static pressure at the inlet — i.e. at the suction surface — is as high as possible.

Taking the above considerations into account brings the *suction location* into the picture. For an example one can look at virtually any pressure distribution (e.g. figure 2.8): static pressure is extremely low on the upper surface near the leading edge and rapidly becoming higher again towards the trailing edge where it tends to go to  $p_\infty$ . Also on the bottom surface the static pressure is high. So, it will be more difficult to find an underpressure low enough for air that is being sucked away from the upper surface near the leading edge — where the static pressure is already extremely low — then it will be to do the same thing for a suction location near the trailing edge or bottom surface. This consideration is especially important in the context of this work: as explained above the eventual aim is not to generate the required pressure difference  $\Delta p_t$  by means of installing a pump but by using a naturally occurring low pressure zone somewhere on the wing (or somewhere else on aircraft). This pressure will have to be at least lower than the static pressure at the suction location, and in practice a significant margin will be necessary to account for the head loss  $\Delta p_{loss}$  in the tubing system and over the suction sheet. With that in mind it is interesting to look for suction locations where the static pressure is not very low already, for example avoid to suck away air at suction peaks.

Of course, other factors than the power requirement of the pump influence the practical feasibility and the requirements of a BLS system: the added weight that the system brings with it, the added complexity which places a penalty on maintenance etc. Despite that, lowering the power requirement is still a good starting point for pursuing a low-requirement BLS system. Picking up again the discussion about suction location, it was already established that the bottom surface of the airfoil and the upper surface towards the trailing edge were interesting locations for suction with a BLS system with minimal requirements. But is there something to gain at these locations?

- Separation is very rare on the bottom surface, so applying suction here to avoid just that is not relevant. Running ahead of facts a little bit, it is also less interesting to apply suction here to control the thickness of the wake (see also [further](#)) since typically the thickness of the boundary layer at the trailing edge of the bottom surface is small compared to the one at the top.
- Contrary to what is the case for the bottom surface, applying suction at the trailing edge on the upper surface can be very effective against trailing edge separation. However, usually this requires large suction areas and/or strong suction; both resulting in large suction coefficients. From the viewpoint of designing a BLS system with requirements as low as possible this offsets the advantage of the location again.

So for an isolated airfoil the situation seems bleak to achieve a BLS system that puts low demands on both the suction location and suction coefficient (or amount of air that needs to be removed). But this investigation is concerned with multi-element airfoils and a lot more is happening here that influences the entire flowfield

<sup>1</sup>Compare this to the case of a *turbine*: going one step further than the present discussion, one can imagine the case where power is *extracted* from the system. In this case the absolute value of the difference  $p_{out,t} - p_{in,t}$  not only balances the pressure losses in the system, but exceeds it. The total pressure rise  $\Delta p_t$  in equation (5.1) now becomes negative as does the pump power: the pump now delivers power instead of requiring it and has become a turbine.

<sup>2</sup>Note that this statement also remains valid if the total pressure at the in- and/or outlet does not equal the static pressure.

(see also chapter 2). As was already hinted in the above discussion the wake thickness can be controlled by applying suction on the preceding airfoil surface. This in turn makes it possible to have some influence on the wake behaviour. The next section will discuss what wake behaviour is desired to maximize lift and how suction can help to achieve this.

## 5.2. WAKE FLOW IN A MULTI-ELEMENT AIRFOIL SYSTEM

In the previous section the importance of the wake in the context of this project has been outlined. In this section the wake will be further examined to identify the mechanisms that cause decambering of the multi-element airfoil system. Some of the elements of chapter 2 will also be revisited.

Figure 5.1 shows the different phenomena affecting the flowfield around a multi-element airfoil. As a continuation of the retarded flow in the boundary layers over the top and bottom of an element a wake is shed at the trailing edge of that element. Two different kinds of wake can be distinguished: ‘confluent shear layers’ (the merging wake of the slat and the BL of the main element is an example of this) where the shear layers are not divided by a region of potential flow. The other wakes visible are those of the main element and the flap: these are wakes that are still divided by a region of potential flow. An important thing to keep in mind is that only the second kind can be simulated with MSES; merging shear layers are not possible. This does not have to be a problem since this phenomenon is to be avoided to achieve an optimal configuration. In fact, much of the trouble of finding an optimum gap/overhang combination for multi-element airfoils is concerned with this problem: avoiding the merging of the shear layers. [16]

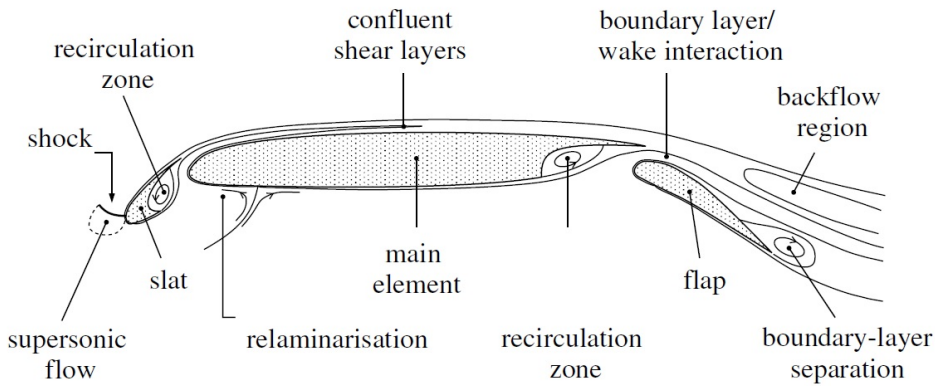


Figure 5.1: Phenomena influencing the flow over a multi-element airfoil. [12]

To get some insight in the development of the wake — be it in a multi-element flow configuration or not — it is useful to go back to the Reynolds averaged conservation equation for momentum in  $x$ -direction for turbulent boundary layer flow, which is equally valid for a wake<sup>3</sup>. This equation can then be used as a tool to explore the mechanisms that determine wake behaviour.

$$\underbrace{\bar{u} \frac{\partial \bar{u}}{\partial \xi} + \bar{v} \frac{\partial \bar{u}}{\partial \eta}}_{\text{Momentum transport (convection)}} + \underbrace{\frac{\partial \overline{u'v'}}{\partial \eta}}_{\text{Turbulent mixing of momentum}} = \underbrace{-\frac{1}{\rho} \frac{d\bar{p}}{d\xi}}_{\text{Pressure gradient}} + \underbrace{\nu \frac{\partial^2 \bar{u}}{\partial y^2}}_{\text{Viscous dissipation}} \quad (5.5)$$

Equation (5.5) shows the well-known balance of change in momentum on the LHS and the forces on the fluid elements on the RHS. The ‘turbulent mixing of momentum’-term is more commonly known as the ‘Reynolds stress’, but for the sake of the following discussion it is more clear to refer to it as an exchange of momentum due to the mixing action of the turbulent eddies — which it actually is(!). The term  $\nu \frac{\partial^2 \bar{u}}{\partial y^2}$  accounts for the turbulent dissipation. This phenomenon is dominant at the small scales, i.e. at the smallest turbulent eddies way down the *turbulent energy cascade* [59, 62], but not so much at the large turbulent structures that will be primarily focused on in the next discussions.

<sup>3</sup>The assumptions made here are: 2D-flow ( $\bar{w} = 0$  and  $\frac{\partial}{\partial z}$ ); the shear layer is ‘thin’ ( $\delta \ll x \rightarrow \bar{v} \ll \bar{u}$  and  $\frac{\partial}{\partial x} \ll \frac{\partial}{\partial y}$ ) [59]

In the case where there is no trailing element, the **pressure gradient** is practically **zero** throughout the course of the wake. Inside the wake viscous forces are dominant and smooth out the velocity defect of the wake. Also the turbulent eddies at the edges of the wake ‘pump’ extra momentum into the wake again, allowing it to decrease its overall momentum deficit. This results in a decrease of the displacement effect of the wake ( $\delta^*$ ) until it eventually vanishes. When this happens a state of full potential flow is reached again. Figure 5.2 summarizes this.

The presence of an **adverse pressure gradient** complicates the matter somewhat, this is the case in the presence of a trailing element (e.g. a flap). Figure 5.3 shows this situation. The viscous forces are still working to smooth out the velocity defect, causing the wake thickness ( $\delta$ ) to grow just like in the zero pressure gradient case. But if the adverse pressure gradient is strong enough, the velocity defect is deepened and the overall momentum deficit increases. One way to look at it is that to work against the increasing pressure momentum is ‘consumed’. This is reflected in equation (5.5): if the adverse pressure gradient is large, the LHS (i.e., the change in momentum of the flow particles) becomes negative. This in turn causes the displacement thickness to increase. This will happen rapidly near the moment where flow reversal occurs: no momentum is left and the pressure rise can only be compensated by quickly expanding the displacement of the wake. In contrast to the change in the magnitude of the velocity vector in the wake, the direction of it remains more or less unchanged. The majority of the increased turbulence originates at the edges of the wake, with virtually none being produced in the wake cores [30]. The next section discusses this in more detail.

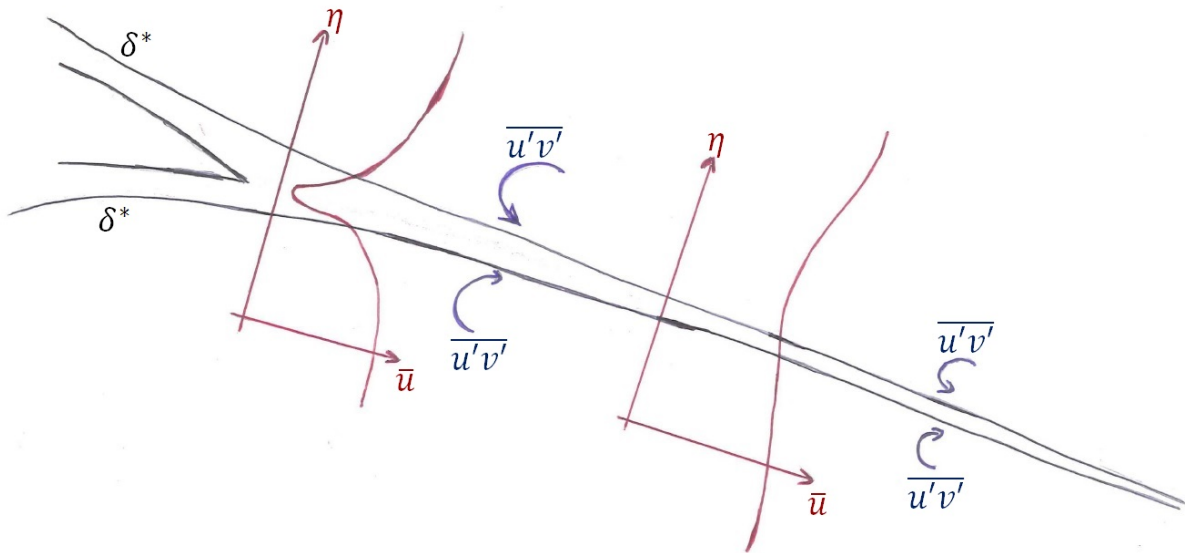


Figure 5.2: Wake in a zero pressure gradient: viscous forces inside the wake smooth out the velocity defect. Turbulent eddies at the wake edge pump extra momentum in the wake, which reduces the wake thickness until it eventually dies out.

### 5.2.1. WAKE IN AN ADVERSE PRESSURE GRADIENT

Smith notes the lack of research towards wake flow in an adverse pressure gradient in his classic paper on high-lift flow [16]. But the aeronautical research has come a long way since and now there is quite a large amount of literature available on the topic. However, the vast majority of this research is a comparison between experimental and computational results [12, 30, 63–69]. Since the computational simulation of strongly ‘separated’ regions is difficult these studies often only simulate only wakes in mild adverse pressure gradients [12, 64]. An exception to this is the study by Driver and Mateer: it presents results for adverse pressure high enough to create ‘massively separated regions’ — off-the-surface-separation, that is [63]. It is in this case that decambering of the entire flowfield is so strong that it causes a significant loss of lift.

Figures 5.4 – 5.6 show three cases with wake flow in a strong adverse pressure gradient, some streamlines are also shown in the background that make it easy to visualize the extent of the ‘separation bubble’. The

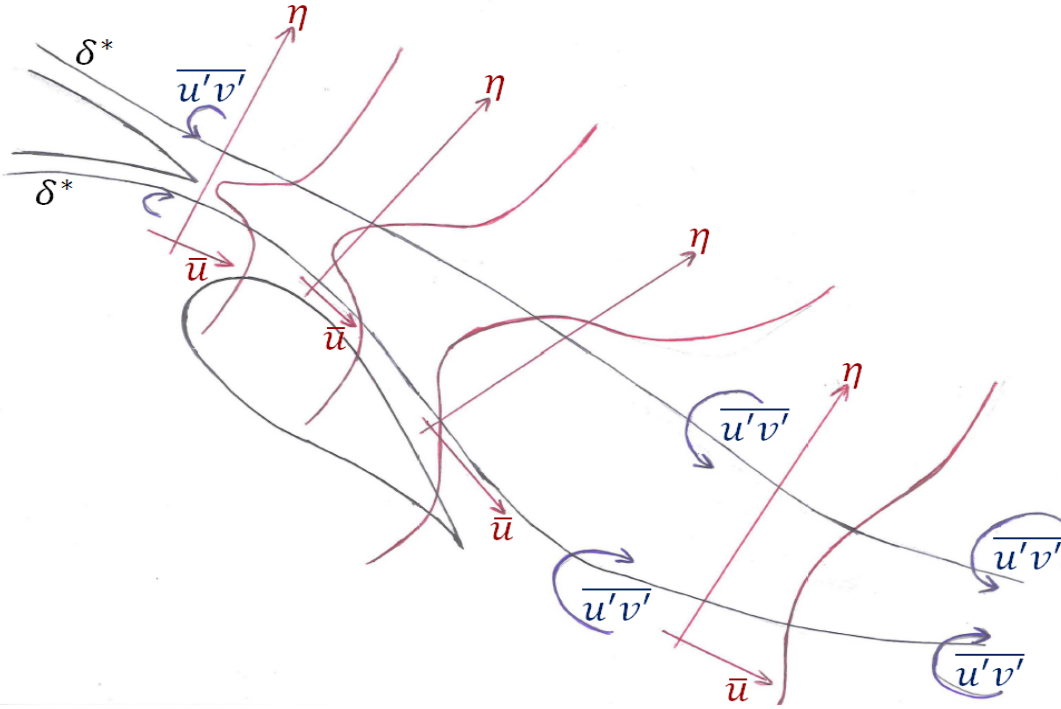


Figure 5.3: Wake in an adverse pressure gradient: viscous forces inside the wake smooth out the velocity defect, but the adverse pressure gradient causes the overall momentum deficit to grow. When all momentum is 'consumed' (near flow reversal) the only way the adverse pressure gradient can be balanced is with the turbulent mixing of momentum. The same mechanism eventually allows the wake to recover again (if no 'off-the-surface'-separation occurs earlier).

adverse pressure gradient is created by a diverging duct and the wake is shed from a flat plate ( $x = 0$  is the point where the plate ends and the wake starts). The first case shows no signs of flow reversal (referred to in the figures as 'separation'), for the second case mild flow reversal is visible and in the last case the separation area has expanded to a large area indicating 'massive separation'. Following the previous discussion, the viscous smoothing effect is clearly visible for all cases: the velocity profiles become wider and wider. However, due to the adverse pressure gradient, the maximum velocity defect does not decrease due to this action.

Comparing the pressure at the centerline of the wake for all three cases one can see that it remains the same for all cases (figure 5.7). In contrast, the wake displacement increases a lot with increasing adverse pressure gradients (figure 5.8): the wake can only sustain a certain pressure rise and compensates this by a rapidly expanding wake, resulting from a rapidly decelerating flow. Figure 5.8 shows how not only the displacement thickness of the wake increases with increasing pressure gradient, but also the rate at which this happens: the spreading rate of the displacement thickness is much higher for the case with massive separation. After this rapid increase of the displacement thickness tops off and decreases slowly again. It tops off once the flow is reversed (or reaches zero speed) in the wake. No momentum is left in the wake at this point. In equation (5.5) this means that momentum transport and viscous dissipation terms become negligible ( $\bar{u} \approx 0$  and  $\bar{v} = 0$ ). The pressure gradient and turbulent mixing terms become dominant and scale directly with each other:

$$\frac{\partial \overline{u'v'}}{\partial \eta} \approx -\frac{1}{\rho} \frac{dp}{d\xi}$$

Depending on the amount of turbulent mixing, a further (limited) pressure rise inside the wake can be sustained by 'pumping' momentum into the decelerated wake by means of highly energized turbulent eddies, this is also visible in figure 5.7. The same mechanism also helps to eventually increase the overall momentum contained in the wake enough to accelerate the wake again and decrease the velocity deficit. This in turn allows the displacement of the wake to decrease again; which is also visible in figure 5.8. Figures 5.10 and 5.9 shows the maximum value of  $-\overline{u'v'}$  and  $-\frac{\partial \overline{u'v'}}{\partial \eta}$  respectively: while the maximum value of  $-\overline{u'v'}$  is much higher for strong flow reversal, the gradient remains the same: this is again the result of the spreading of the wake. The higher turbulent mixing is the result of a larger area in which it grows rather than a steeper gradient.

The previous discussion is based on results for a symmetric wake without curvature. However several researchers report that curved and/or asymmetric wakes generally tend to be better at withstanding an adverse pressure gradient and an asymmetric wake tends to become symmetric fairly rapidly [63, 65–67]. For the degree of asymmetry and curvature that is encountered in this project the behaviour of the wake is assumed to be in line with the above discussion for symmetric, uncurved wakes.

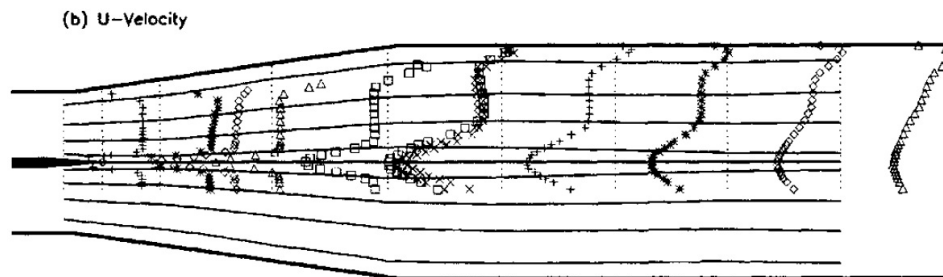


Figure 5.4: Wake in adverse pressure gradient: non separated case streamlines and velocity profiles. [63]

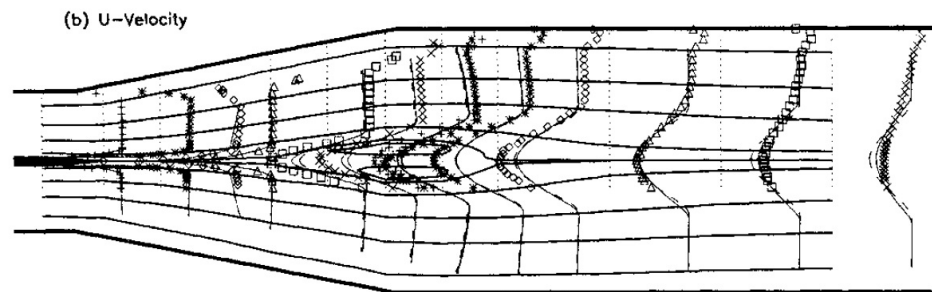


Figure 5.5: Wake in adverse pressure gradient: mildly separated case streamlines and velocity profiles. [63]

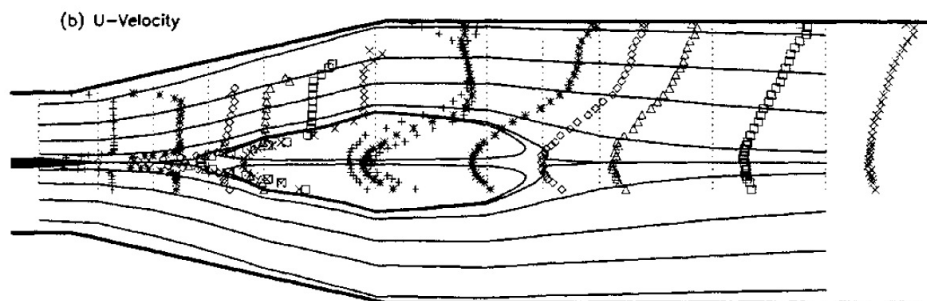


Figure 5.6: Wake in adverse pressure gradient: massively separated case streamlines and velocity profiles. [63]

### 5.2.2. WAKE BURST: A QUESTION OF SEMANTICS?

*Wake burst* and *off-the-surface-separation* are terms often found in literature to describe a change in the behaviour of the wake, more specifically to describe a situation arises where the wake becomes a dominant feature of the flowfield. The term however is somewhat unclear since there is no clear definition for it. To begin with, the term ‘burst’ implies a sudden change which is certainly not always the case — just like ‘ordinary’ BL separation does not necessarily has to happen instantaneously. As is clear by now, a formal definition is lacking, let alone that a criterion is available to identify it. Despite that wake burst can be characterized as a viscous phenomenon with [15, 16, 30, 63, 65, 66, 70]:

- rapid wake thickening;
- flow deceleration and possibly flow reversal in the wake;

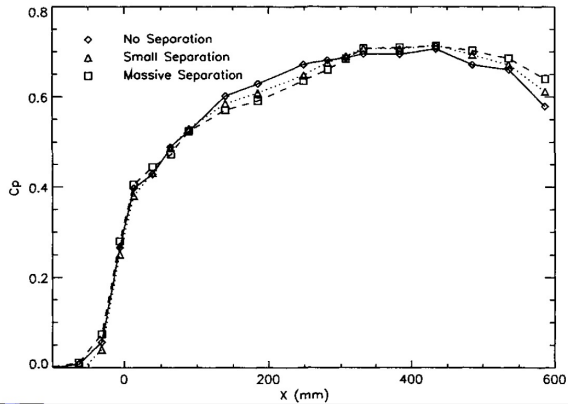


Figure 5.7: Wake in adverse pressure gradient: pressure along centerline. [63]

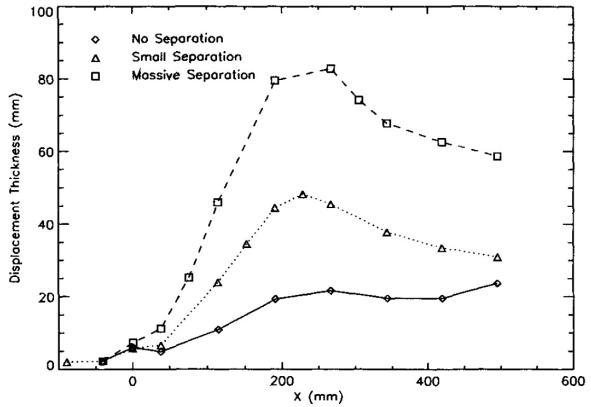


Figure 5.8: Wake in adverse pressure gradient: displacement thickness. [63]

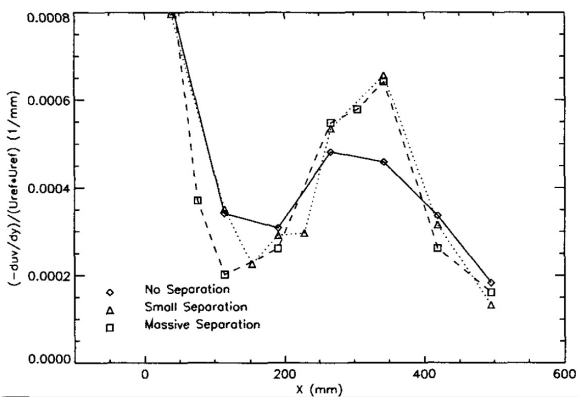


Figure 5.9: Wake in adverse pressure gradient:  $-\frac{\partial u'}{\partial y}$ . [63]

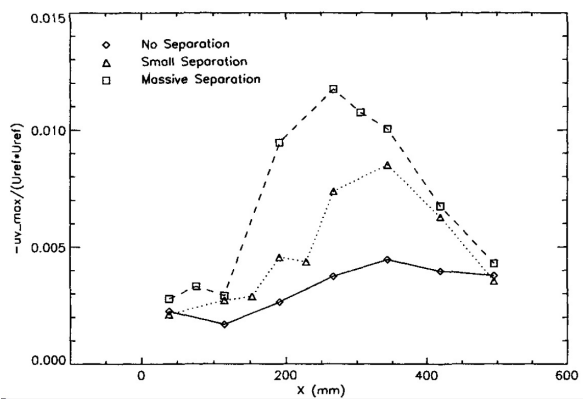


Figure 5.10: Wake in adverse pressure gradient:  $(-u'v')_{max}$ . [63]

- increased turbulence in the wake.

The consequences of the ‘wake burst’ are:

- increased drag;
- reduction of  $C_{l_{max}}$ ;
- and — more generally — a decambering of the airfoil system, with an associated loss in lift.

In the context of the present work the last point is of most interest. When the term ‘wake burst’ is used, it will refer to a state of the wake where it has become a dominant feature of the flowfield and responsible for a loss of lift of the overall airfoil system. It will answer to the characteristics and consequences given above. However, it will in general not refer to a phenomenon occurring very ‘sudden’, nor does it necessarily mean that there is actual flow reversal (although in practice this is usually the case, as should be apparent from the discussion in section 5.2.1). Concerning this last point, note that MSES uses an integral boundary layer formulation, so having information about the actual velocity profile (and the existence of flow reversal) can only be based on a reconstruction based on the integral BL parameters. If it is at all possible to reliably identify wake burst directly based on integral parameters this is much preferred, since in that case no additional assumptions have to be made. This is the subject of the next section.

### 5.3. ASSESSMENT OF THE WAKE

As should be apparent from the [previous section](#) it is important to realize that just the appearance of (mild) flow reversal or the mark of ‘wake burst’ does not also means that there is an immediate loss of lift associated with it. Conversely, and even more so, a loss of lift does not mean that the wake is causing it. Indeed, in most cases the loss in lift can be attributed to ‘ordinary’ causes such as boundary layer separation. What is necessary here is a reliable indicator that can be used to identify the wake as being such a dominant feature of the flow field that it causes decambering of the airfoil system and an associated loss of lift.

In section 5.3.1 some attention is given to Gartshore’s criterion. Although it is not suitable to predict wake burst it is still interesting to give some attention to it because it gives a simple relation that incorporates the viscous and pressure gradient aspects. Section 5.3.2 explores the possibilities to detect wake burst — in the sense that the wake starts compromising lift performance (see also section 5.2.2).

#### 5.3.1. GARTSHORE’S CRITERION

Gartshore’s criterion was already introduced in section 2.1.5. It is a criterion to determine whether a wake is growing or decaying, based on the earlier discussed observation that an adverse pressure gradient aggravates the momentum deficit and the viscous effect smooths it out [17]:

$$\frac{1}{1 - C_p} \frac{dC_p}{dx} > \frac{0.007}{\delta^*} \quad (5.6)$$

If the left-hand side of equation (5.6) is less than  $\frac{0.007}{\delta^*}$ , the wake decays; if greater, it grows. It is interesting to compare some results of MatSESuction to the criterion of Gartshore. With the capabilities of MatSESuction the growth rate of the displacement thickness can be quickly calculated for each point, but it is still interesting to give some attention to the old criterion put forward by Gartshore because it gives some insight in the behaviour of the wake. Moreover, it relates the wake growth to a quantity that can directly be influenced by suction, namely  $\delta^*$ . Equation (5.6) shows that by lowering  $\delta^*$  — for example by suction — the adverse pressure gradient can be higher while still avoiding growth of the wake. This is behaviour that can be expected since it is well known that thinner shear layers can withstand larger adverse pressure gradients, but the criterion also quantifies this. As thoroughly discussed in section 5.2 the growth of the displacement of the wake is very much related to a loss of momentum, increase in turbulence and eventual wake burst. If the results of MatSESuction are in line with Gartshore’s criterion, this is an indication<sup>4</sup> that MatSESuction is indeed able to simulate the wake and its behaviour that is sought to be controlled by suction.

Figures 5.11–5.13 show the development of Gartshore’s criterion for the wakes of the NLR7301 airfoil with three different flap deflections. On the left the geometry and (first inviscid) streamlines are shown; the red band indicates boundary layer growth following Gartshore and the black band shows where there is actual

<sup>4</sup>Not definitive proof though.

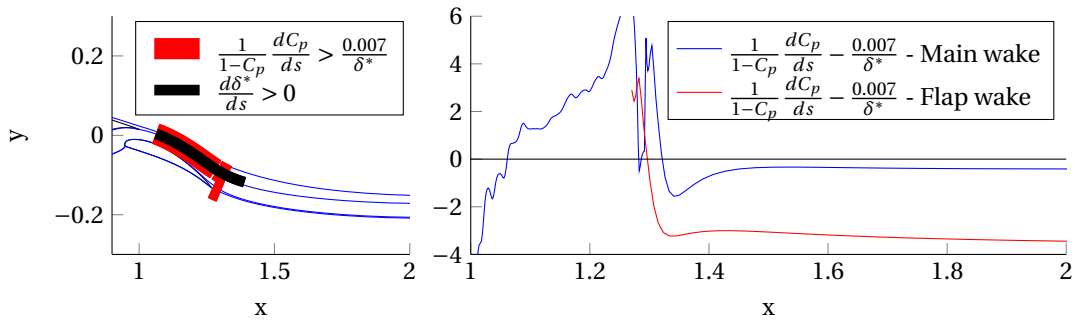


Figure 5.11: Wake growth: comparison Gartshore's criterion and MatSESuction — NLR7301 —  $\delta_f = 20^\circ$ .

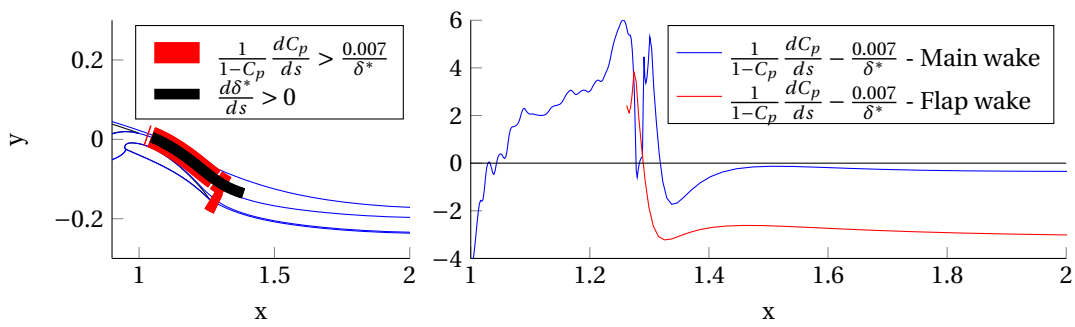


Figure 5.12: Wake growth: comparison Gartshore's criterion and MatSESuction — NLR7301 —  $\delta_f = 24^\circ$ .

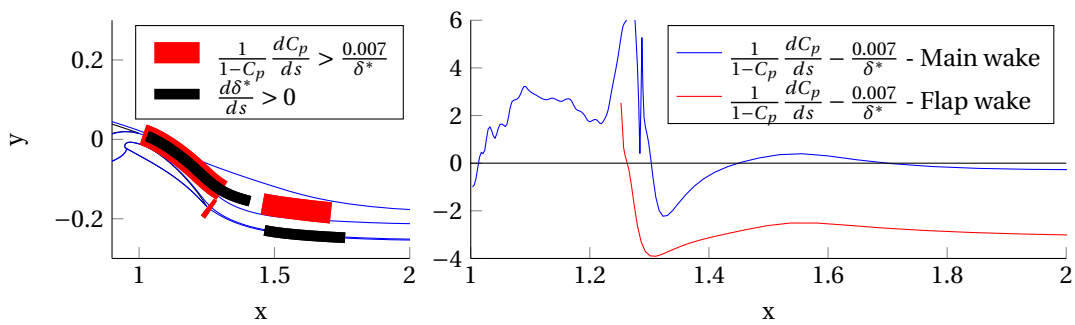


Figure 5.13: Wake growth: comparison Gartshore's criterion and MatSESuction — NLR7301 —  $\delta_f = 28^\circ$ .

boundary layer growth. On the right the value of the criterion is shown along the trajectory of the wake (where it drops below zero there is wake growth). For the case  $\delta_f = 28^\circ$  a large area of wake growth is predicted by Gartshore in the wake of the main element past the flap, however, on the right can be seen that the criterion actually only marginally exceeds zero. This shows immediately one of the drawbacks of the criterion: while it may indicate wake growth, it does definitely not give very reliable information about the severity of it. The opposite is true for the wake of the flap: an area with wake growth is present that is not being picked up by Gartshore's criterion; it should be said however that the wake growth is very, very small here.

It is important to keep in mind that the criterion was actually developed from and for flow in the adverse pressure gradient over a flap; so further downstream it is probably not a valid model. In the region above the flap the results from Gartshore's criterion follow the actual situation very well for all cases. All in all, the results of MatSESuction are reasonably well in line with Gartshore's criterion. This strengthens the credibility of its predictive capabilities with respect to the wake's behaviour.

### 5.3.2. WAKE BURST DETECTION

To determine to which extent the wake is burst, several options can be explored based on the knowledge of the characteristics (section 5.2.2) and development of the wake (section 5.2):

- Pomeroy and Selig use a figure of merit analogous to the wake thickness  $\delta$  for mutual comparison of similar flow cases [70]. The figure of merit is the normal distance at a given streamwise station between the two points where the 'total pressure coefficient'  $C_{p_t} = \frac{p_t - p_\infty}{q_\infty}$  reaches a certain threshold value ( $-0.10$  in the case of [70]). As they remark themselves in the paper the threshold value is rather arbitrary and taking it at  $C_{p_t} = 0$  would give the actual wake thickness  $\delta$ .
- From the discussion in section 5.2.1 and from figure 5.8 can be learned that the severity of wake burst is characterized by the displacement effect of the wake  $\delta^*$ .
- Other integral parameters such as the momentum thickness  $\theta$  and the derived shape factor  $H$ .
- From the discussion in section 5.2.1 it was also clear that the severity of wake burst is strongly linked to the *spreading rate* of the wake:  $\frac{\partial \delta^*}{\partial s}$ .
- Other possibilities include analysis of the velocity profiles and the turbulence intensity.

All these options are candidates to detect wake burst but they are not all equally suitable, also because some of the limitations of MatSESuction.

The first two options are the wake thickness  $\delta$  and displacement thickness  $\delta^*$ . To begin with it are dimensional numbers, so comparing between two quite geometrically different cases would not give a lot of useful information. This could of course be overcome by non-dimensionalizing them by some relevant reference length (e.g. the chord length). But even then the wake thickness at a certain streamwise station is heavily dependant upon the upstream history of the wake and boundary layer: for example, an earlier transition far upstream could just as well cause a thicker wake thickness in the wake as wake burst itself. The same is true for the momentum thickness  $\theta$ . It follows that these are not prime choices to reliably identify wake burst. The shape factor is very attractive option: it is a dimensionless number that is already commonly used to detect separation of 'ordinary' boundary layers, with great success. There is no specific reason why this line of reasoning could not be extended for it to give an indication about the condition of the wake. However, there is virtually no literature or even data available that documents the development of the shape factor in the wake. It can be expected that wake burst will cause the shape factor to peak, but to have a quantification of what values of  $H$  are indicative for this, experimental or other data — from outside this project — is lacking.

This is not the case for the displacement thickness. Ample data is available for this parameter since it is often used to compare experimental with numerical data (see also section 5.2.1). It is already discussed why the displacement thickness itself is an interesting parameter but not a good choice to use as a criterion, but the *rate* at which it grows is an equally — if not even more — interesting parameter. At the onset of wake burst, the displacement effect of the wake will rapidly increase as explained in section 5.2.1. It is also a dimensionless number which makes it easy to use it for different flow cases, and it is often discussed in literature so the envisaged criterion can have a solid foundation on experimental data. The study by Driver and Mateer very conveniently presents three cases with no, mild and strong flow reversal [63]. Before the onset of flow reversal, an almost linear increase in the displacement thickness can be observed for all three

cases, see figure 5.8. This allows to extract a constant spreading rate of the displacement thickness and link this spreading rate to a flow case (either no, small or massive flow reversal; this is shown in figure 5.14):

$$\text{No flow reversal: } \frac{d\delta^*}{dx} = 0.0395 \quad (5.7a)$$

$$\text{Mild flow reversal: } \frac{d\delta^*}{dx} = 0.2244 \quad (5.7b)$$

$$\text{Massive flow reversal: } \frac{d\delta^*}{dx} = 0.4451 \quad (5.7c)$$

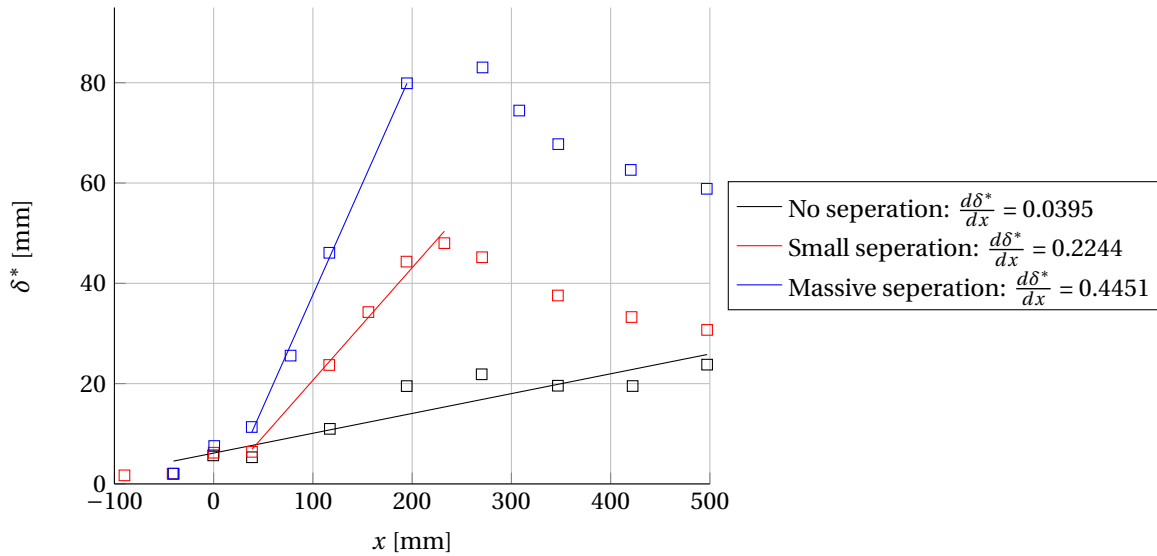


Figure 5.14: Displacement thickness spatial growth rates extracted from Driver and Mateer [63].

For the sake of completeness the option of analysing the velocity profile and turbulence in the wake is also discussed. An analysis of the velocity profiles or turbulence intensity throughout the wake would probably give even better information than the spreading rate about the extent to which the wake is burst, but the integral boundary layer formulation of MatSESuction does not produce this kind of information. A work-around for this can be employed with a reconstruction of the velocity profile and the turbulence intensity with models based on integral parameters. However, for wakes these models are very unreliable or even non-existent respectively. Indeed, the author experimented with this approach before adopting the spreading rate of the wake as a criterion but without a lot of success. The author therefore feels that it is better to have a criterion based directly on the integral parameters. Using the work-around of a reconstruction of the velocity profile will at best give equally reliable results, and in practice almost always much worse.

What rests is to check whether the spreading rate of the displacement thickness  $\frac{d\delta^*}{ds}$  is useful to use in conjunction with MatSESuction. Are the limiting values of  $\frac{d\delta^*}{ds}$  in equations (5.7) reflected in the results obtained with MSES/MatSESuction? To answer this question a relevant case is presented in figure 5.15: the NLR7301 airfoil (without suction) at an angle of attack of  $\alpha = 8^\circ$ . Figure 5.15a shows the variation of the lift coefficient with increasing flap deflection. A clear deviation from the trend is visible when the flap deflection is increased past  $\delta_f = 24^\circ$ . This indicates that some sort of disturbance manifests itself in the flowfield for  $\delta_f > 24^\circ$ , but judging from the shape factor development in the BLs it is not surface separation or a separation bubble (not shown), and also the transition point does not move a lot. Could it be that the disturbance must be attributed to the wake? Judging from figure 5.15b this is probably the case: for flap deflections below  $24^\circ$  the spreading rate peaks at values below the value for which Driver and Mateer only found mild flow reversal (which is at  $\frac{d\delta^*}{ds} = 0.2244$ ). For larger flap deflections the peak value of the spreading rate quickly increases, and even reaches the value for which Driver and Mateer report massive flow reversal. Figures 5.15c and 5.15d show the effect of the displacement of the wake and also serve to support the statement that the loss in lift cannot be attributed to separation or transition. From this and other cases (for more cases one can see chapter 6) it can be concluded that the proposal to use the spreading rate of the wake  $\frac{d\delta^*}{ds}$  to detect wake burst works well and

also that it is an excellent method to use in conjunction with MatSESuction. Even better, the value for which Driver and Mateer find mild flow reversal ( $\frac{d\delta^*}{ds} \approx 0.23$ ) proves to be a good threshold value above which wake burst is likely.

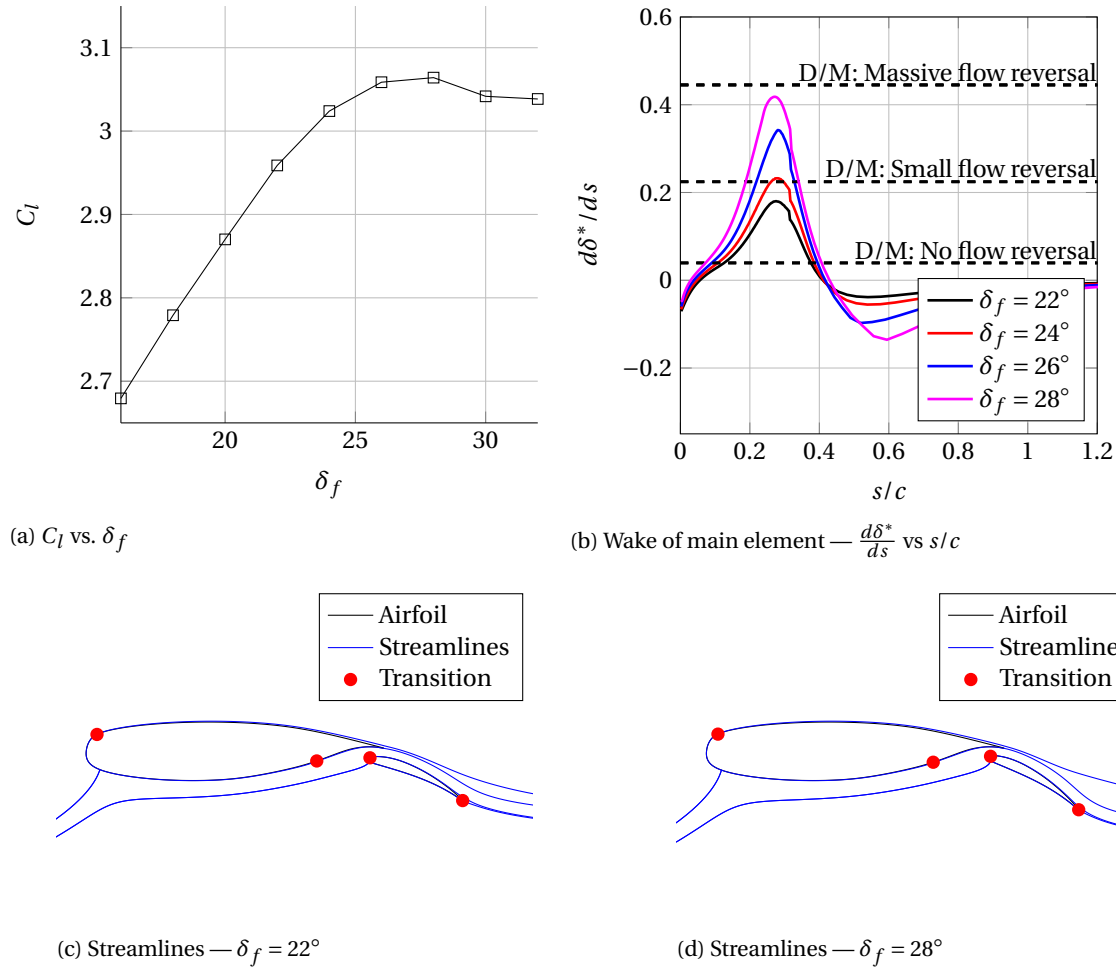


Figure 5.15: NLR7301 — No Suction —  $\alpha = 8^\circ$ . Comparison of the wake growth ( $\frac{d\delta^*}{ds}$ ) with the critical values for flow reversal from [63] show that  $\frac{d\delta^*}{ds}$  is a reliable indicator (to be used in conjunction with MatSESuction) for flow reversal in the wake that leads to a loss of lift.

## 5.4. CONCLUSION

This chapter started with the equation of an ideal pump, as a means to identify the factors that make up the requirements of a BLS system. It turns out two factors can be distinguished: the suction *quantity* and the *pressure* at the suction location. The former is much related to the suction strength an area over which suction is necessary. A good measure for it is the suction coefficient  $C_q$ , which is virtually the only measure for suction requirements in literature. The total pressure rise on the other hand dictates that it is desirable to apply suction where the static pressure is relatively high; this is much related to the suction location. It was reasoned that the best option to achieve a BLS system with low requirements is to try to influence the wake by applying suction near the trailing edge.

This is an interesting option in multi-element airfoil configurations. The wake encounters an adverse pressure gradient in this case which can cause the flow in the wake to lose a lot of momentum. This leads to a rapid thickening of the wake and possibly even flow reversal. This can affect the flowfield to such an extent that a significant loss of lift can be observed that can be attributed to the behaviour of the wake: a situation that will be referred to as ‘wake burst’. Suction can delay this wake burst by making the boundary layer thinner before it is shed as a wake at the trailing edge.

Since the term ‘wake burst’ lacks a clear definition, let alone a means to identify it with quantifiable parameters, it can be difficult to point at it as the ‘culprit’ for a loss of lift. To remedy this situation the spreading rate of the displacement thickness  $\frac{d\delta^*}{d\xi}$  is proposed to use as a criterion. From a theoretical perspective, rapid spreading of the wake is known to be strongly linked to wake burst. It is also a dimensionless number so it can be used independent of geometry. Because the displacement thickness is often presented in literature the criterion does not have to be based on the own simulations in MatSESuction but can instead have a solid foundation on experimental data. This criterion also shows to work really well with the results of MatSESuction, consistently indicating wake burst where a loss of lift is observed — which is, after all, the main concern — yet surface separation is not present. It is therefore concluded that  $\frac{d\delta^*}{d\xi}$  can be used as a reliable indicator for wake burst:

The **onset of wake burst** can be expected when:

$$\boxed{0.23 < \frac{d\delta^*}{d\xi} < 0.44} \quad (5.8)$$



# 6

## BLS CONFIGURATIONS WITH MINIMAL PUMP REQUIREMENTS FOR MULTI-ELEMENT AIRFOILS

In the [previous chapter](#) was concluded that the most promising approach to achieve a BLS system with minimal pump requirements is to try to influence the wake to avoid wake burst. This will be the focus of the investigation presented in this chapter, which contains the results of the simulations with MatSESuction of suction applied to the NLR7301 and MFFS026 multi-element airfoils.

### 6.1. NLR7301

The NLR7301 is a very grateful test geometry: it has been specifically designed so no flow separation occurs at the wing shroud/flap cove/flap well. This makes it possible to study the behaviour of the wake, of transition models, of turbulence models etc. applied to multi-element airfoils without having to worry about the unwanted influence of the separation at the flap well. It is no surprise then that it is also often found in literature as a validation case or the study object.

Also for this project it is important that flow separation is avoided at the flap well, because this is not the interest of this study. Therefore it is desired to minimize the influence of it. The NLR7301 is perfectly suited for this and an excellent starting point for the discussion of the results.

#### 6.1.1. COMPARISON WITH EXPERIMENT

Before discussing the effect of boundary layer suction on NLR7301 airfoil it is not a bad idea to compare some experimental results with the results from MatSESuction, this is of course without boundary layer suction. This will give an indication of the reliability of the prediction from MatSESuction that can be expected. The experimental results for the NLR7301 were obtained by van den Berg and Oskam in the low speed wind tunnel of the NLR [71]. The experiments were performed on a model with chord  $c = 0.57$  m and at a Reynolds number of  $Re_c = 2.51 \cdot 10^6$  and Mach number  $M = 0.185$ . The airfoil geometry is shown in figure 6.1.

In section 5.3.2 it was explained how the behaviour of the wake (and the severity of the wake burst in particular) is best assessed with the available means: the combination of a change in the trend of the lift and the growth rate of the displacement thickness are key in this. The experimental data available from [71] allows to compare these values at an angle of attack of  $\alpha = 6^\circ$ . Figure 6.2 shows the lift polar and figure 6.3 the development of  $\delta^*$  and  $\theta$  in the wake of the main element; these experimental values were not available directly but were obtained by digitalizing the velocity profiles of the wake given in [71] and integrating them. Despite that the agreement is good: the decrease of  $\delta^*$  over the part of the flap where there is a favourable pressure gradient and the sharp rise in the presence of an adverse pressure gradient is well predicted (pressure distribution of the flap is shown on the left in figure 6.4); only at the extremes the displacement thickness remains somewhat underpredicted. Also the momentum thickness shows good agreement, except for the last point at  $x = 1.4$ : here the momentum thickness is very far off. The reason for this is not entirely clear, but it is suspected that interaction of the wakes plays a role here, which is not predicted by MatSESuction. The

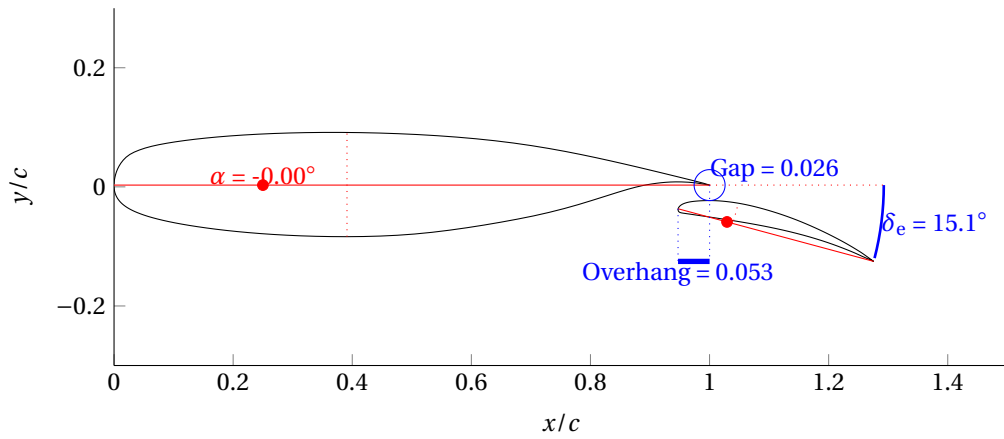


Figure 6.1: NLR7301 airfoil geometry.

predicted lift polar in figure 6.2 shows close agreement with the experiment but fails to accurately predict  $C_l$  at angles of attack close to  $\alpha_{C_{l_{max}}}$ . It was already discussed in chapter 4 that MSES has difficulties near  $C_{l_{max}}$ ; in this case the extremely sharp drop in lift after  $C_{l_{max}}$  observed in the experiment makes this case extra difficult. The pressure distribution over the flap at two angles of attack ( $6^\circ$  and  $13.1^\circ$ ) is compared in figure 6.4. At an angle of attack of  $6^\circ$  the prediction is very good, but closer to  $\alpha_{C_{l_{max}}}$  the pressure distribution over the upper surface is off; this can also be seen in the lift polar. Also the inviscid result is shown for comparison: it is clear that the viscous effects play an important role in the eventual lift distribution. Not only the boundary layer over the flap is responsible for this but also the wake of the main element has a large — although indirect — influence on it.

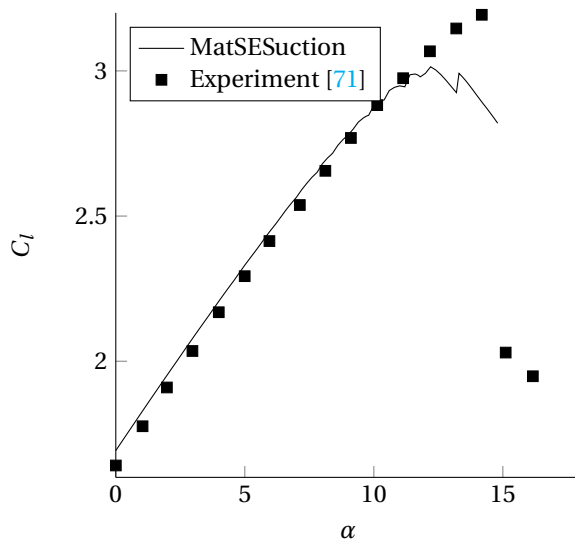
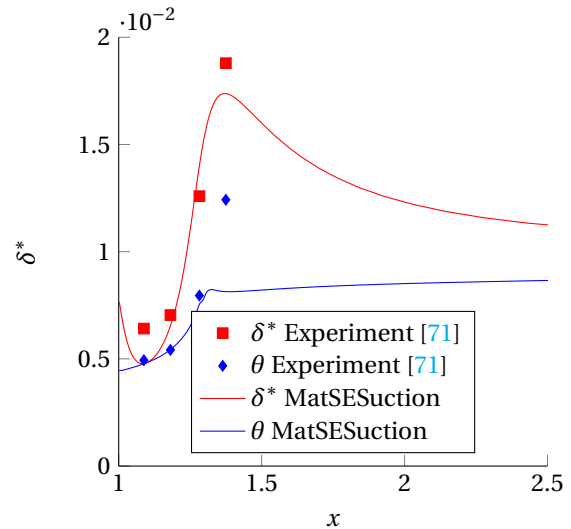


Figure 6.2: NLR7301 case — Comparison of lift polars.

Figure 6.3: NLR7301 case — Comparison of  $\delta^*$  and  $\theta$  in the main element wake —  $\alpha = 6^\circ$ 

### 6.1.2. NLR7301 WITH SUCTION

The NLR7301 case was already introduced in chapter 5. Figure 5.15a shows that at an angle of attack of  $8^\circ$  there is a change in the trend of the lift for flap deflections above  $\delta_f = 24^\circ$ . The spreading rate of the displacement thickness (figure 5.15b) indicates that the source of the problem is located in the wake: strong flow reversal is present here, or this is at least expected when comparing the spreading rate of  $\delta^*$  with the critical values found from [63]. The loss in lift cannot be attributed to surface separation: from figure 6.8 it is clear that the shape factor over the upper surfaces of the main element and flap never reach critical values (black line; the lower surfaces are not shown, nothing interesting is going on here); except at the trailing edge

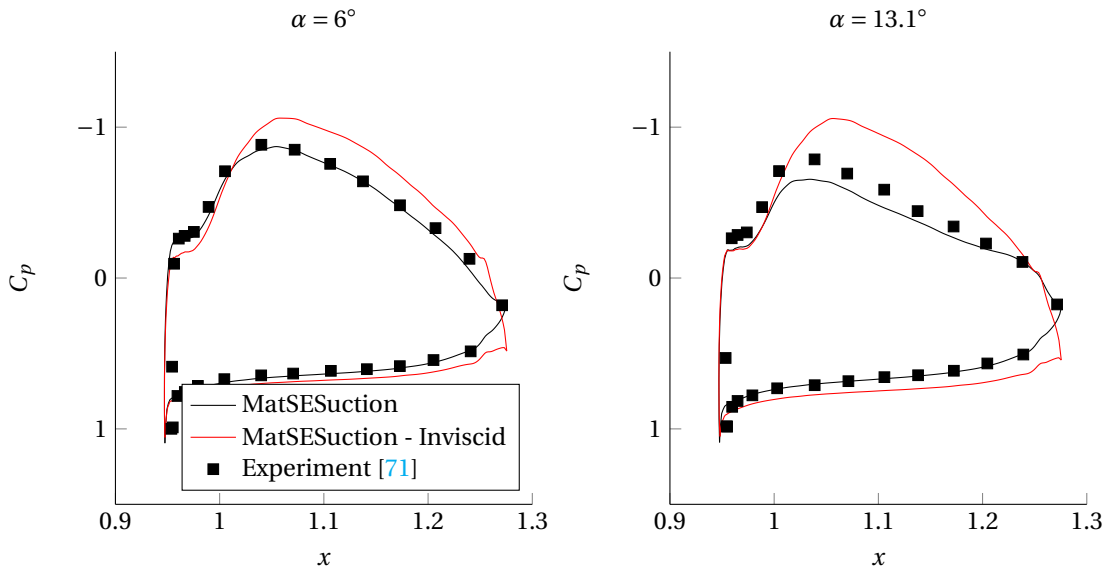


Figure 6.4: NLR7301 case — Comparison of pressure distribution over flap at selected angles of attack.

of the flap the onset of TE separation is visible. The large peak in  $H$  on the upper surface of the main element near the leading edge is a separation bubble that is also observed in the experiment by van den Berg and Oskam.

The question is now whether the observed wake burst can be avoided by suction. Suction was applied near the trailing edge from  $x/c = 0.81$  to  $x/c = 0.91$  with a strength of  $v_w/u_\infty = -0.01$ . This amounts to a suction coefficient of  $C_q = -0.001$ . Other values for  $v_w/u_\infty$  were also simulated, some of which are discussed later, but for now the focus will be on the difference with the non-suction case. To this end and to keep things clear, the focus will be on three configurations: two without suction and with the flap deflection at  $24^\circ$  and  $28^\circ$  respectively and one with suction, also with the flap deflection at  $28^\circ$ . Figure 6.5 shows the effect on the spreading rate of the displacement thickness for the three configurations, the critical values for wake burst are also indicated. The choice to show  $\frac{d\delta^*}{ds}$  plotted against  $x$  instead of  $s$  may at first seem somewhat confusing, but this is deliberately done to make it possible to make comparison with the actual geometry easier (figure 6.1). For a flap deflection of  $24^\circ$  and no suction the spreading rate of  $\delta^*$  indicates that the wake is on the verge of bursting, but hasn't yet. No loss of lift is consequently observed in figure 6.7<sup>1</sup>. For  $\delta_f = 28^\circ$  the critical value for  $\frac{d\delta^*}{ds}$  has been well exceeded. This is also translated in the fact lift tops off for this flap deflection. Applying suction prevents the strong growth of the displacement thickness as is clear from figure 6.5. This also leads to a significant gain in lift: at a flap deflection of  $28^\circ$  the lift coefficient is increased from 3.064 to 3.196, or an increase of 4.31%. The lift also tops off at a somewhat higher flap deflection (at  $\delta_f = 30^\circ$ ); at this flap deflection the spreading rate of  $\delta^*$  is again well into the 'danger zone' (where  $0.23 < \frac{d\delta^*}{ds} < 0.44$ ). From figure 6.8 it is clear that suction is also very effective against lowering the peak of  $H$  in the wake (middle plot). The development of  $H$  observed in this plot suggests that also  $H$  could be used as a criterion to identify wake burst as already put forward in section 5.3.2; the critical value would be around  $H = 5$  but this is speculating somewhat because little is known yet about the development of  $H$  in the wake. The pressure distribution for the three cases is shown in figure 6.6: an increase in circulation over the whole airfoil system is visible, both for increasing the flap deflection but also when wake burst is prevented at the TE. The 'dumping velocity' is also increased (see section 2.1.3). To end this discussion, a more visual approach to show the effect of suction is presented in figure 6.9: it shows the first inviscid streamlines around the airfoil. It is clearly visible that the suction limits the wake growth and increases the overall circulation. Also indicated are transition and separation locations (at the TE means that there is no actual separation) and the suction location (thick blue band on upper main element surface).

<sup>1</sup>Notice how sometimes certain data points seem 'missing' in the plots. This means that the solution was not converged for this point. There are a few possible causes for this and they are discussed in appendix C. If the trend is clear not all the data points are always individually analysed to find the cause of failure and recomputed.

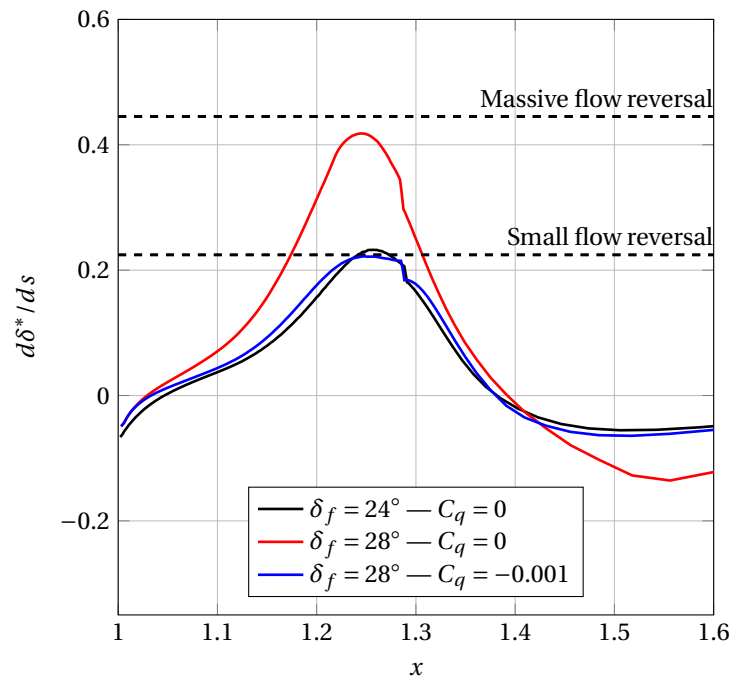


Figure 6.5: Spreading rate of  $\delta^*$  — NLR7301 —  $\alpha = 8^\circ$ . For a flap deflection of  $24^\circ$  and no suction the wake is on the verge of bursting. For  $\delta_f = 28^\circ$  the critical value for  $\frac{d\delta^*}{ds}$  has been well exceeded. This is also translated in the fact lift tops off for this flap deflection (figure 6.7).

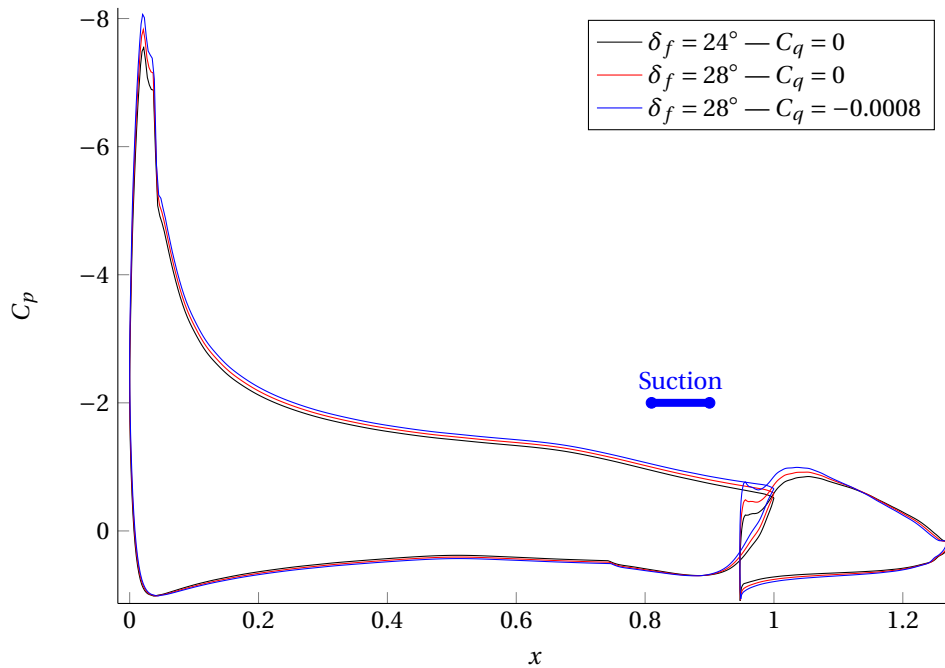


Figure 6.6: Pressure distribution — NLR7301 —  $\alpha = 8^\circ$ . An increase in circulation over the whole airfoil system is visible, both for increasing the flap deflection and by preventing wake burst with suction. The 'dumping velocity' at the TE is also increased.

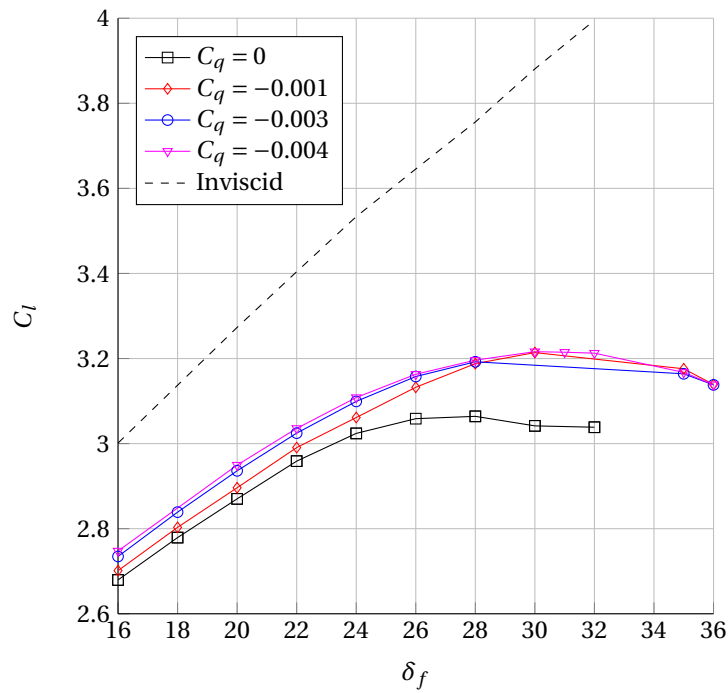


Figure 6.7: Lift coefficient vs. flap deflection at  $\alpha = 8^\circ$  — NLR7301. Suction allows higher flap deflections without a loss of lift by avoiding wake burst.

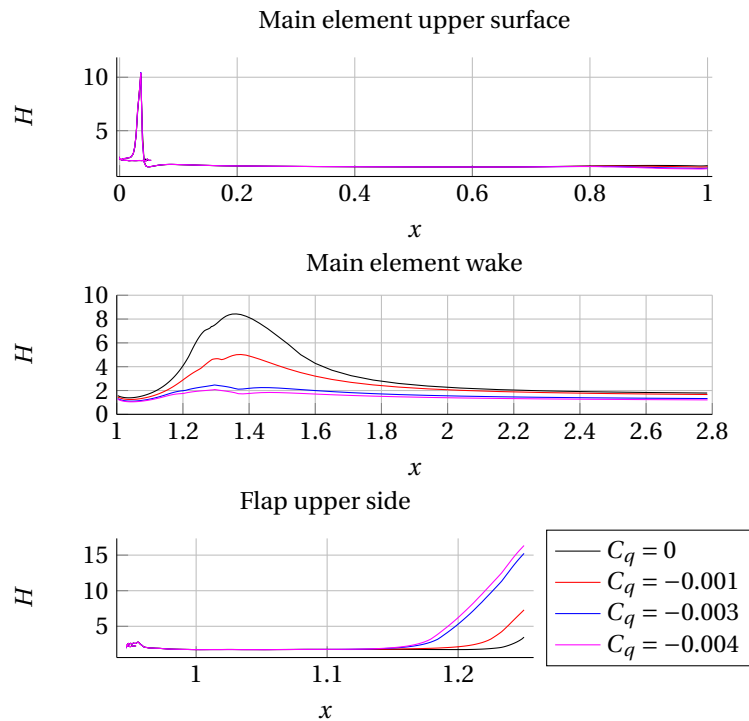


Figure 6.8: Shape factor  $H$  — NLR7301 —  $\alpha = 8^\circ$  —  $\delta_f = 28^\circ$ . No surface separation is present in any of the cases, except TE separation on the flap which is aggravated by applying suction.

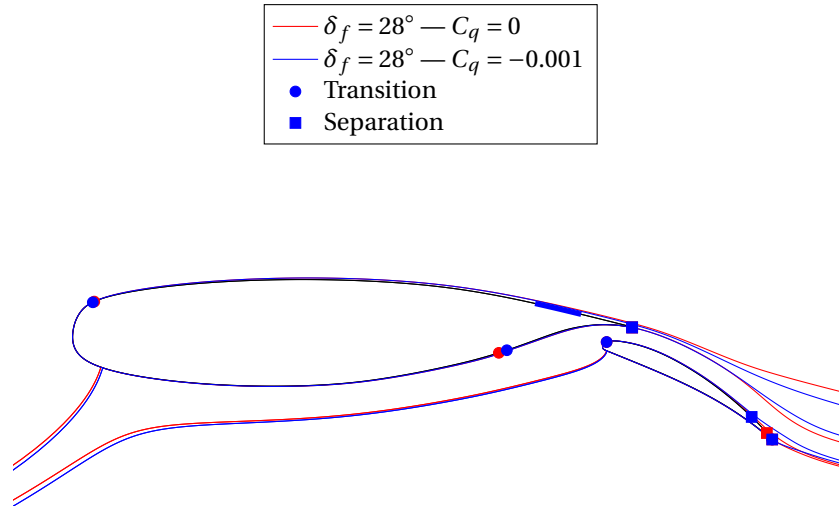


Figure 6.9: Streamlines — NLR7301 —  $\alpha = 8^\circ$ . Separation indicators at the TE indicate that there is actually no separation.

#### DIFFERENT SUCTION LEVELS

Apart from the case of  $v_w = -0.01$  already discussed thoroughly before, two other suction levels are presented to investigate the influence of the suction level. For these two additional cases the normal velocity at the wall (suction velocity) is increased to  $v_w/u_\infty = -0.03$  and  $v_w = -0.04$  at the same suction location, i.e. at  $x/c = 0.81$  to  $x/c = 0.91$ . This leads to suction coefficients of  $C_q = -0.003$  and  $-0.004$ .

As can be observed in figure 6.7, an increase in the suction level does not produce more lift, certainly not in the region where wake burst is observed, i.e. beyond a flap deflection angle of  $\delta_f = 24^\circ$ . This is explained by figure 6.10: while still a spectacular decrease in the spreading rate of  $\delta^*$  is observed for increasing  $v_w/u_\infty$  from  $-0.01$  to  $-0.03$  this has no effect on the wake other than reducing its displacement effect somewhat further. Wake burst has already been avoided by applying much milder suction (at  $v_w/u_\infty = -0.01$ ) which yielded a significant gain in lift but stronger suction does not ‘undo’ the wake burst even more and hence does not result in more lift.

In figure 6.8 can be observed how the shape factor changes with the different suction levels. For the wake the behaviour is analogous to  $\frac{d\delta^*}{ds}$  and a small decrease for  $H$  can be observed at the suction location. At the TE of the flap something else entirely can be seen however: higher suction levels led to TE separation here, which is evident from the shape factor and figure 6.11 showing the streamlines. This can be interpreted in two ways: the first is that the increased circulation by avoiding wake burst increases the circulation to such an extent that it creates a suction peak on the flap (visible in figure 6.6) that is so large the BL cannot cope with the adverse pressure gradient that is created by this. Another explanation is by means of the inviscid streamtubes: by limiting the displacement effect of the wake, the streamtube is allowed to become wider which inevitably leads to a stronger pressure rise, i.e. (again) a stronger pressure gradient on the flap. In a way, the displacement effect of the wake ‘pushes’ the BL onto the flap.

The small increase in lift that can be observed before wake burst is encountered has obviously nothing to do with avoiding wake burst. Here the wake is certainly not a dominant factor in the flowfield. In this case the small increase in lift can be attributed to the movement of  $\Delta n$  over the upper surface which affects the pressure distribution. By the suction the wake is also made thinner, which allows it to keep its (downward) momentum better which improves circulation.

#### SUCTION LOCATION

Figure 6.12 shows the influence of the suction location on the overall lift coefficient. The horizontal axis indicates the endpoints of the suction area, the width of the suction area is still the same as the cases presented

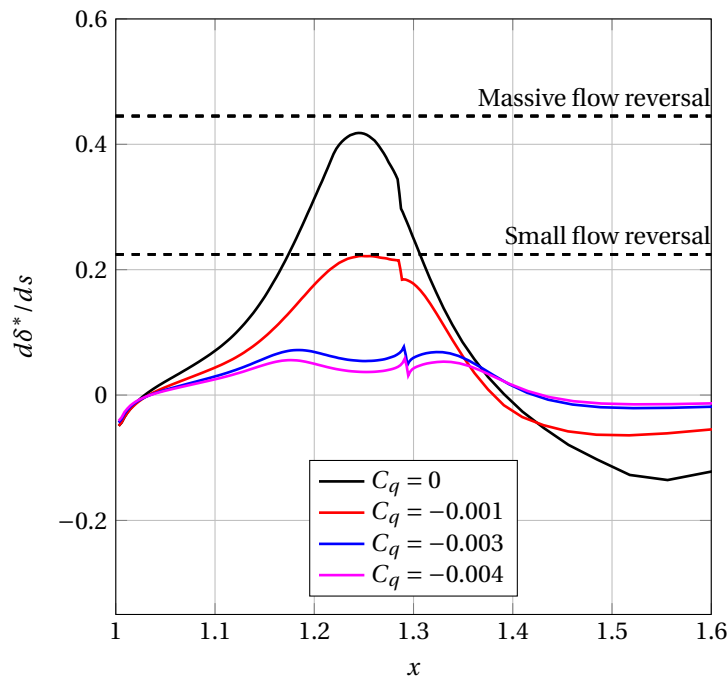


Figure 6.10: Spreading rate of  $\delta^*$  for different suction levels — NLR7301 —  $\alpha = 8^\circ$  —  $\delta_f = 28^\circ$ . A decrease in the spreading rate of  $\delta^*$  is observed for increasing  $v_w/u_\infty$  from  $-0.01$  to  $-0.03$  but this has no effect on the wake other than reducing its displacement effect somewhat further. Wake burst has already been avoided by applying much milder suction. The boundary layer at the TE is already almost at its minimum thickness for  $C_q = -0.003$ , so increasing suction even further has little effect on the wake growth.

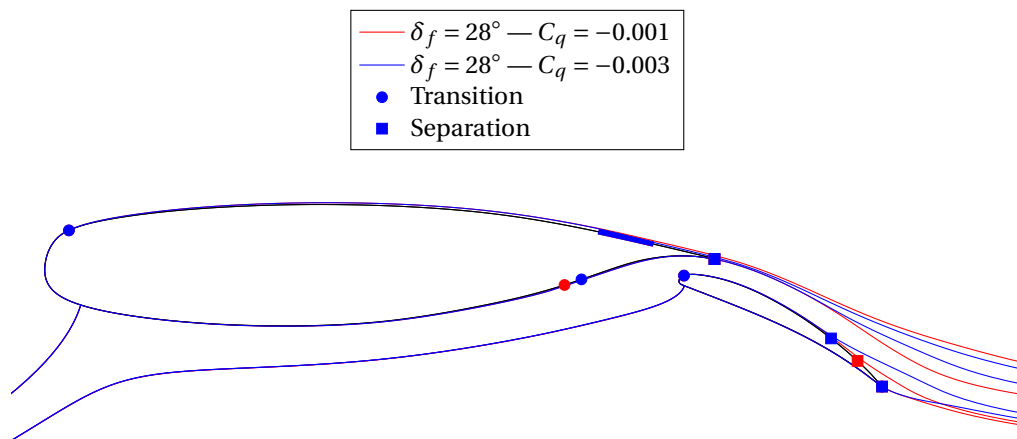


Figure 6.11: Streamlines for different suction levels — NLR7301 —  $\alpha = 8^\circ$

in the previous section. Especially for low suction levels, it is clear that it is beneficial to apply suction as much to the trailing edge as possible. This makes sense: bringing the suction location forward allows the BL to grow again before it is shed at the TE; while the goal is to minimize the width of the wake here. This is confirmed by looking at figure 6.13: the maximum spreading rate of  $\delta^*$  encountered in the wake is more efficiently countered when the suction location is near the trailing edge, this is especially the case for lower suction levels.

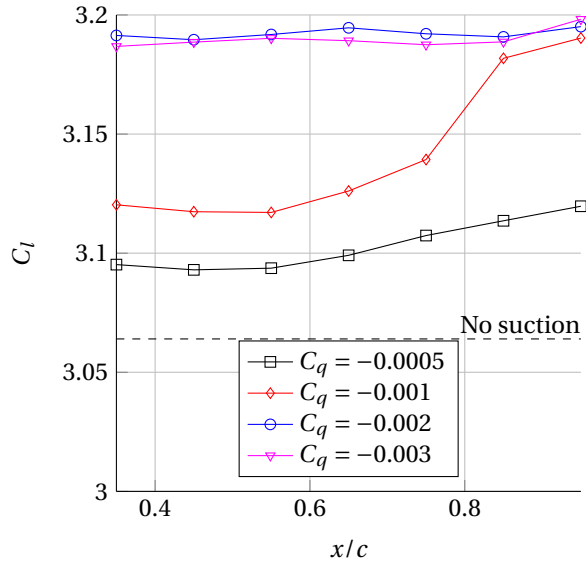


Figure 6.12: Lift coefficient for different suction locations. NLR7301 —  $\alpha = 8^\circ$  —  $\delta_f = 28^\circ$ . The horizontal axis indicates the endpoints of the suction area. Lift is more efficiently increased by applying suction towards the TE because the influence on the wake is more effective over there.

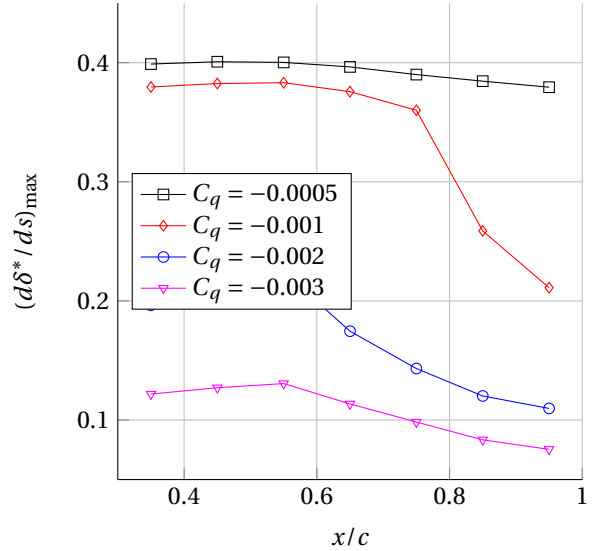


Figure 6.13:  $(\frac{d\delta^*}{ds})_{\max}$  in the main element wake for different suction locations. NLR7301 —  $\alpha = 8^\circ$  —  $\delta_f = 28^\circ$ . The horizontal axis indicates the endpoints of the suction area. Lift is more efficiently increased by applying suction towards the TE since limiting the growth of the wake is more effective in this way.

## 6.2. MFFS026

The MFFS026 airfoil is an airfoil used specifically for researching the wake burst phenomenon by Pomeroy et al. (see e.g. [30, 70]). It is therefore also an interesting case to simulate in the context of this project. The flow around the airfoil system is nowhere stalled near the TE nor is there massive separation, or to put it with the words of Pomeroy et al. ‘the flow is well behaved’; despite that the flowfield does show signs of the onset of wake burst. This is important since MatSESuction cannot simulate flow regions with massive separation. The simulations were run at a Reynolds number of  $Re = 1 \cdot 10^6$ . Figure 6.14 shows the airfoil configuration.

The results presented in [30, 70] do not lend themselves to directly compare them to those from MatSESuction due to their different nature. A part of the lift polar is shown for reference in figure 6.15; the agreement is good although MatSESuction overpredicts  $C_l$  somewhat.

Concerning the wake, Pomeroy et al. report that bursting occurs in the main wake at  $x/c \approx 0.96$  (and  $y/c \approx -0.13$ ) and the flap wake at  $x/c \approx 0.95$ . Pomeroy et al. use a much more ‘relaxed’ definition for wake burst, in the sense that not flow reversal or a loss of lift qualifies as ‘wake burst’, but merely rapid expansion of the wake and an increasing velocity deficit; in the presented case the wake core velocity only slows down to  $0.7u_\infty$ . This is shown in figure 6.16. This behaviour is also picked up by MatSESuction, shown in figure 6.17: the spreading rate of the wake indicates that the wake is also growing (much) more rapidly around the locations observed by Pomeroy et al. as being the locations of ‘wake burst’ (i.e.  $x/c = 0.96$  and  $x/c = 0.95$ ). It is much more outspoken for the main element wake than the flap wake, but from figure 6.16 it is clear that the ‘strength’ of the ‘wake burst’ is also much stronger for this one.

### 6.2.1. MFFS026 WITH SUCTION

The ‘wake burst’ for the reference case discussed above is very weak and it does not cause significant decambering of the airfoil system yet. More interesting cases with respect to this can be found for larger flap deflections at higher angles of attack. Figure 6.7 shows the variation of the lift coefficient with flap deflection

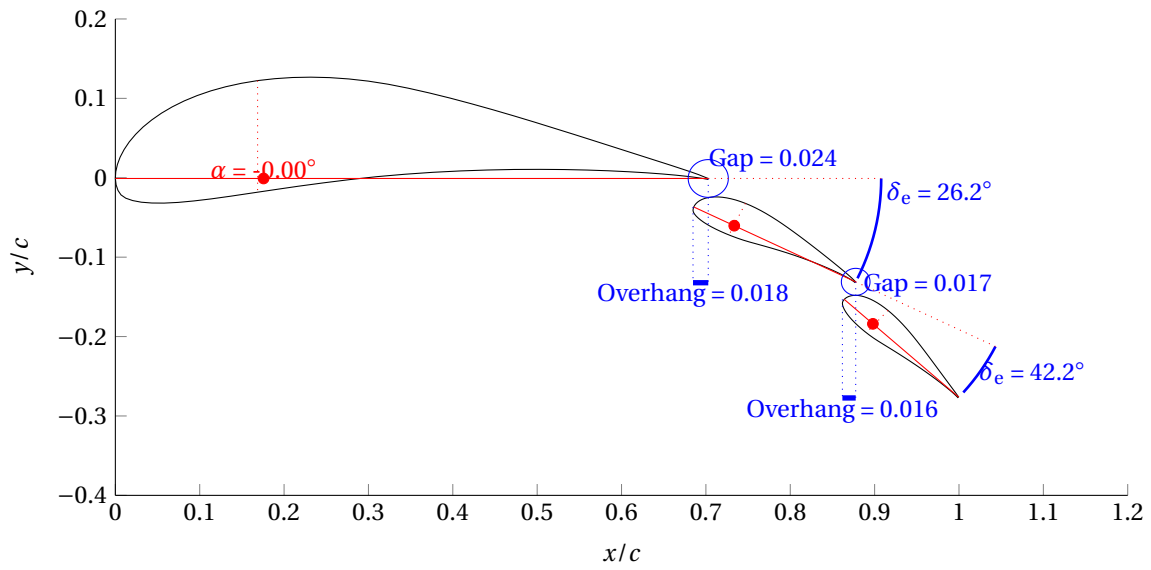


Figure 6.14: MFFS026 airfoil geometry.

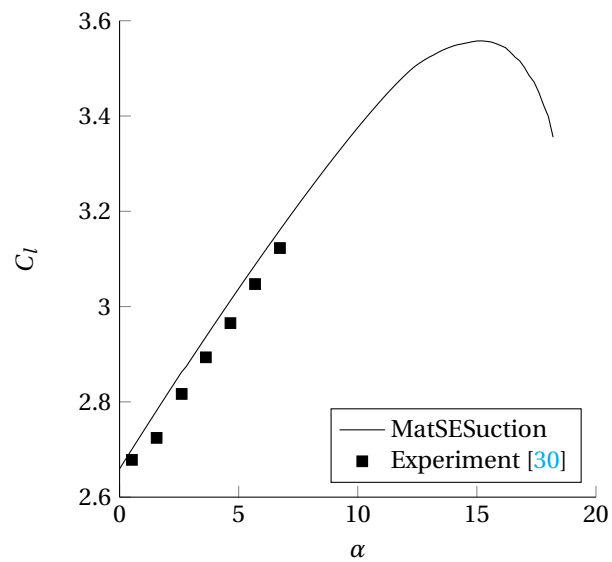


Figure 6.15: MFFS026 case: comparison of lift polars.

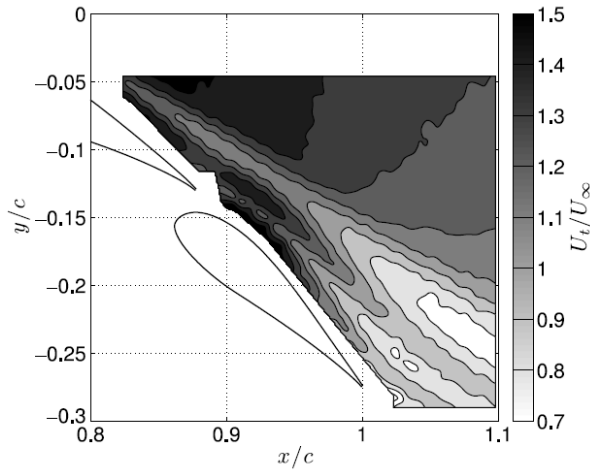


Figure 6.16: MFFS026 case: contour plot of flow velocity along flow direction  $U_t$  from the experiment by Pomeroy et al. [30]

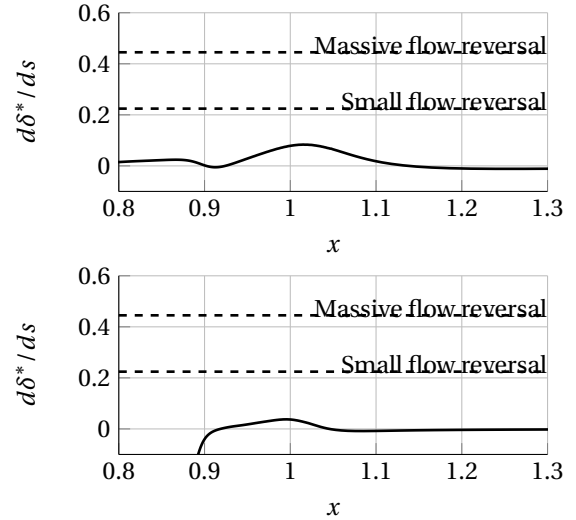


Figure 6.17: MFFS026 case:  $\frac{d\delta^*}{ds}$  at  $\alpha = 0^\circ$  as computed by MatSESuction. Upper figure is for main element wake, lower figure for first flap wake.

at  $\alpha = 12^\circ$ . The indicated flap deflection on the horizontal axis is that of the second flap; the first flap is always at a deflection of  $16.5^\circ$  less. A clear change in the trend of the lift is visible at  $\delta_{f_2} = 42^\circ$ , although figure 6.22 showing the shape factor does not suggest separation and also figure 6.21 showing the streamlines does not indicate this — with the exception of the onset of trailing edge separation on the second flap, which gets stronger with increasing suction, [very similar to the NLR7301 case](#).

Applying suction proves again to be successful in avoiding wake burst, as evidenced by figures 6.19 and 6.20: for a flap deflection of  $\delta_f = 45^\circ$  wake burst is avoided by applying suction between  $x/c = 0.8$  to  $x/c = 0.9$  with a wall velocity of only  $v_w = -0.005$  ( $C_q = -0.0005$ ). As a result, the lift coefficient is increased from 3.5 to 3.6, or an increase of 3%. Increasing the suction level limits the spreading of the wake even further but only has a marginal effect on the eventual lift coefficient. For a larger flap deflection ( $\delta_f = 47^\circ$ ) a higher suction level is necessary to lower the spreading rate of  $\delta^*$  below the critical value, now this is only achieved for  $C_q = -0.001$ . The lift coefficient increases from 3.5 to 3.64 and 3.7 for  $C_q = -0.0005$  and  $C_q = -0.001$  respectively. The comparison the two cases of  $\delta_{f_2} = 45^\circ$  and  $47^\circ$  demonstrates nicely how increasing the suction level is only beneficial if it ‘pulls’ the spreading rate of the wake below the critical value of 0.23. This is also the reason why no suction was applied over the first flap: at no point the wake of the first flap comes in the neighbourhood of the ‘danger zone’.

Briefly revisiting figure 6.22 it can be observed that — when it comes to wake burst — a critical value of  $H \approx 5$  can again be distinguished: when the shape factor in the wake rises above 5 wake burst is likely and the other way round.

### 6.3. THE APPLICATION OF SUCTION TO AVOID WAKE BURST: THE GENERAL CASE

In section 6.1 and 6.2 the application of suction to avoid wake burst on the NLR7301 and MFFS026 airfoil systems was discussed. Both cases show results that are in line with each other: in case of wake burst, the overall lift can be successfully increased by applying suction. A clear link between suction and the growth rate of  $\delta^*$  in the wake can be distinguished; and by keeping  $\frac{d\delta^*}{ds}$  below the critical value wake burst is avoided. In the case of the NLR7301 the lift coefficient is increased from 3.064 to 3.196 (or an increase of 4.31%) and for the MFFS026 it is increased from 3.5 to 3.6 (3%). For a successful application the goal should be to minimize the thickness of the wake that is shed at the trailing edge. Therefore, it makes more sense to apply suction close to the TE, especially since this also allows the static pressure to rise at the suction location which relaxes the requirements for the BLS system.

The discussion of the NLR7301 and MFFS026 case is limited to the complete airfoil systems being at an angle of attack of  $8^\circ$  and  $12^\circ$  respectively. This choice of angle of attack is rather arbitrary, but nevertheless

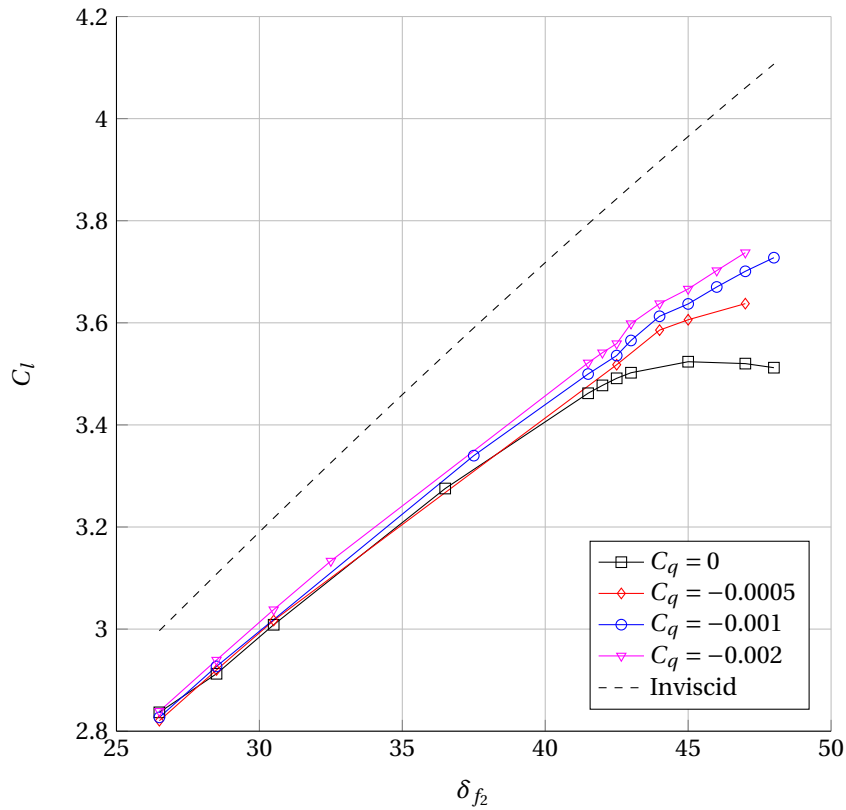


Figure 6.18: Lift coefficient vs. flap deflection — MFFS026 —  $\alpha = 12^\circ$ . The lift tops off at at  $\delta_{f2}$  without suction due to wake burst. This is however successfully prevented with suction which allows the lift to increase further with flap deflection.

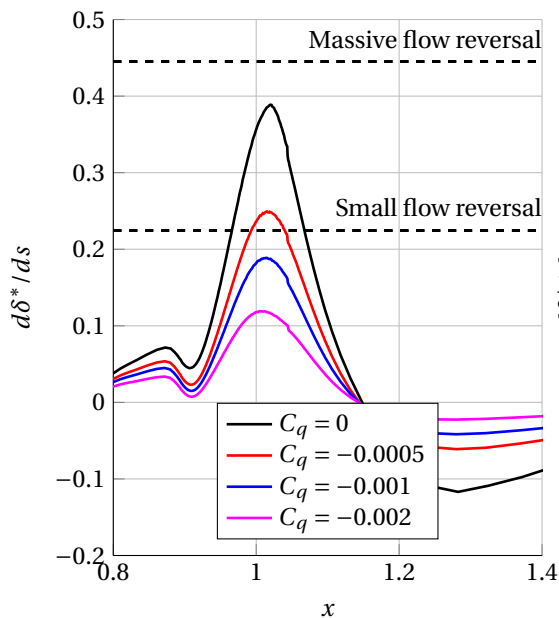


Figure 6.19: Spreading rate of  $\delta^*$  — MFFS026 —  $\alpha = 12^\circ$  —  $\delta_f = 45^\circ$

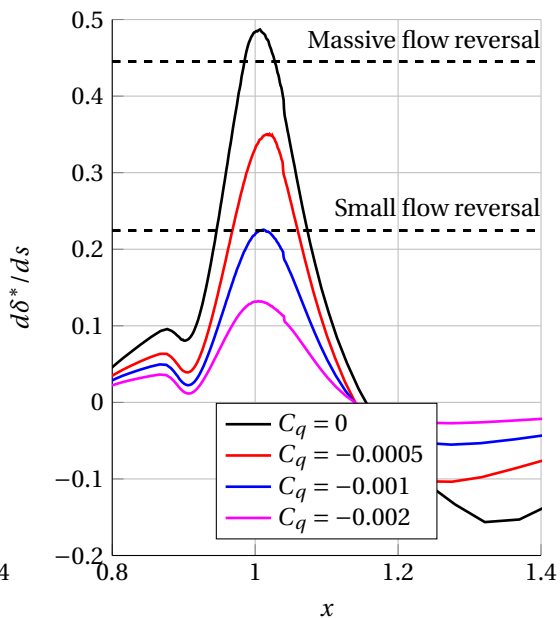


Figure 6.20: Spreading rate of  $\delta^*$  — MFFS026 —  $\alpha = 12^\circ$  —  $\delta_f = 47^\circ$ . A suction level of  $C_q = -0.0005$  is not sufficient to prevent wake burst which is also reflected in the lift that is obtained by this configuration (figure 6.18).

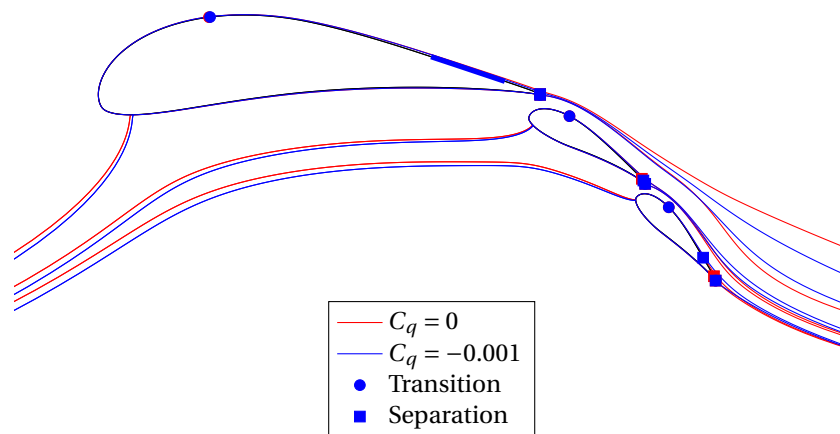


Figure 6.21: First streamlines — MFFS026 —  $\alpha = 12^\circ$  —  $\delta_{f_2} = 47^\circ$ . Suction clearly limits the growth of the wake (this is especially true over the second element which is the critical location) which successfully increases the overall circulation.

based on a situation as would be the case during a ‘high-lift’ situation — i.e. during take-off or landing — where the airfoil is at an elevated angle of attack but not too close to stall. As can be expected, similar results are found at other angles of attack. The results differ in value but the observed trend is identical: BLS helps to limit the wake growth and in turn wake burst, which successfully improves lift performance. This effect becomes less apparent at lower angles of attack. At lower angles of attack the BL growth on the main elements is not as strong and the wake that is shed at the TE is already thin enough so wake burst does not occur. The adverse pressure gradient imposed by the flap also causes the wake to grow but by increasing the flap deflection the same adverse pressure gradient causes the BL *on* the surface to separate earlier than wake burst is encountered. In this case applying suction to prevent wake burst obviously does not yield a significant increase in lift performance.

A not unimportant particularity with respect to the BL development on the flap was observed for both cases: keeping the growth of the wake in check may promote trailing edge separation over the underlying flap. This is caused by a stronger pressure rise, i.e. a stronger pressure gradient, on the flap due to the increased circulation. Another way to look at it is that a slower growing wake causes the inviscid streamtube between the wake and the element to grow faster which leads again to a higher adverse pressure gradient. In a way, the large wake ‘pushes’ the BL of the underlying element on the surface. Despite the fact of this earlier onset of TE separation on the flap, the overall lift is still higher when wake burst is prevented for both cases.

Also a third case was envisaged to be simulated and discussed here, but unexpected problems with solving the flowfield prevented this. A solution was not readily available to fix this and it was decided to drop this case. Section C.4 in appendix C discusses the problems with this case to some length.

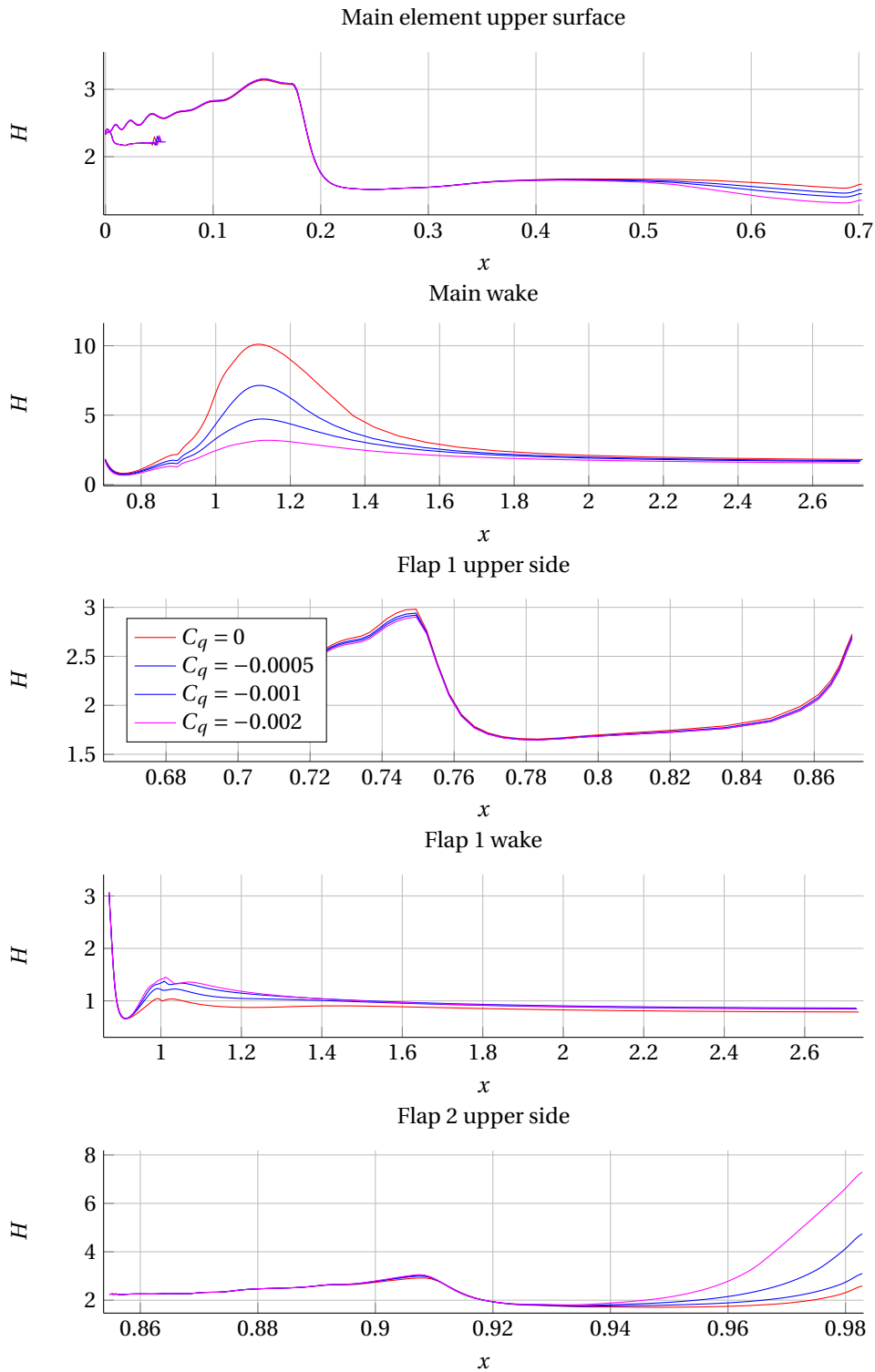


Figure 6.22: Shape factor over the upper surfaces and in the wake — MFFS026 —  $\alpha = 12^\circ$  —  $\delta_{f_2} = 47^\circ$ . Separation is absent everywhere, except at the trailing edge of the second flap. Stronger suction aggravates this, this is discussed in section 6.1.2.



# 7

## CONCLUSION & RECOMMENDATIONS

With the ongoing push towards simpler and lighter high-lift systems caused by a desire for simpler, lighter and thus more fuel-efficient aircraft the benefits of active boundary layer control for lift enhancement are investigated. Literature research shows that boundary layer suction is by now a mature research field, although the use of active boundary layer control has somewhat focused on periodic excitation methods when it comes to multi-element airfoil applications. The available research shows that boundary layer suction can significantly improve the maximum lift performance of multi-element airfoils. However, in practice their application is uncommon. This may be due to the additional power generation that is necessary to drive such a system. The work presented in this thesis aims to find solutions for a BLS system for multi-element airfoils with low pump requirements, that could potentially be driven by naturally occurring low pressure zones.

MSES was chosen as the platform to simulate the flow, an inviscid-viscid flow solver with the capability to simulate multi-element airfoils. The code had to be (re-)adapted to make it possible to simulate boundary layer suction, which was a part of this thesis presented in chapter 3. This was followed by a validation yielding the following conclusions:

- The simulation of larger areas of continuous suction is well predicted, the error for the suction cases is on the same order as the non-suction case. Agreement with rFoilsuc (also an inviscid-viscid flow solver adapted for BLS, although for single elements) is excellent.
- In the case of slot suction the effect of the recirculation zones at the slot entrance cannot be captured and this resulted in an underprediction of  $\theta$ . Comparison with experimental data showed that this did not affect the prediction of the 'outer flow' very much, but the underestimation of  $\theta$  may become a problem in cases with severe adverse pressure gradients where separation becomes an issue.
- The reliability of the flow prediction near  $C_{l_{max}}$  is unclear and varies from case to case. Therefore it is advisable to avoid using results near this area.

Chapter 5 continued with exploring the requirements of boundary layer suction. The equation for the power requirement for an ideal pump was used to identify two main factors. The first is the total pressure rise that must be overcome: it can be concluded that it is desirable to apply suction where the static pressure is relatively high. This is translated in the suction *location*: zones with suction peaks (such as the leading edge upper surface) are to be avoided. The suction location and required underpressure is a factor not recognized in the available literature. The other factor is the volumetric flow rate of the air mass being sucked away; it is obviously desirable to keep both the *suction area* and *suction strength* low to keep this factor low and as such also the overall power requirement. A good measure for this is the suction coefficient  $C_q$  as given in equation (5.2) since it is essentially a non-dimensionalized version of the volumetric flow rate.

With the desired suction location in mind, i.e. on the upper surface towards the trailing edge, the idea of trying to influence the wake with suction is pursued and becomes the focus of this project. This rather than for example using suction to try and avoid trailing edge separation because this requires strong suction over large areas, strongly increasing the volumetric flow rate and as such the eventual power requirement of

the BLS system. In multi-element airfoil systems, a rapid expansion of the wake may start to dominate the flowfield leading to a loss of lift — known as ‘wake burst’. Suction can delay this effect by thinning the wake making it able to withstand stronger adverse pressure gradients.

When trying to avoid wake burst it obviously comes in handy if there is a way of assessing the severity of the wake burst. How close is a certain configuration to it? This is a recurring problem in the available literature (see e.g. [70]), partly because of the fact that there is no clear definition for it. An assessment was made of several parameters (and combinations of it) and a rather good criterion was found — based on experimental values from literature — that could consistently link the spreading rate of the wake  $\left(\frac{d\delta^*}{ds}\right)$  to a loss of lift of the overall system for the results of MatSESuction:

$$\text{The onset of wake burst can be expected when: } 0.23 < \frac{d\delta^*}{ds} < 0.44$$

Applying suction towards to the trailing edge of the main element of the NLR7301 airfoil ( $\delta_f = 28^\circ, \alpha = 8^\circ$ ) shows promising results: the maximum value of  $\frac{d\delta^*}{ds}$  along the main element wake is successfully limited below the critical value with an associated gain in lift as a result. For example, for a wall transpiration velocity of  $v_w = -0.01$  over  $x/c = 0.81-0.91$ , suction coefficient  $C_q = -0.001$  the lift coefficient is increased from 3.064 to 3.196 or an increase of 4.31%. Also applying suction on a geometrically different case, the MFFS026 ( $\delta_{f2} = 47^\circ, \alpha = 12^\circ$ ), again shows that the wake burst is avoided. Here the lift is increased from 3.5 to 3.7 for  $C_q = -0.001$ .

These BLS specifications are on the same order of magnitude as other results from literature in [39, 52], however the increase in  $C_l$  is lower ( $\Delta C_l = 0.132$  against  $\Delta C_l \approx 0.3$  and  $\approx 0.6$  respectively). Comparing the suction configuration and results with those presented in [53] (where  $C_q$  is up to 0.12) the suction requirement is much lower but also the increase in lift is lower ( $\Delta C_l = 0.132$  against  $\Delta C_l$  almost 0.9). The above discussion applies to the NLR7301 case with a flap deflection of  $28^\circ$  and at an angle of attack of  $\alpha = 8^\circ$ . Other flap deflections and angles of attack yield different results of course, the presented case is chosen rather arbitrarily based on the fact that it is a representative value for an aircraft in a high-lift situation (i.e. elevated angle of attack but not too close to  $\alpha_{C_{l\max}}$ ). It is clear however that applying suction near the trailing edge does not show very much improvement of  $C_l$  in a case where there is no wake burst present.

The above comparison shows that applying suction towards the trailing edge does not yield a significant benefit over earlier investigated BLS configurations, nor does it perform significantly worse but with the consideration that it only makes sense when wake burst is present. But as was already noted before, only comparing  $C_q$  does not tell the whole story. The BLS configurations from literature all feature suction at locations where the pressure is already very low, which will in practice require a lot of power to generate the increase in total pressure that is required to maintain the suction distribution. This again calls for a strong pump, let alone making it possible to use a naturally occurring low pressure zone to drive the BLS. It becomes then a question of balancing the ‘power’ that is willing to be ‘invested’ in the BLS system with the suction location and strength.

As could be expected, increasing the suction level beyond what is necessary to avoid wake burst does not yield a further increase in lift. It suffices to keep the spreading rate of the displacement thickness of the wake below the critical value of  $\sim 2.3$ , a further increase in the suction level is not necessary.

The suction location to successfully avoid wake burst with BLS is as much to the trailing edge as possible. This is because the boundary layer just starts growing again after the suction location, and applying suction more to the front of the airfoil will eventually results in a thicker wake being shed at the trailing edge. A welcome side effect of this is that by moving the suction location to the rear, the static pressure rises which relieves the requirement for the underpressure required to drive the BLS system.

In view of possible future research towards the behaviour of the wake in an adverse pressure gradient it is interesting to make a note about the shape factor  $H$  in the wake. The obtained results hint at a limiting value of  $H \approx 5$  for the wake above which wake burst can be expected; much in the same way as the critical value of  $\frac{d\delta^*}{ds} \approx 0.23$  is used in this work.

To end this conclusion an early attempt to assess the possibility to drive a BLS with a naturally occurring low pressure zone is made. In section 5.1 it was already explained that in order to make this possible it is at least required that the static pressure at the outlet is lower than that at the suction location:  $p_{out} < p_{in}$ . At

the suction locations of the cases presented in this report the pressure coefficient  $C_p$  varies approximately between  $-1$  and  $-2$ . One of the ideas put forward as low pressure zone is the low pressure zone at the wing tip under influence of the tip vortex. In an earlier project by the author it was found that the lowest pressure coefficients reached due to this effect are around  $C_p = -1$ , somewhat higher or lower depending on the angle of attack of the wing of course [72]. This would already make for a very critical case, in practice it would most probably not suffice to drive the BLS system. This does not mean that there is no benefit to be found at all: carefully choosing an outlet location and a ‘low-requirement’ suction configuration, the power requirement can be significantly relieved and — theoretically — bring it close to zero.

#### RECOMMENDATIONS

In chapter 4 it was found that although the prediction of continuous suction with MatSESuction was good this was not the case for slot suction. An opportunity for further research lies here to investigate better models for slot suction — or the possibility for them. This is not a trivial task however! It was already concluded in section 4.2 that the incorrect prediction of  $\theta$  is due to the the effect of small zones with flow reversal at the slot entrance. The severity of this effect is of course strongly linked to the slot geometry, such as slot width but also the radius of the inlet, the angle of the inlet with respect to the flow etc. A good model would have to take all of this into account.

Another recommendation linked to MatSESuction — and more generally MSES for that matter — is the implementation of better closure relations for the boundary layer equations near  $C_{l_{max}}$ . As was already remarked in section 4.3 rFoil is known to have superior models for this, which is also visible from figure 4.10. The development of rFoil (from X-foil) at the own faculty would be a good starting point for this since the basis of the boundary layer formulation is the same.

Concerning the obtained results it would be good to confirm the beneficial effect of suction on  $\frac{d\delta^*}{ds}$  (to keep it below the critical values in the wake) and indirectly the lift coefficient with other data. This data can be obtained either by CFD or experiment. Concerning using CFD, the following note can be made: in the literature consulted for this project also differential based full-blown CFD codes have a lot of trouble with simulating the massively separated region due to wake burst, not always giving reliable results. But now finding cases that are only on the onset of wake burst is much more difficult because running one configuration (i.e. one combination of geometry  $\alpha$ ,  $\delta_f$ ,  $C_q$ ,...) is much more expensive. However, with more recent and suitable turbulence models this seems to have improved somewhat and the results of this report could be used as a guideline. An advantage of this on the other hand is that velocity profiles can be obtained rather easily, which will without doubt enhance the insight in the problem.

To eventually make a more accurate assessment of the possibility of a BLS system with a naturally occurring low pressure zone, it is necessary to also have an estimation of the pressure losses in the BLS system. This requires an estimation of the pressure drop over the ‘suction sheet’ as well as the head loss in the tubing system. When further pursuing this search to a ‘naturally driven’ BLS system this problem should certainly get attention.



## BIBLIOGRAPHY

- [1] M. Recksiek, *Advanced high lift system architecture with distributed electrical flap actuation*, in *Proceedings of the 2nd International Workshop on Aircraft System Technologies* (2009) pp. 49–59.
- [2] J. Meister and J. Pfennig, *Boundary layer suction arrangement*, (2010), uS Patent 7,837,155.
- [3] A. A. Merchant, *Design and analysis of supercritical airfoils with boundary layer suction*, Master's thesis, Massachusetts Institute of Technology. Dept. of Aeronautics and Astronautics (1996).
- [4] G. de Oliveira Andrade, *Wind Turbine Airfoils with Boundary Layer Suction - A novel Design approach*, Master's thesis, TU Delft, Delft University of Technology, Delft (2011).
- [5] J. D. McLean, J. D. Crouch, R. C. Stoner, S. Sakurai, G. E. Seidel, W. M. Feifel, and H. M. Rush, *Study of the Application of Separation Control by Unsteady Excitation to Civil Transport Aircraft*, Technical Report NASA/CR-1999-209338 (NASA, NASA Langley Research Center, 1999).
- [6] J. K. Wimpers, *AERODYNAMIC TECHNOLOGY APPLIED TO TAKEOFF AND LANDING*, [Annals of the New York Academy of Sciences](#) **154**, 962 (1968).
- [7] P. Meredith, *Viscous Phenomena Affecting High-Lift Systems and Suggestions for future CFD Development*, in *High-lift system aerodynamics: papers presented and discussions recorded at the 71st Fluid Dynamics Panel Meeting and at the symposium held in Banff, Alberta, Canada, from 5th - 8th October 1992 = (L'aérodynamique des systèmes hypersustentateurs)*, AGARD conference proceedings No. 515, edited by NATO and Symposium on High Lift System Aerodynamics (AGARD, Neuilly-sur-Seine, 1993) pp. 19–1 – 19–8.
- [8] Scott Anders, William Sellers III, and Anthony Washburn, *Active Flow Control Activities at NASA Langley*, in *2nd AIAA Flow Control Conference*, Fluid Dynamics and Co-located Conferences (American Institute of Aeronautics and Astronautics, 2004).
- [9] Anthony Washburn, Susan Gorton, and Scott Anders, *A Snapshot of Active Flow Control Research at NASA Langley*, in *1st Flow Control Conference*, Fluid Dynamics and Co-located Conferences (American Institute of Aeronautics and Astronautics, 2002).
- [10] William Bower and Valdis Kibens, *An Overview of Active Flow Control Applications at The Boeing Company*, in *2nd AIAA Flow Control Conference*, Fluid Dynamics and Co-located Conferences (American Institute of Aeronautics and Astronautics, 2004).
- [11] J. D. Anderson, *Fundamentals of Aerodynamics*, 4th ed. (McGraw-Hill, New York, 2007).
- [12] M. Tummers, K. Hanjalić, D. Passchier, and R. Henkes, *Computations of a turbulent wake in a strong adverse pressure gradient*, [International Journal of Heat and Fluid Flow](#) **28**, 418 (2007).
- [13] L. Prandtl and O. Tietjens, *Applied Hydro- and Aerodynamics* (Dover, New York) p227.
- [14] I. Abbott and A. Von Doenhoff, *Theory of Wing Sections, Including a Summary of Airfoil Data*, Dover Books on Aeronautical Engineering Series (Dover Publications, New York, 1959).
- [15] A. Nakayama, H.-P. KREPLIN, and H. L. MORGAN, *Experimental investigation of flowfield about a multi-element airfoil*, [AIAA Journal](#) **28**, 14 (1990).
- [16] A. M. O. Smith, *High-Lift Aerodynamics*, [Journal of Aircraft](#) **12**, 501 (1975).
- [17] I. Gartshore, *Predictions of the blowing required to suppress separation from high lift airfoils*, *CASI Transactions* **4**, 39 (1971).

- [18] S. Goldstein, *On laminar boundary-layer flow near a position of separation*, The Quarterly Journal of Mechanics and Applied Mathematics **1**, 43 (1948).
- [19] A. Veldman, *Quasi-Simultaneous Viscous-Inviscid Interaction for Transonic Airfoil Flow (invited)*, in *4th AIAA Theoretical Fluid Mechanics Meeting*, Fluid Dynamics and Co-located Conferences (American Institute of Aeronautics and Astronautics, 2005).
- [20] H. Schlichting and K. Gersten, *Boundary-Layer Theory*, 8th ed., Physic and astronomy (Springer, Heidelberg, 2000).
- [21] L. Veldhuis, *Reader Aircraft Aerodynamics*, (2012).
- [22] B. S. Stratford, *The prediction of separation of the turbulent boundary layer*, Journal of fluid mechanics **5**, 1 (1959).
- [23] M. R. Head, *Entrainment in the turbulent boundary layer*, Technical Report Rep. R and M 3152 (Aeronautical Research Council, England, 1960).
- [24] T. Cebeci, G. J. MOSINSKIS, and A. M. O. SMITH, *Calculation of Separation Points in Incompressible Turbulent Flows*, *Journal of Aircraft* **9**, 618 (1972).
- [25] L. Prandtl and A. Betz, *Vier Abhandlungen zur Hydrodynamik und Aerodynamik: Flüssigkeit mit kleiner Reibung; Tragflügeltheorie, I. und II. Mitteilung; Schraubenpropeller mit geringstem Energieverlust*, Göttinger Klassiker der Strömungsmechanik No. 3 (Univ.-Verl, Göttingen, 2010).
- [26] L. F. Crabtree, *Effects of Leading-Edge Separation on Thin Wings in Two-Dimensional Incompressible Flow*, *Journal of the Aeronautical Sciences* **24**, 597 (1957).
- [27] J. E. Carter and V. N. Vatsa, *Analysis of Airfoil Leading Edge Separation Bubbles*, Interim report CR165935 (1982).
- [28] C. L. Rumsey, T. B. Gatski, S. X. Ying, and A. Bertelrud, *Prediction of High-Lift Flows Using Turbulent Closure Models*, *AIAA Journal* **36**, 765 (1998).
- [29] S. X. Ying, F. W. Spaid, C. B. McGinley, and C. L. Rumsey, *Investigation of Confluent Boundary Layers in High-Lift Flows*, *Journal of Aircraft* **36**, 550 (1999).
- [30] B. W. Pomeroy, J. M. Diebold, P. J. Ansell, and M. S. Selig, *Study of Burst Wakes in a Multi-Element Airfoil Flowfield*, *AIAA Journal* **52**, 821 (2014).
- [31] D. Agoropoulos and L. C. Squire, *Interactions between turbulent wakes and boundary layers*, *AIAA Journal* **26**, 1194 (1988).
- [32] F. Bario, G. Charnay, and K. D. Papailiou, *An Experiment Concerning the Confluence of a Wake and a Boundary Layer*, *Journal of Fluids Engineering* **104**, 18 (1982).
- [33] L. J. Johnston and H. P. Horton, *An experimental study of turbulent wake/boundary layer mixing flows*, in *Proceedings of the International Congress of Aeronautical Sciences (ICAS)* (AIAA, 1986) pp. 360–369.
- [34] J. J. Cornish, *Practical High Lift Systems Using Distributed Boundary Layer Control* (Aerophysics Department, Mississippi State University, 1958).
- [35] M. Gad-El-Hak, *Flow Control*, 1st ed. (Cambridge University Press, Cambridge, 2000).
- [36] D. C. Hazen, *Film notes for Boundary Layer Control*, (1968), youtube video of lecture: <https://www.youtube.com/watch?v=w1Q6-NJPpk>.
- [37] L. A. Marshall, *Boundary-layer transition results from the F-16XL-2 supersonic laminar flow control experiment*, Technical Report TM-1999-209013 (NASA Dryden Flight Research Center, Edwards, California, 1999).
- [38] Wikipedia, *General Dynamics F-16XL*, [http://en.wikipedia.org/wiki/General\\_Dynamics\\_F-16XL#NASA](http://en.wikipedia.org/wiki/General_Dynamics_F-16XL#NASA) (2014).

- [39] E. L. Terry, *Extension of the aerodynamic design program MSES for the simulation of boundary layer suction*, Master's thesis, TU Delft, Delft University of Technology, Delft (2004).
- [40] Aerofiles, *The Humpback L-1*, <http://aerofiles.com/humpback-L1.html> (2005).
- [41] Wikipedia, *Shin Meiwa US-1A*, [http://en.wikipedia.org/wiki/Shin\\_Meiwa\\_US-1A](http://en.wikipedia.org/wiki/Shin_Meiwa_US-1A) (2014).
- [42] Wikipedia, *Blackburn Buccaneer - Wikipedia, the free encyclopedia*, [https://en.wikipedia.org/wiki/Blackburn\\_Buccaneer](https://en.wikipedia.org/wiki/Blackburn_Buccaneer) (2015).
- [43] H. Atik, C.-Y. Kim, J. Walker, and L. Van Dommelen, *Boundary-Layer Separation Control on a Thin Airfoil Using Suction - Physical Examples*, <http://www.eng.fsu.edu/~dommelen/courses/eml5935/00/topics/101601/node2.html#SECTION00020000000000000000> (10/16/01).
- [44] NASA, *NASA - NASA Dryden Technology Facts - F-16XL Supersonic Laminar Flow*, [http://www.nasa.gov/centers/dryden/about/Organizations/Technology/Facts/TF-2004-12-DFRC\\_prt.htm](http://www.nasa.gov/centers/dryden/about/Organizations/Technology/Facts/TF-2004-12-DFRC_prt.htm).
- [45] T. van der Hoeven, *Slot suction in the turbulent boundary layer*, Master's thesis, TU Delft, Delft University of Technology, Delft (2013).
- [46] W. L. Sellers, G. S. Jones, and M. D. Moore, *Flow Control Research at NASA Langley in Support of High-Lift Augmentation*, (Williamsburg, VA, United States, 2002).
- [47] M. E. Desalvo, E. A. Whalen, and A. Glezer, *Enhancement of High-Lift System Flap Performance using Active Flow Control*, in *52nd Aerospace Sciences Meeting*, AIAA SciTech (American Institute of Aeronautics and Astronautics, 2014).
- [48] J. H. Quinn, *Tests of the NACA 64(1)A212 airfoil section with a slat, a double slotted flap, and boundary-layer control by suction.pdf*, Technical Note 1293 (National Advisory Committee for Aeronautics, Langley Memorial Aeronautical Laboratory Langley Field, Va., 1947).
- [49] E. Collett, *Aircraft wing leading edge high lift device with suction*, (2000).
- [50] F. Satta, M. Ubaldi, P. Zunino, and C. Schipani, *WAKE CONTROL BY BOUNDARY LAYER SUCTION APPLIED TO A HIGH-LIFT LOW-PRESSURE TURBINE BLADE*, in *PROCEEDINGS OF THE ASME TURBO EXPO 2010: TURBOMACHINERY: AXIAL FLOW FAN AND COMPRESSOR AERODYNAMICS DESIGN METHODS, AND CFD MODELING FOR TURBOMACHINERY, VOL 7, PTS A-C* (AMER SOC MECHANICAL ENGINEERS, THREE PARK AVENUE, NEW YORK, NY 10016-5990 USA, 2010) pp. 1571–1582, aSME Turbo Expo 2010, Glasgow, SCOTLAND, JUN 14-18, 2010.
- [51] A. Shmilovich and Y. Yadlin, *Flow Control Techniques for Transport Aircraft*, *AIAA Journal* **49**, 489 (2011).
- [52] A. Khodadoust and A. Shmilovich, *High Reynolds Number Simulation of Distributed Active Flow Control for a High-Lift System*, in *25th AIAA Applied Aerodynamics Conference*, Fluid Dynamics and Co-located Conferences (American Institute of Aeronautics and Astronautics, 2007).
- [53] J. Wijnen, *Passive separation control on a wing-flap combination through steady boundary layer suction*, Master's thesis, TU Delft, Delft University of Technology, Delft (2011).
- [54] M. Drela and M. B. Giles, *Viscous-inviscid analysis of transonic and low Reynolds number airfoils*, *AIAA Journal* **25**, 1347 (1987).
- [55] M. Drela, *Two-Dimensional Transonic Aerodynamic Design and Analysis Using the Euler Equations*, Phd thesis, Massachusetts Institute of Technology. Dept. of Aeronautics and Astronautics (1985).
- [56] A. Merchant and M. Drela, *Design and analysis of supercritical suction airfoils*, in *14th Applied Aerodynamics Conference*, Fluid Dynamics and Co-located Conferences (American Institute of Aeronautics and Astronautics, 1996).
- [57] M. Drela, *A User's Guide to MSES 3.04*, (2006).
- [58] M. Drela and M. Giles, *ISES - A two-dimensional viscous aerodynamic design and analysis code*, (American Institute of Aeronautics and Astronautics, 1987).

- [59] F. White, *Viscous Fluid Flow*, 3rd ed. (McGraw-Hill, New York, 2006).
- [60] A. Favre, R. Dumas, and E. Verollet, *Couche limite sur paroi plane poreuse*, Tech. Rep. 39001554 (CEA Saclay, 91-Gif-sur-Yvette (France), Saclay, 1961).
- [61] J. Park and H. Choi, *Effects of uniform blowing or suction from a spanwise slot on a turbulent boundary layer flow*, [Physics of Fluids](#) **11**, 3095 (1999).
- [62] S. B. Pope, *Turbulent flows* (Cambridge university press, 2000).
- [63] D. M. Driver and G. G. Mateer, *Wake flow in adverse pressure gradient*, [International Journal of Heat and Fluid Flow](#) **23**, 564 (2002).
- [64] A. Starke, R. Henkes, and M. Tummers, *Effects of curvature and pressure gradient on a turbulent near wake*, [Experimental Thermal and Fluid Science](#) **19**, 49 (1999).
- [65] R. Hoffenberg and J. Sullivan, *Measurement and simulation of wake deceleration*, in *36th AIAA Aerospace Sciences Meeting and Exhibit*, Aerospace Sciences Meetings (American Institute of Aeronautics and Astronautics, 1998).
- [66] G. Bucci, J. Sullivan, G. Bucci, and J. Sullivan, *An experimental simulation of high lift wake flows at high Reynolds number*, (American Institute of Aeronautics and Astronautics, 1997).
- [67] F. O. Thomas and X. Liu, *An experimental investigation of symmetric and asymmetric turbulent wake development in pressure gradient*, [Physics of Fluids](#) **16**, 1725 (2004).
- [68] Fengjun Liu, William Liou, and Ronald Joslin, *Numerical Simulations of Confluent Wake/Boundary Layer Flows*, in *41st Aerospace Sciences Meeting and Exhibit*, Aerospace Sciences Meetings (American Institute of Aeronautics and Astronautics, 2003).
- [69] N. Duquesne, J. Carlson, C. Rumsey, and T. Gatski, *Computation of turbulent wake flows in variable pressure gradient*, in *30th Fluid Dynamics Conference*, Fluid Dynamics and Co-located Conferences (American Institute of Aeronautics and Astronautics, 1999).
- [70] B. W. Pomeroy and M. S. Selig, *Pressure Measurements of Burst Wakes Over a Three-Element Airfoil*, in *33rd AIAA Applied Aerodynamics Conference* (2015) p. 2569.
- [71] B. van den Berg and B. Oskam, *Boundary layer measurements on a two-dimensional wing with flap and a comparison with calculations*, in *In AGARD Turbulent Boundary Layers 14 p (SEE N80-27647 18-34)*, Vol. 1 (1980).
- [72] J. Van Craenenbroeck, *Wingtip vortex - Influence of the wingtip vortex on the lowest pressure on a NACA0018 wing with aspect ratio 5*, Honours Track Internship project (Delft University of Technology & NUMECA, Brussels, Delft, 2014).
- [73] D. L. Whitfield, *Integral solution of compressible turbulent boundary layers using improved velocity profiles*, Tech. Rep. (DTIC Document, 1978).
- [74] D. Whitfield, *Analytical description of the complete turbulent boundary layer velocity profile*, in *11th Fluid and Plasma Dynamics Conference*, Fluid Dynamics and Co-located Conferences (American Institute of Aeronautics and Astronautics, 1978).
- [75] T. W. Swafford, *Analytical approximation of two-dimensional separated turbulent boundary-layer velocity profiles*, [AIAA Journal](#) **21**, 923 (1983).

# A

## CLOSURE RELATIONS

This appendix summarizes the closure relations for boundary layer flow including suction after Merchant [3, 56].

### A.1. LAMINAR CLOSURE

**Kinetic energy shape parameter::**

$$H^* = f(H_k, M_e, Re_\theta)$$
$$= \begin{cases} 0.0111 \frac{(H_k - 4.35)^2}{H_k + 1} - 0.0278 \frac{(H_k - 4.35)^3}{H_k + 1} + 1.528 - 0.0002 ((H_k - 4.35) H_k)^2 & H_k < 4.35 \\ 0.0150 \frac{(H_k - 4.35)^2}{H_k} + 1.528 & H_k \geq 4.35 \end{cases} \quad (\text{A.1a})$$

**Density thickness shape parameter:** (after Whitfield [73])

$$H^{**} = f(H_k, M_e) = \left( \frac{0.064}{H_k - 0.8} + 0.251 \right) M_e^2 \quad (\text{A.1b})$$

**Skin friction coefficient**

$$C_f = f(H_k, M_e, Re_\theta)$$
$$\Rightarrow Re_\theta \frac{C_f}{2} = \begin{cases} 0.01977 \frac{(7.4 - H_k)^2}{H_k - 1} - 0.067 & H_k < 4 \\ 0.00918 - 0.035 (1 - e^{2(H_k - 4)}) & H_k \geq 4 \end{cases} \quad (\text{A.1c})$$

**Dissipation coefficient:**

$$C_\varnothing = f(H_k, M_e, Re_\theta)$$
$$\Rightarrow Re_\theta \frac{2C_\varnothing}{H^*} = \begin{cases} 0.00205 (4 - H_k)^{5.5} + 0.207 & H_k < 4 \\ -0.0016 \frac{(H_k - 4)^2}{1 + 0.02 (H_k - 4)^2} + 0.207 & H_k \geq 4 \end{cases} \quad (\text{A.1d})$$

**Kinematic shape parameter:** (after Whitfield [74])

$$H_k = \frac{H - 0.29 M_e^2}{1 + 0.113 M_e} \quad (\text{A.1e})$$

## A.2. TURBULENT CLOSURE

**Kinetic energy shape parameter:**

$$\begin{aligned}
 H^* &= f(H_k, M_e, Re_\theta) \\
 &= \begin{cases} \left(0.5 - \frac{4}{Re_\theta}\right) \left(\frac{H_0 - H_k}{H_0 - 1}\right)^2 \frac{1.5}{H_k + 0.5} + 1.5 + \frac{4}{Re_\theta} & H_k < H_0 \\ (H_k - H_0)^2 \left(\frac{0.007 \ln(Re_\theta)}{\left(H_k - H_0 + \frac{4}{\ln Re_\theta}\right)^2 + \frac{0.015}{H_k}}\right) + 1.5 + \frac{4}{Re_\theta} & H_k \geq H_0 \end{cases} \quad (A.2a) \\
 \text{with } H_0 &= \begin{cases} 4 & Re_\theta < 400 \\ 3 + \frac{400}{Re_\theta} & Re_\theta \geq 400 \end{cases}
 \end{aligned}$$

**Skin friction coefficient:** ( $C_{f_{w/o \text{ suction}}}$  after Swafford [75])

$$\begin{aligned}
 C_f &= C_{f_{w/o \text{ suction}}} - 2 \frac{\rho_w v_w}{\rho_e u_e} U_{\text{slip}} \\
 \text{with } C_{f_{w/o \text{ suction}}} &= \frac{0.3e^{-1.33H_k}}{F_c \left(0.4342 \ln\left(\frac{Re_\theta}{F_c}\right)\right)^{1.74+0.31H_k}} + \frac{0.00011}{F_c} \left(\tanh\left(4 - \frac{H_k}{0.875}\right) - 1\right) \quad (A.2b) \\
 F_c &= \sqrt{1 + 0.2M_e^2}
 \end{aligned}$$

**Dissipation coefficient:**

$$C_\varnothing = \frac{C_{f_{w/o \text{ suction}}}}{2} U_{\text{slip}} - \frac{1}{2} \frac{\rho_w v_w}{\rho_e u_e} U_{\text{slip}}^2 + C_\tau (1 - U_{\text{slip}}) \quad (A.2c)$$

**Maximum shear stress coefficient:** (the 'shear lag equation')

$$\begin{aligned}
 \frac{\delta}{C_\tau} \frac{dC_\tau}{d\xi} &= 4.2 \left(C_{\tau(\text{eq})}^{0.5} - C_\tau^{0.5}\right) + \left(\frac{2\delta}{u_e} \frac{du_e}{d\xi}\right)_{(\text{eq})} - \left(\frac{2\delta}{u_e} \frac{du_e}{d\xi}\right) \\
 \text{with } C_{\tau(\text{eq})} &= H^* \frac{0.0015 (H_k - 1)^3}{(1 - U_{\text{slip}}) H_k H} \quad (A.2d) \\
 \delta &= \theta \left(3.15 + \frac{1.72}{H_k - 1}\right) + \delta^*
 \end{aligned}$$

**Slip velocity:**

$$U_{\text{slip}} = \frac{H^*}{2} \left(1 - \frac{4}{3} \frac{H_k - 1}{H}\right) \quad (A.2e)$$

**Kinematic shape parameter:** (after Whitfield [74])

$$H_k = \frac{H - 0.29M_e^2}{1 + 0.113M_e} \quad (A.2f)$$

# B

## CHANGELOG MSES TO MATSESUCTION

Table B.1 shows a detailed overview of the changes made to the original Fortran MSES code in Fortran.

Table B.1: Detailed overview of the changes to the original MSES code and related programs.

Modified routines			
Routine	P/S	Located in	Description & Changes
MSES	P	mSES.f	<p>Main program for initializing the solution from a previous solution state (stored in the mdat.xxx file). Contains the main Newton loop for iteratively solving the Newton system (see section 3.1.1).</p> <ul style="list-style-type: none"><li>• Additional argument is required for defining the suction mode ('0' for no suction (in which case the calculations follow the original MSES code) and '1' for calculations taking into account suction).</li><li>• Initialize suction distribution and read and set the suction distribution if required.</li><li>• A fix for the 'oscillating solution problem'. It is not very advanced, but is able to break out of an 'oscillating solution loop' for the simulated cases. It can be turned off or on by an argument to the program.</li><li>• A special version for detecting convergence problems is also created that 'recycles' the MPLOTF function and provides output for every iteration (instead of output for every converged <math>\alpha</math>). This function too can be turned off easily albeit only before compilation.</li></ul>

Table B.1: (continued)

MSET	P	mset.f	<p>Program for initializing the solution and the grid for a given geometry and grid parameters based on a panel solution.</p> <ul style="list-style-type: none"> <li>• The ‘interactive’ part of the code is removed and all grid generation steps are followed automatically based on the grid parameter settings in the file gridpar.xxx.</li> <li>• To be able to check the grid visually afterwards, also a plot of the grid is dumped to the execution folder.</li> <li>• Additional argument added to determine the type of output (on screen (default), or dump in ps-files). Necessary because on-screen output pauses the program if the window is not activated and this is not acceptable for queued cases.</li> <li>• Initialize the suction variables included in STATE.INC to zero to be able to write them to the mdat.xxx-file. The actual suction distribution is read while running MSES in suction mode.</li> </ul>
MPOLAR	P	mpolar.f	<p>Program for driving MSES over a range of angle of attack (thus generating a polar curve).</p> <ul style="list-style-type: none"> <li>• Two additional arguments are added to the argument list: one that controls the number of maximum Newton iterations for every <math>\alpha</math> (previously it had to be set before compilation) and one to specify the suction mode (as in MSES).</li> <li>• Output of number of required Newton iterations to reach convergence for every <math>\alpha</math>.</li> <li>• A ‘specialized’ version of MPLOT (MPLOTF) is called after the solution is converged for a certain <math>\alpha</math> to automatically dump all required BL data etc. for every <math>\alpha</math> in the execution folder. The actual value of <math>\alpha</math> is included in the filename of the dumped files.</li> <li>• A fix for the ‘oscillating solution problem’. It is not very advanced, but is able to break out of an ‘oscillating solution loop’ for the simulated cases. It can be turned off or on by an argument to the program.</li> </ul>

Table B.1: (continued)

MPLOT, MPLOT2, MPLOTF	P	mplo.t.f, mplo.t2.f, mplo.tf.f	<p>Different incarnations of the original MPLOT program:</p> <ul style="list-style-type: none"> <li>• MPLOT: all user interaction is removed, instead the program automatically dumps all the grid, flowfield, BL and wall <math>C_p</math> in datafiles for later analysis. Also the data written to the BL datafile is extended to include suction information such as <math>v_w</math>, <math>\delta_{\text{suction}}^*</math> and <math>\Delta n</math>.</li> <li>• MPLOT2: program with all original (plotting) functionality, including the user interaction. It is recompiled to work with the changed mdat.xxx-files; however it does NOT include the possibility of plotting specific suction variables such as <math>v_w</math> or <math>\delta_{\text{suction}}^*</math>. On the other hand the dumped files do include them, just like for MPLOT.</li> <li>• MPLOTF: a ‘specialized’ version of MPLOT which can take a value for the angle of attack from the argument list. Another additional argument specifies which datafiles must be dumped (latest incarnation: ‘non’, ‘gbl’ and ‘obl’ to dump no datafiles, grid and BL data or only the BL data respectively. Other choices are easy to implement). The argument for <math>\alpha</math> is passed to the BL datafile and included in the name of the dumped file.</li> </ul>
SETBL	S	setbl.f	<p>Build the Jacobian and RHS of the Newton system for the BL grid nodes.</p> <ul style="list-style-type: none"> <li>• Before sweeping over all BL surfaces and grid nodes, VWSET is called to re-set the suction distribution to account for the movement of the stagnation point and BL grid nodes.</li> </ul>
SETBC	S	setbc.f	<p>Overwrite the Jacobian and RHS entries for grid nodes located at the boundary with appropriate value for either far field or wall conditions.</p> <ul style="list-style-type: none"> <li>• Add the displacement due to the mass defect due to suction to the RHS of the equations prescribing the coupling condition (see also 3.5).</li> </ul>
INPUT, OUTPUT	S	io.f	<p>Subroutines for reading (INPUT) and writing (OUTPUT) the solution state from and to the file mdat.xxx.</p> <ul style="list-style-type: none"> <li>• Added reading and writing of suction distribution <math>v_w</math>, suction mass defect displacement <math>\delta_{\text{suction}}^*</math> and <math>\rho_e</math>.</li> </ul>
UPDATE	S	update.f	<p>Update the solution vector (no surprise there).</p> <ul style="list-style-type: none"> <li>• Inviscid running mode ended in a segmentation fault (during runtime) because of a variable set only during a normal viscous running mode. Fixed.</li> </ul>

Table B.1: (continued)

MARCHBL	S	io.f	<p>Marches every BL surface (also the wake) for every station <math>i</math> to:</p> <ul style="list-style-type: none"> <li>• Establish the transition point based on the current solution;</li> <li>• Call BLVAR and BLSYS for every BL station to calculate the correct BL variables (laminar or turbulent<sup>1</sup>).</li> </ul> <p>It can be used in a ‘direct’ mode which prescribes <math>u_e</math> and <math>\delta^*</math> must follow. This can lead to the infamous ‘Goldstein singularity’ hence it can also be used in a ‘mixed mode’ which takes both <math>u_e</math> and <math>\delta^*</math> as input and use a weighted linear combination of to assess the correct intersection point with the <math>u_e - \delta^*</math> relationship.</p> <ul style="list-style-type: none"> <li>• Calculate the displacement due to thickness <math>\delta^*_{\text{suction}}</math> by calculating the integral in equation 3.12.</li> <li>• Added suction information to the argument list for every call to BLVAR and BLSYS.</li> </ul>
BLVAR	S	blvar.f	<p>Calculate non-kinematic BL variables for a certain BL grid node.</p> <ul style="list-style-type: none"> <li>• Added suction information to the argument list.</li> <li>• Calculate <math>C_\mu</math> and derivatives wrt. primary BL variables.</li> <li>• <math>H_k</math> lower limit is lowered further since with suction it should be able to approach 1 very closely.</li> <li>• Calculation of slip velocity <math>U_{\text{slip}}</math> reordered before calculation of <math>C_f</math> since the closure relation of <math>C_f</math> modified for suction requires <math>\bar{U}_{\text{slip}}</math>.</li> <li>• Modified closure relation of <math>C_f</math> for suction cases, see also section 3.4. Also the derivatives of <math>C_f</math> are modified in accordance with the modified closure relation.</li> <li>• Modified closure relation for <math>C_\mathcal{D}</math> as well as the derivatives with respect to the primary BL variables.</li> </ul>
BLSYS	S	blsys.f	<p>Sets up the integral momentum BL formulation equations and the shear lag equation (i.e. stores Jacobian entries and RHS in temporary local Newton system for later easy access). Also splits interval where transition occurs into a laminar and turbulent part (no additional grid nodes are created though).</p> <ul style="list-style-type: none"> <li>• Added suction information to argument list.</li> <li>• Added interpolated value for <math>\nu_w</math> at the transition point (in case of a transition interval).</li> <li>• Added suction information to argument list for all BLVAR calls.</li> </ul>

<sup>1</sup>Or similarity

Table B.1: (continued)

BLDIF	S	bldif.f	Calculates the Jacobian entries and RHS for the ODE's governing the BL for one interval (the integral momentum BL formulation and the shear lag equation). <ul style="list-style-type: none"> <li>Inclusion of <math>C_\mu</math> in the governing equations. At this level MSES already — very conveniently — included some sort of provision for future inclusion of <math>C_\mu</math>, which was used gracefully.</li> </ul>
CFTFUN	S	blfun.f	Calculate turbulent $C_f$ for a certain BL grid node.
ELLIP	S	ellip.f	Elliptic grid smoother. <ul style="list-style-type: none"> <li>Value of 'IDIM' raised to allow larger grids.</li> </ul>
New routines			
Routine	P/S	Located in	Description
JVWINI	S	sucsub.f	Initialize suction distribution and related variables to zero for all BL surfaces.
VWREAD	S	sucsub.f	Read suction distribution $\nu_w$ for BL surfaces from file suction.xxx.
VWSET	S	sucsub.f	Set suction distribution $\nu_w$ in arrays for every surface and BL grid node for easy access during calculating the BL variables and $\delta_{\text{suction}}^*$ . This routine has to be recalled after every solution update since due to the movement of the stagnation point also the BL grid nodes may move.
Other			
Routine		Located in	Description & Changes
STATE.INC		STATE.INC	File with (common) definition of solution state variables. It can be called from any routine to be included which allows the share variables between the main program and different subroutines. <ul style="list-style-type: none"> <li>Variables for suction added, including the prescribed <math>\nu_w</math> distribution and also other related variables such as <math>\delta_{\text{suction}}^*</math>.</li> <li>Value of 'IX' and 'JX' raised to allow larger grids.</li> </ul>



# C

## MSES & CONVERGENCE

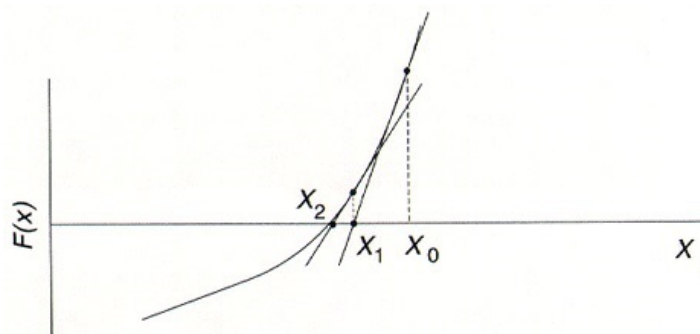
As much as one would like their simulations to run smoothly and recreate the real physics of a problem (and of course, this includes the author), a simulation is just this: an approximation to this reality. Reality is approximated by means of mathematical relations, be it governing equations founded upon a mathematical description of reality (e.g. the N-S equations and the derived momentum integral relations) or empirical relations based on experimental data (e.g. the closure relations). Regardless of the nature of these relations, solving them may cause several problems. This chapter is dedicated to shed some light on these problems, yet<sup>1</sup> a solution or even a fix to these problems is not always provided.

### C.1. CONVERGENCE OF THE NEWTON SOLVER

In MSES, the equations to be solved are a set of non-linear differential equations: the Euler equations for the inviscid grid and the momentum integral relations for the viscous BL; these have to be solved for every grid node or BL surface node respectively. This non-linear system is solved by Newton's method. How the system of equation is set up is briefly explained in section 3.1.1. The system is then solved by converging towards the solution using Newton's method. When convergence fails, the cause of this remains unclear because no output data is generated. To remedy this, a piece of code was added to MSES that, during runtime, provides output of the solutions for the boundary layer and grid (which in the case of MSES is actually the solution) for every iteration. Obviously, providing output for every iteration leads to an explosion of data, and the default compilation of the program does not provide this. Also the history of the 'convergence parameters' (see also further) is given as output, which helps to find a cause for convergence failure.

To understand the causes of convergence failure in MSES it is essential to get an idea of why a Newton system can fail to converge to the solution. In turn, a basic understanding of Newton's method is required. To this end, it is useful to draw an analogy with the way a Newton system is solved for only one degree of freedom. Of course, in MSES the system has typically several thousand degrees of freedom. In short, Newton's method to find a root of  $y = f(x)$  consists of:

1. At a certain position  $x_i$ , calculate  $f(x_i)$  and  $f'(x_i)$  and find the root of the tangent at  $x_i$ .
2. Make this root the new  $x_i$  and go back to 1.
3. Root is found if  $x_i$  does not move between successive iterations.



In practice, finding the exact root is rare and instead the change of the solution between successive iterations is tracked. When this drops below a certain threshold or 'tolerance' this is accepted as the root. In the

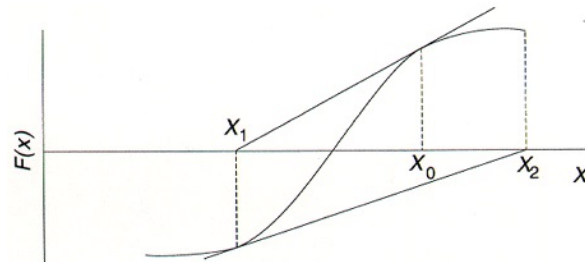
<sup>1</sup>Spoiler alert!

case of MSES, the change of the solution is tracked by six ‘convergence parameters’. They are a measure of how much the solution has changed since the previous iteration. As convergence parameters, MSES uses:

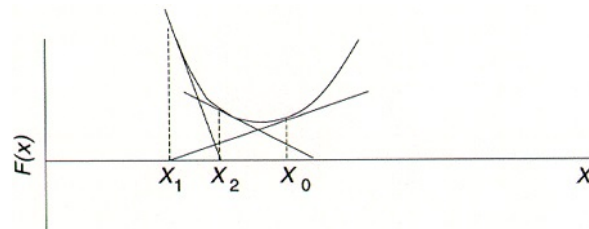
- The RMS of the change of the ‘area’ (or better, the ‘thickness’ of the streamtubes) and the density at all inviscid nodes and the RMS of a measure for the inviscid parameters at the viscous surface nodes: DNRMS, DRRMS and DVRMS respectively.
- The maximum changes of the same quantities: DNMAX, DRMAX and DVMAX.

The approach described above can fail to converge due to an inflection point near the root, the fact that there is simply no root or very slow convergence due to an almost zero or infinite slope:

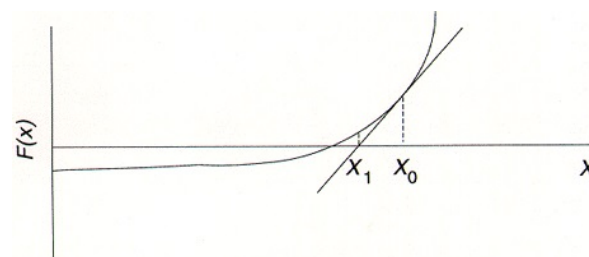
**Inflection point:** the Newton solver can get stuck in a ‘loop’, alternating between solutions on either side of the solution. This generally leads to oscillating behaviour of the solution, possibly diverging.



**No root:** when there is simply no root, the Newton solver also cannot find one. Generally this leads to the solution diverging quickly.



**Slope:** the tangent may be calculated where the slope is either very large or low. In the former case convergence will be extremely slow (and the solver may leave due to a maximum amount of iterations). In the latter case the solver may even be thrown completely off-track, i.e. arrive at a point very far from the actual solution.



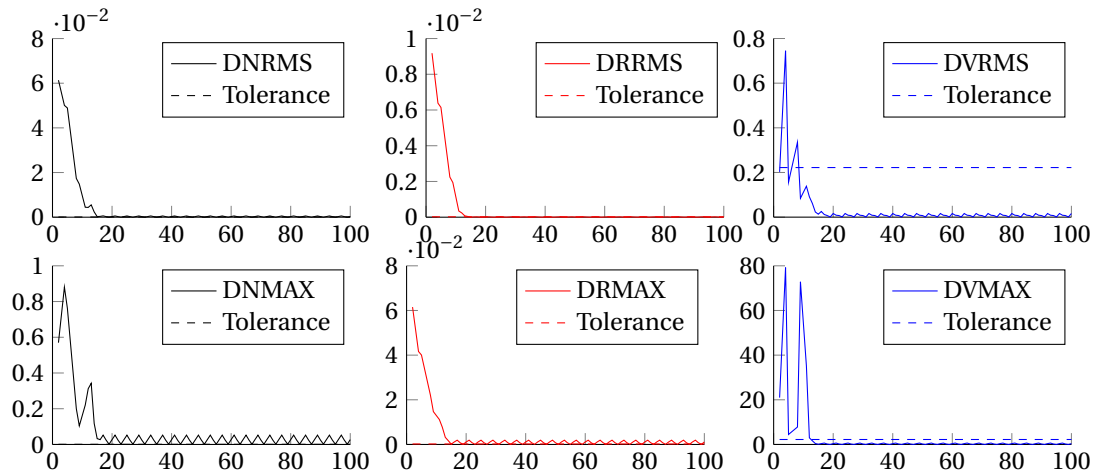
For the sake of completeness it is also worthwhile to mention that the system can converge to the wrong root if there happen to be multiple ones. It is then up to the user to identify the solution as (probably) being unphysical.

The next sections will relate these problems to some cases encountered during the project with MSES.

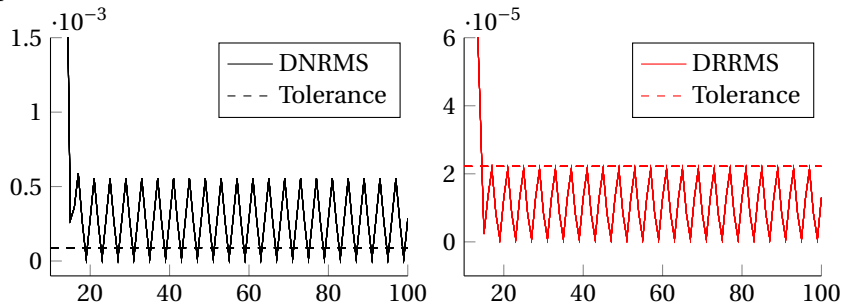
## C.2. A FLAP DEFLECTION OF $26^\circ$ ON THE NLR7301 AIRFOIL

Inspecting figure ?? shows that, for the case without suction, the NLR7301 airfoil does not have a solution for a flap deflection of  $26^\circ$ . This may at first glance seem somewhat strange since a solution is again present for larger flap deflections. However, the history of the convergence shown in figure C.1a shows that the convergence parameters are oscillating and because of this do not drop below the convergence tolerances, although they are very close to it. It is reasonable to assume that oscillating convergence parameters are caused by the solution that is also oscillating at some points. This can also be checked by inspecting the output of the solution for every iteration, which confirms the assumption. Figure C.6 is shown for this purpose, which shows the solution for  $\delta^*$  of the last iterations before convergence ‘fails’. Note that in this case it is merely shown for completeness, changes in the solution are not even visible(!). Closer inspection learns that the source of the oscillation can more than likely be found near the trailing edge of the main element where there is a separation bubble; MSES handles the separation bubble not very well here. Nevertheless, continuing the overall

discussion, the fact that the solution is oscillating hints at an ‘inflection point problem’ as described in section C.1. This means that the solver is close to the solution but cannot reach it because it is stuck in a loop (also Terry already described this problem with MSES [39]). Inspection of the solution shows that it is indeed already well within the bounds that can be expected for this configuration.



(a) Convergence parameters.



(b) Detail of DNRMS and DRRMS.

Figure C.1: Convergence history of the NLR7301 case with  $\delta_f = 26^\circ$ . Iteration number on the  $x$ -axis.

A fix for this problem was added to the code of MSES and MPOLAR. It is a rather simple one: it looks at the history of the convergence parameters and if they oscillate reasonably close to the actual tolerance, the solution is accepted. A provision was made to switch it on or off during runtime since this rather rudimentary fix may in some cases just boil down to relaxed convergence criteria which is not desired. Preferably, the option is only used if an oscillating solution is encountered.

### C.3. THE NLR7301 AIRFOIL AT $\alpha = 15^\circ$

A more fundamental problem is encountered for the same NLR7301 airfoil at an angle of attack of  $15^\circ$  and with the flap in the ‘default’ position (as it happens, also at  $\approx 15^\circ$ ). As can be seen from figure 6.2 there is no solution for this angle of attack. Why? The answer is obvious of course, the flow has separated and MSES cannot deal with this. This is also evident from the convergence history shown in figure C.2: the error quickly escalated and there is no solution any more after 19 iterations. This is a clear example of a situation where there is ‘no solution’ as explained in section C.1. The equations that MSES use for the viscous domain rely on the assumption of a relatively thin boundary layer and for a flow with massive separation they are simply not valid and are unable to provide a solution.

Figure C.7 shows the iteration history of  $\delta^*$  for this case. Due to the inviscid-viscid interaction also the inviscid domain is affected and the grid (which is the solution for the inviscid domain) is completely messed up as is evidenced by the changing scales on the  $x$ -axis. Also note that it is the wake that is the first to diverge: wake burst is the cause of separation here; an interesting observation especially in the context of the project.

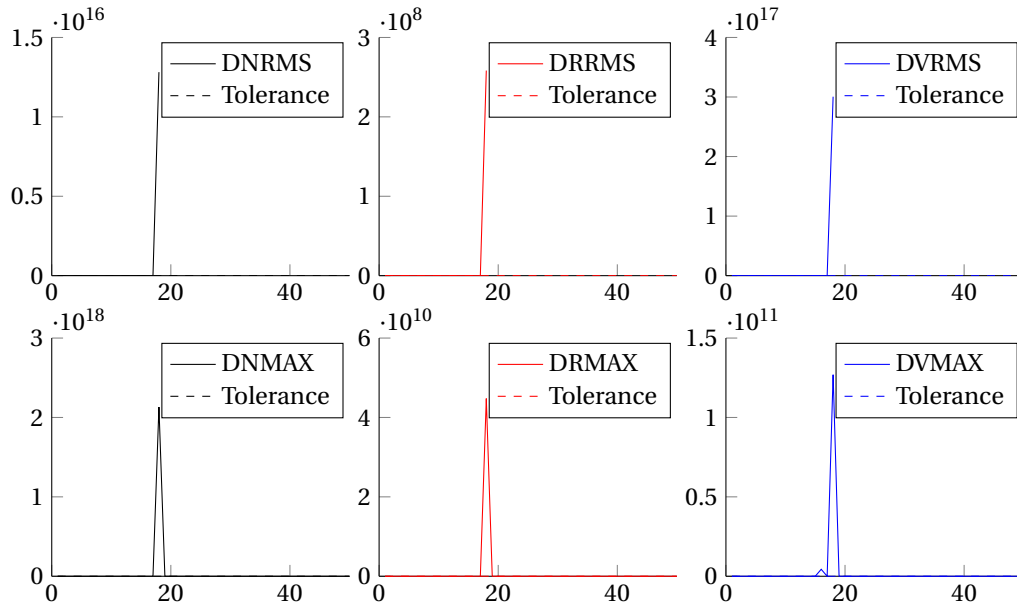


Figure C.2: Convergence history for the NLR7301 airfoil with  $\delta_f = 15^\circ$  at  $\alpha = 15^\circ$ . Iteration number on the x-axis.

#### C.4. THE NLF22 AIRFOIL

When simulating the NLF22 airfoil at zero angle of attack (no suction), which is by all means a reasonable flow configuration where no significant flow separation is expected. The NLF22 airfoil however features a flap cove that, despite that there are no corners in the geometry, is very ‘deep’ and separation may very well be expected. MSES showed to be quite robust and in most cases is able to correctly detect a very large displacement thickness here (see e.g. the separation ‘bubble’ at the flap cove as evidenced by  $\delta^*$  over the lower surface in figure C.8). To rule this out as a possible reason for a diverging solution, the lower surface of the main element was reconstructed with a more ‘relaxed’ flap cove based on the NLR7301 geometry. Figure C.3 and C.4 show the original and modified geometries respectively.

Another problem however was encountered: after a few iterations the solution diverges for no obvious reason (figure C.5). The problem seems to be located at the trailing edge of the flap. It is not clear if this is a bug in the code or if the relations in MSES simply cannot handle this flow configuration. Inspection of the solution hints that the problem originates in the viscous calculations: around iteration 15 the viscous solution of the wake at the flap TE starts to diverge (figure C.8) and only later the inviscid solution follows (figure C.9 showing grids = inviscid solution).

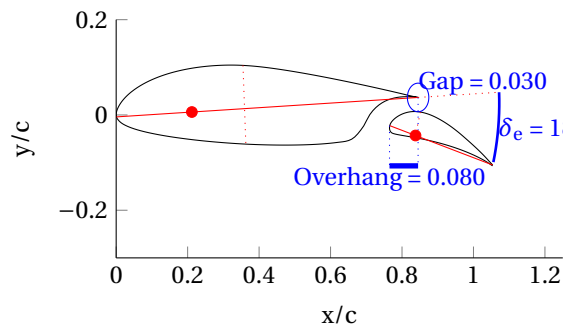


Figure C.3: NLF22 airfoil.

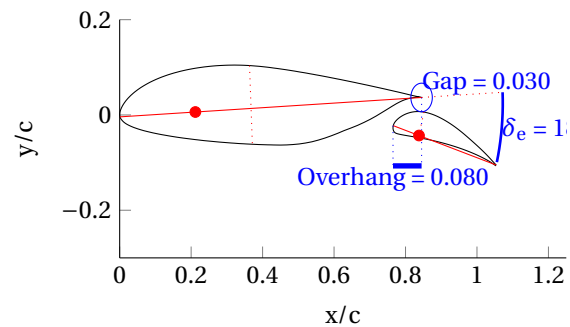


Figure C.4: Modified NLF22 airfoil.

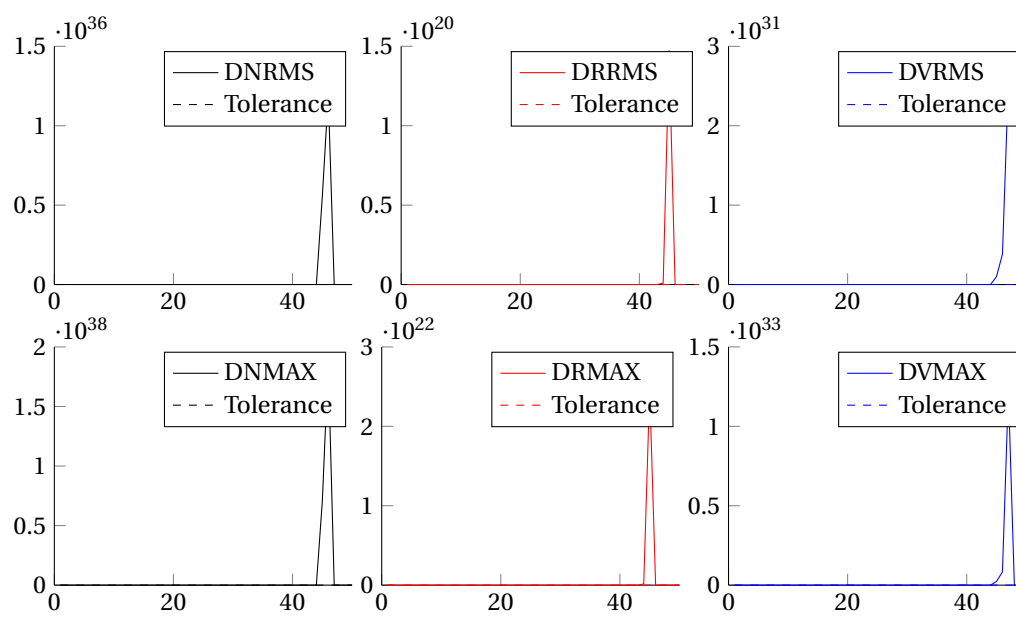
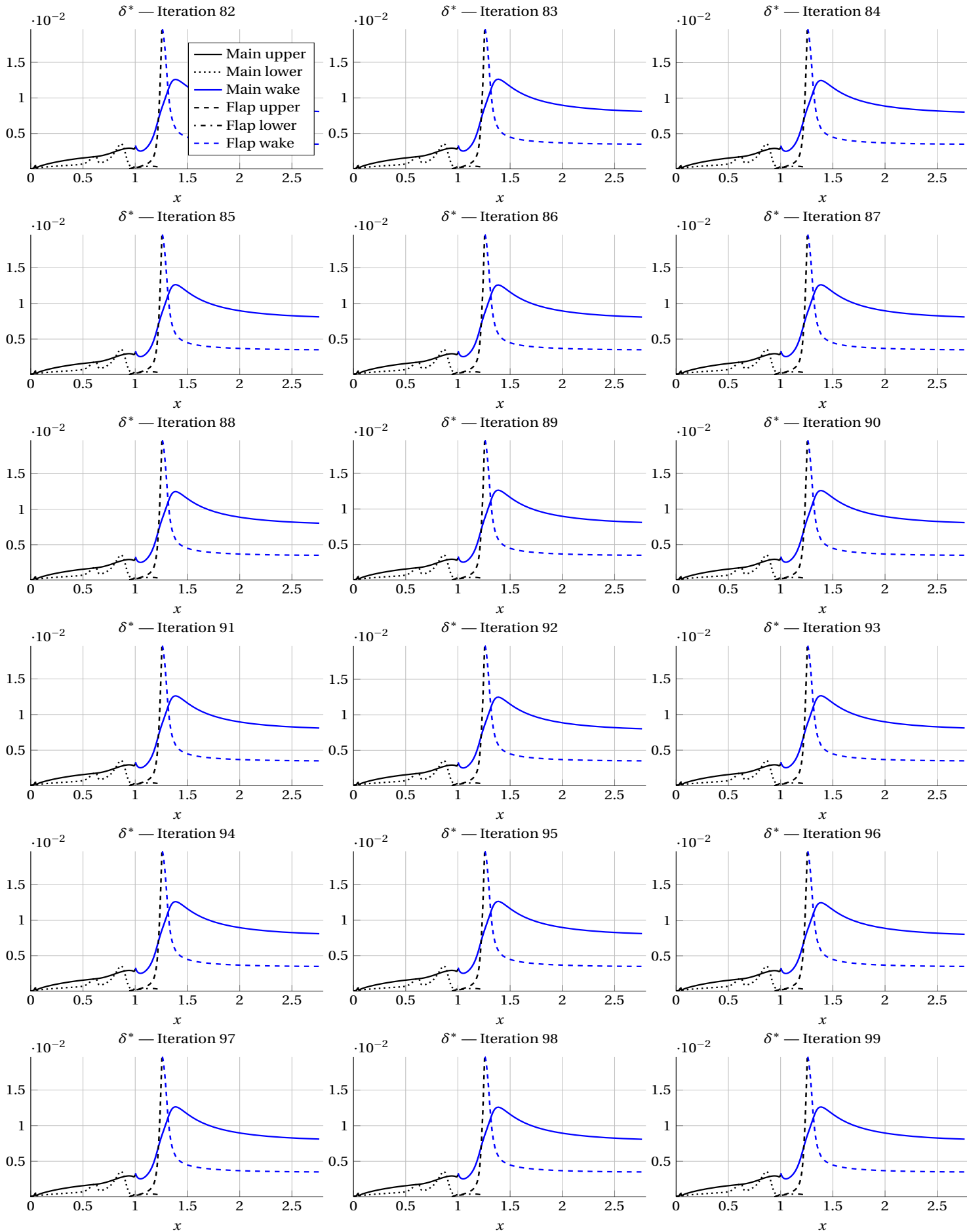


Figure C.5: Convergence history for the NLF22 airfoil. Iteration number on the  $x$ -axis.

Figure C.6: Iteration history of  $\delta^*$  for the NLR7301 airfoil with  $\delta_f = 26^\circ$ .

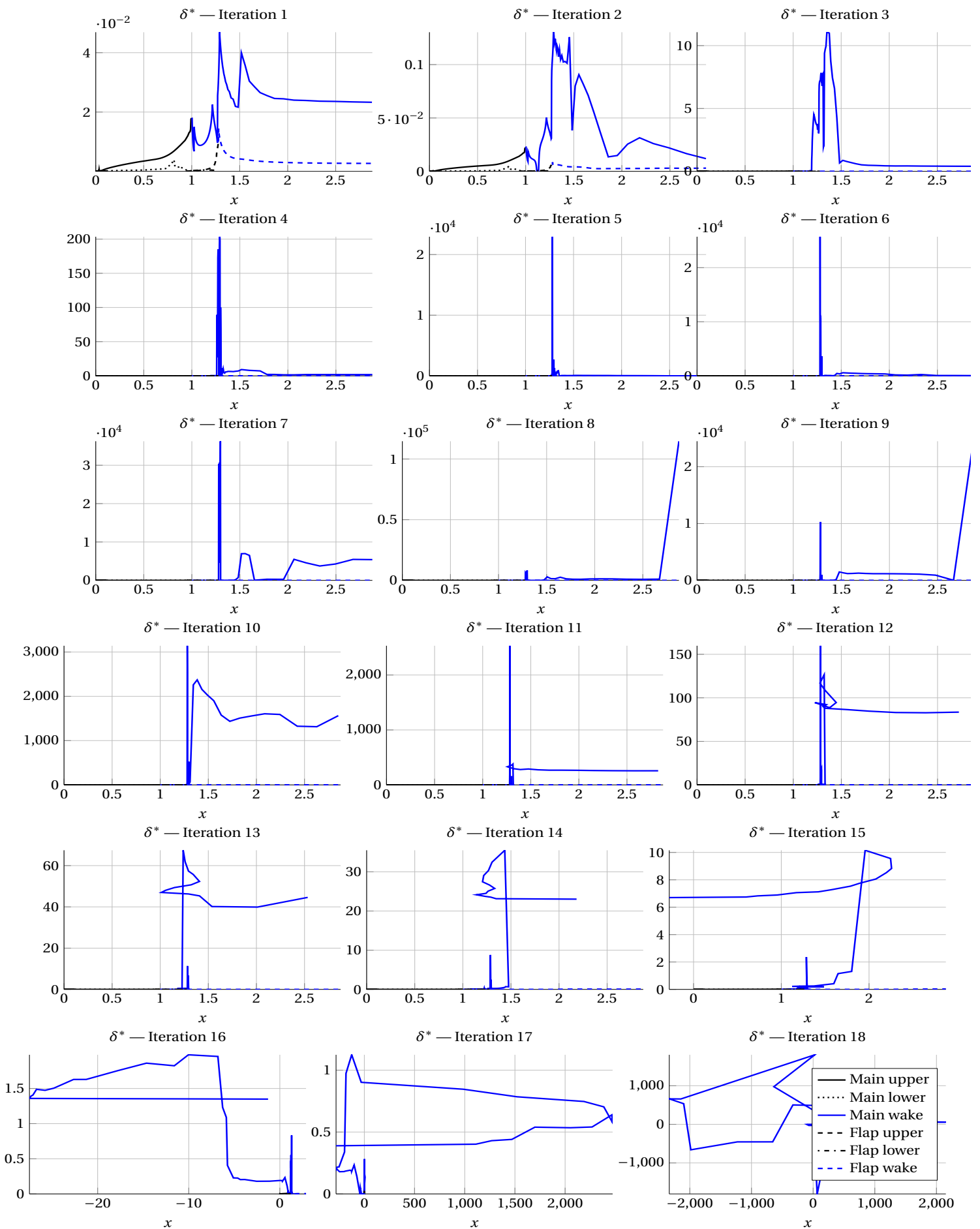
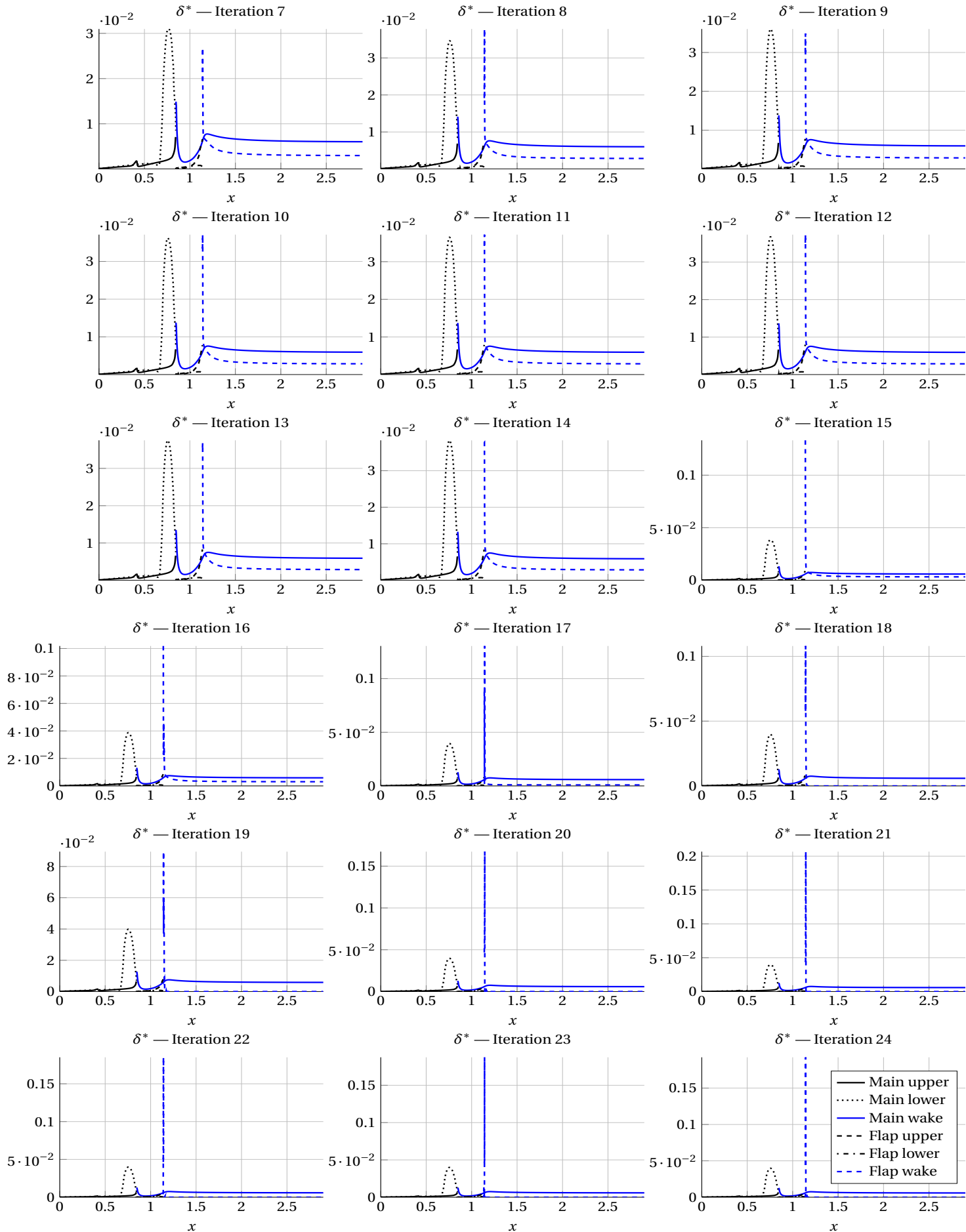


Figure C.7: Iteration history of  $\delta^*$  for the NLR7301 airfoil with  $\delta_f = 15^\circ$  at  $\alpha = 15^\circ$ .

Figure C.8: Iteration history of  $\delta^*$  for the NLF22 airfoil.

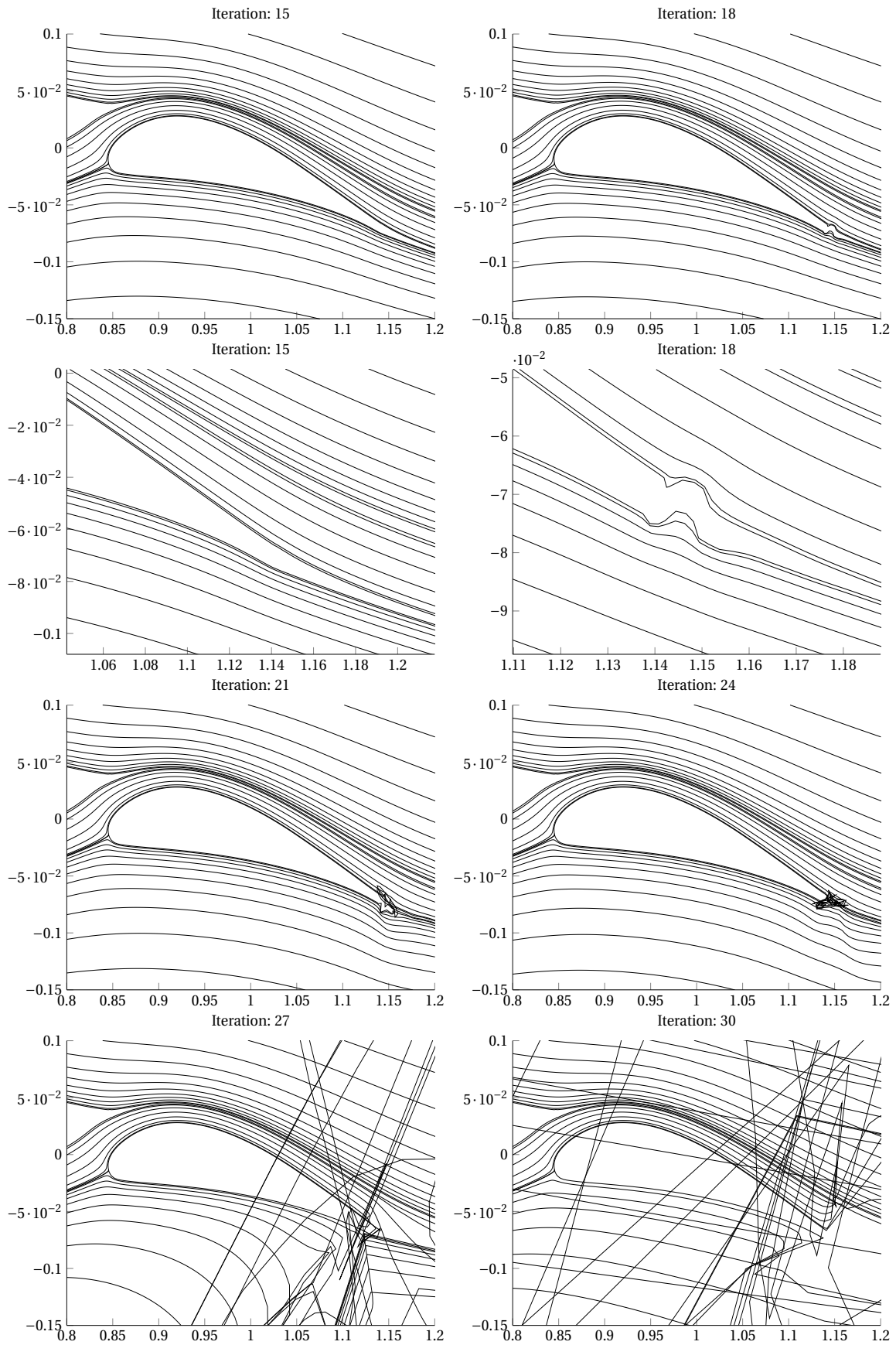


Figure C.9: Iteration history of the inviscid grid at the flap of the NLF22 airfoil.